Abdulwahid, Ahmed Adeeb (2020) ***Heat and mass transfer mechanisms in a wet scrubber.*** **PhD Thesis, James Cook University.**

Access to this file is available from:

https://doi.org/10.25903/vqrr%2D5f27

Heat and mass transfer mechanisms in a wet scrubber

Thesis submitted by

MSc. Ahmed Adeeb Abdulwahid

April 2020

For the degree of Doctor of Philosophy in the department of engineering and science

James Cook University, Australia

Statement of Access

I, the undersigned, author of this work, understand that James Cook University will make this thesis available for use within the University Library and, via the Australian Digital Theses network, for use elsewhere.

All users consulting this thesis will have to sign the following statement: "In consulting this thesis I agree not to copy or closely paraphrase it in whole or in part without the written consent of the author and to make proper public written acknowledgment for any assistance that I have obtained from it."

I understand that, as an unpublished work, a thesis has significant protection under the Copyright Act (1968).

Every reasonable effort has been made to gain permission and acknowledge the owners of copyright material. I would be pleased to hear from any copyright owner who has been omitted or incorrectly acknowledged.

Ahmed Abdulwahid

Acknowledgments

I would like to thank my creator ALLAH for everything in my life not just getting this degree and I am sure the word "thank" is not enough.

I thank my father (Adeeb) who helped me a lot during his life and after his shocking death. Big thanks for my lovely boys (Ibrahim and Abdullah) who have been more than patient during my hard journey. They bring brightness and pleasantness to my life. Indeed, I wrote these two sentences with tears. I am very proud of them. Many thanks to my wife (Faten) for her encouragement to get this degree.

I thank my principal supervisor (Dr Rong Situ) for his support and for his advice as a friend. Another big thank-you to Professor Richard Brown from QUT. Many thanks to everyone from JCU who have helped and/or supported me: Melissa Norton, Helen Marsh, Associate Professor Liz Tynan, Jodi Wilson, Professor Wenxian Lin, Troy Poole, Dean Frendon and Shane. Also, I would like to thank PhD students Liqiang Dong, Ali and other lab. mates from the undergraduate students.

Thanks also to my best friends and work mates: Dr. M. Sabri, Abdulwahab, Shaimaa, Zaid, Shay Maa, Areej, Mohammed, Suhad, Younis, Esraa and others. A very special thanks to Vian who I cannot describe how much I appreciate her help. Another special thanks to the people who helped me to come and study in Australia: Luay, Najla and Ammar. Also I thank the Ministry of Higher Education and Scientific Research in Iraq for the financial support during my first three years of study.

Abstract

A wet scrubber is an air pollution removal device that eliminates Particulate Matter (PM) and acid gases. This scrubber is connected with a diesel engine of underground vehicles in the stream of the exhaust gases between the engine and the Dry Particulate Filter (DPF). The exhaust gas enters the scrubber beneath the surface of the scrubbing liquid, causing a reduction in both gas temperature and concentrations of some soluble particles. This process increases the Relative Humidity (RH) of the gas at the scrubber outlet. This high relative humidity blocks the downstream dry particulate filter and increases the overall production cost. Reducing this cost and improving the environment can be achieved through optimising the wet scrubber. The objective of this study are: investigating the wet scrubber in different methods, then suggest a new design that reduces the relative humidity and temperature at the scrubber exit.

The combination of three methods are used in this thesis to investigate scrubber performance: experiments, thermodynamic analysis and heat transfer analysis. The experiments include transient heat loss estimation tests, the heating tests and the flow visualisation tests. The transient heat loss estimation tests estimate the heat loss from the scrubber at steady-state process. These heat-loss tests are discussed and compared such as conduction, convection and radiation. Then, the most accurate one is selected to estimate the heat loss from the scrubber. The heating experiments include 115 steady-state heating tests to analyse the scrubber thermodynamically. Furthermore, 16 bubble heat transfer experiments are conducted with a high-speed video system. The data of these experiments are used for the thermodynamic and heat transfer analysis of the scrubber. The thermodynamic analysis estimates the outlet gas relative humidity and compares it with the measured ones. The heat transfer analysis investigates the direct interaction between the gas bubbles and their surrounding scrubbing liquid. The bubble heat transfer analysis proposes several correlations for the flow and the heat transfer, including the free convection heat transfer coefficient between bubbles and liquid.

Several parameters have a major influence on scrubber performance, such as the flow rate and the temperature of the inlet gas as well as the scrubbing liquid volume ratio. The designing parameters have a minor effect on the scrubber performance such as the orifice size. To explain, the current scrubber reduces the gas temperature up to 590ºC, and increases the relative humidity up to the saturation condition. Adding the orifice plate reduced the flow turbulence and the liquid leaving the scrubber from the scrubber outlet. Further, increasing the

liquid volume ratio reduced the outlet gas temperature. Increasing the inlet gas Reynolds number and/or temperature ratio increases the relative humidity.

Three flow regions are recognised at low Reynolds numbers of the inlet gas: departing, churn-turbulent and bubbly. Only the churn-turbulent region was observed at high inlet gas flow rate. Bubbles departed the orifice row at the departing region with different shapes, sizes and velocities. The bubble diameter was a function of the inlet gas volumetric flow rate or the Reynolds number. The inlet gas Reynolds number, inlet gas temperature ratio and the orifice ratio affected the bubble vertical velocity or bubble Reynolds number.

The outcome of our work adds to the existing knowledge of after-treatment of diesel exhaust. After a careful investigation and combining the three methods mentioned earlier, a new design of the scrubber is suggested, based on optimising scrubber performance. The new design prolongs dry particulate filter life by reducing the outlet gas relative humidity. Also, the new scrubber design should improve the workplace environment and the workers' social lives. Therefore, this should maximise the economic benefits in countries such as Australia where mining equipment plays an important role in the economy.

List of Publications

1. Abdulwahid, A. A., Situ, R., Brown, R. J. Underground diesel exhaust wet scrubbers: Current status and future prospects. *Energies* **2018**, 11, 1-20. doi:10.3390/en11113006.
2. Abdulwahid, A. A., Situ, R., Brown, R. J., Heat and mass transfer process in exhaust wet scrubber, 21st Australasian Fluid Mech. Conf. 10th-13th Dec. **2018**, Australia, doi: https://www.conftool.com/21afmc/index.php?page=browseSessions&form_session=59.
3. Abdulwahid, A. A., Situ, R., Brown, R. J., Lin, W., Thermodynamic Analysis of a Diesel Exhaust Wet Scrubber, 22nd Australasian Fluid Mech. Conf. 6th-10th Dec. **2020**, Australia, submitted.
4. Abdulwahid, A. A., Situ, R., Brown, R. J., Lin, W., Bubble Dynamics in a Diesel Exhaust Wet Scrubber, 22nd Australasian Fluid Mech. Conf. 6th-10th Dec. **2020**, Australia, submitted.

Table of Contents

Lists of Figures

Chapter 5

List of Tables

List of Symbols

Nomenclature:

A	Area or Surface area (m^2).
AR	Aspect ratio.
a	Bubble acceleration (m/s^2).
Bo	Bond number.
C	Component concentration.
C_D	Drag coefficient.
c_p	Specific heat (kJ/kg.K).
D	Inlet pipe diameter (m).
D_c	Column diameter (m).
d_o	Orifice diameter (m).
DPF	Dry Particulate Filter.
d	Bubble diameter (m).
$\frac{dW}{dt}$	Water mass change within scrubber (kg/s).
E	Evaporation rate (m^3/s).
$\dot{E}$	Energy (kW).
EC	Elemental Carbon.
Ec	Eckert number.
e	Internal energy (kJ/kg).
F	Force (N).
g	Gravity acceleration (m/s^2).
H	Column length (m).
h	Fluid enthalpy (kJ/kg).
h	Heat transfer coefficient ($W/m^2.K$).
h_c	Condensation heat transfer coefficient ($W/m^2.K$).
k	Fluid thermal conductivity (W/m.K).
k_v	Velocity factor.
L	The characteristic length (m).
L/G	Liquid to gas ratio (%).
LLSP	Laser Light Scattering Photometry.
LVR	Liquid volume ratio (%).
$\dot{m}$	Mass flow rate (kg/sec.)
Nu	Nusselt number.
n	Bubble frequency.
nb	The number of bubbles.
nc	Natural convection.

Greek letters:

α	Fluid thermal diffusivity (m^2/s).
β	Dimensionless radius (R/R_o).
β	Orifice ratio.
β_b	Bubble diameter ratio.
β'	Dimensionless constant.
β''	Contact angle (^{0}).
θ	Inlet gas temperature ratio.
γ	Thermal expansion coefficient (1/K).
Δ	Changes.
ϵ	Emissivity.
ε	Dissipation rate (m^2/s^3).
ε'	Hold-up.
η	Removal efficiency (%).
λ	Latent heat of evaporation (kJ/kg).
μ	The fluid dynamic viscosity (mPa.s).
μ'	The fluid drop internal viscosity (mPa.s).
v	Fluid kinematic viscosity (m^2/s).
ρ	The density of the fluid (kg/m^3).
σ	Stefan-Boltzman constant.
σ	Surface tension (N/m).
τ	Dimensionless time.
$\emptyset$	Volume fraction in slurry phase.
$\emptyset'$	Surface orientation (^{0}).

Subscript:

a	Ambient.
$above$	Above water surface.
B	Buoyance.
b	Bubble.
$below$	Below water surface.
cond.	Conduction.
conv.	Convection.
CO_2	Carbon dioxide.
D	Drag.
e	Equivalent.
ev	Evaporative.

PM	Particulate Matter.	f	Liquid.
Pr	Prandtl number.	G	Gravity.
Q	Heat transfer (kW).	g	Gas.
$Q^{'}$	Average volumetric flow rate (m^3/s).	H_2O	Water / water vapor.
q	Heat flux (W/m^2).	i	Sequence.
$q^{'}$	Heat transfer rate (kW).	in	Inlet.
R	Bubble radius (m).	k	Condensation.
$R^{'}$	Curvature radius of lenticular body (m).	L	Loss.
R''	Bubble radial velocity (dR/dt).	l	Liquid.
Ra	Rayleigh number.	m	Mixture.
Re	Reynolds number.	max	Maximum value.
RH	Relative humidity.	n	Net.
S	Storage volume (m^3).	O_2	Oxygen.
sa	Bubble front face area (m^2).	out	Outlet.
SMPS	Scanning Mobility Particle Sizer.	p	Polycarbonate.
St	Stanton number.	s	Steel.
SVR	Support Vector Regression.	sc	Scrubber.
T	Temperature (K).	sm	Small bubble.
TEOM	Tapered Element Oscillating Microbalance.	T	Terminal.
th	Thickness (m).	$trans$	Transition region.
t	Time (sec.)	V	Virtual
P	Pressure (kpa).	v	Vapor/gas.
U	Relative vapor-liquid velocity (m/s)	W	Bubble wall.
u	The fluid velocity (m/s).	w	Wet scrubber storage.
V	Volume (m^3).	Δv	Water volume changing due to evaporation.
W	Column width (m).	0	Initial value.
x	Bubble x-position (m).	∞	Bubble surrounding fluid.
z	Bubble z-position (m).		

Chapter 1 – Introduction

1.1. Background

Diesel engine emissions are divided into gaseous precursors such as NOx, H_2SO_4, SO_3, SO_2 and H_2O. These emissions also contain semi-volatile organic compounds and solid carbonaceous material such as Particulate Matter (PM) (Giechaskiel et al. 2018 (A, B)). To clarify, PM is a suspended mixture in air, consisting of solid and liquid particles (Giechaskiel et al. 2018, Miljevic 2010). The characterisation and chemical composition of the PM depend on several parameters related to the engine, the environment and the fuel. The engine factors include rpm, load, type, lubrication oil, and age (Gaffney and Marley 2009, Giakoumis et al. 2017, Pratt et al. 2018, Papagiannakis et al. 2016). The environmental parameters are temperature and relative humidity, etc. (Gaffney and Marley 2009). Also, fuel properties such as density, polyaromatic content and sulphur content affect PM generation (Papagiannakis et al. 2016, Suarez-Bertoa et al. 2019, Rakopoulos et al. 2015, Cardenas et al. 2016, Mata et al. 2017). However, special devices can be connected to exhaust systems to reduce these emissions, such as a Diesel Particulate Filter (DPF) and a wet scrubber. A wet scrubber is defined as an air-pollution removal device that is fitted into the stream of exhaust gases (Mussatti and Hemmer 2017). In particular, for both underground and marine equipment.

Scientists worldwide have investigated wet scrubbers or similar devices. For example, Davidson & Schüler (1997) experimentally investigated bubble formation at an orifice fitted inside a viscous liquid. Several forces caused by gas flow rate and liquid density limit both bubble motion and their positions, such as drag, buoyancy, surface tension and inertia. Also, Jhawar and Prakash (2007) confirmed that a high rate of heat transfer can be achieved in a heterogeneous flow. Indeed, increasing the inlet gas velocity increases the mixing of the liquid phase and reduces bubble size due to high bubble breakup. Nevertheless, at low inlet gas velocities, bubble breakup and coalescence were weak, in addition to a narrow distribution being observed.

Moreover, Guo and Gao used a wet scrubber to remove both SO_2 and NO_2, using limestone slurry (2008). They investigated the reaction temperature, the oxygen amount in the flue gas, and the inlet concentration of SO_2 and NO_2. Guo and Gao found that minimising the concentration of the inlet NO_2, the amount of O_2 in the flue gas, and the reacting temperature, caused a reduction in the removal efficiency of SO_2. Nevertheless, the absorption of NO_2 increased due to increasing concentrations of the inlet SO_2 and reducing the reaction temperature and the flue gas oxygen.

This scrubber analysed by Situ et al. (2012) thermodynamically based on the First Law of Thermodynamics and the continuity equation. They observed that the relative humidity of the outlet gas depends on the inlet gas temperature and flow rate. Also, the high gas flow rate ejects the scrubbing liquid from the scrubber via the outlet gas exit. The current study expanded the investigation parameters to include the designing and operating ones. Also, it combines 3 methods to investigate the scrubber: experiments, thermodynamic analysis and heat transfer analysis. This combination, the variety of the investigated parameters and the range of operating conditions did not covered previously by the scientists.

1.2. Research Questions

This thesis addresses four main questions. Is scrubber's performance affected by the operating conditions (inlet gas conditions) such as temperature and/or flow rate? Is scrubber's performance affected by design conditions such as scrubbing liquid volume and orifice size? What is the optimum operating condition of the scrubber? What is the gas condition at the exit of the wet scrubber? Can the relative humidity at the scrubber exit be reduced? Can the liquid ejected to outside the scrubber be reduced? Answering these questions will help elucidate the performance of the scrubber hydro-dynamically and thermally. This helps us to suggest a new design of the wet scrubber.

1.3. Research Approach, Model Development and Objectives

The current design of wet scrubbers consists of a tank (scale 1:1) with an inlet pipe in which the outlet is inserted beneath the scrubbing liquid surface (explained in detail in Chapter 2). Situ et al. (2012) investigated this design thermodynamically. This design effectively reduces exhaust gas temperatures. However, the current design has two disadvantages. Firstly, the high flow turbulence causes some scrubbing liquid to leave through the scrubber outlet. Secondly, the gas leaves the scrubber with relative humidity around or at the saturation condition. Because of these two issues, the dry filter after the scrubber can become blocked, thus increasing the production cost.

This thesis investigates the effect of operating conditions and design parameters on the scrubber performance. The operating conditions consist of wide range of inlet gas temperature and flow rate. This investigation achieved based on three methods: experiments, thermodynamic analysis and heat transfer analysis. These methods are explained in detail in Chapters 3, 4 and 5 respectively. The results of these methods are combined to suggest a new design based on optimum scrubber performance, as concluded in Chapter 6. The suggested design allows the gas to leave the scrubber with relative humidity below saturation, and also prevents the gas from carrying any scrubbing liquid with it on its way out. Also, this thesis helps better understanding the performance of this equipment will have an economic benefit because mining equipment plays an important role in the Australian economy. In other words, the objective of this study are: investigating the wet scrubber in different methods, using wide range of operating conditions, optimising scrubber performance then suggest a new design that reduces the relative humidity and temperature at the scrubber exit.

1.4. Thesis Structure (Overview)

This thesis starts with the introductory chapter, followed by a review, Chapter 1 (Figure 1-1). This figure shows main sections only. In Chapter 2, several studies are reviewed in detail in addition to an explanation of the parameters that may affect scrubber performance. Some scrubber analyses are also mentioned in the review chapter. Chapter 3 explains the experimental set-up and methodologies used to investigate the scrubber. Chapter 3 also includes an explanation of the exhaust wet scrubber, the experimental design and methodology, the primary experimental results and discussions and conclusion. Most experimental results are used to analyse the scrubber thermodynamically in Chapter 4. The heat transfer model of the scrubber is investigated in Chapter 5 using the corresponding experimental results.

Chapter 4 investigates the scrubber based on the first law of thermodynamics. The first section of this chapter describes the modelling design and methodology used in the following sections: the thermodynamic model results and discussion in addition to the outlet gas relative humidity calculation. The heat transfer analysis of the scrubber is explained in detail in Chapter 5. This chapter includes experimental design and methodology, flow characteristics observation, image analysis, result and discussion and the combined effect of orifice ratio, inlet gas Reynolds number and temperature ratio. The thesis ends with Chapter 6 with recommendations for future work. This final chapter consists of the conclusions (summary of findings) as well as the recommendations for future work (new design).

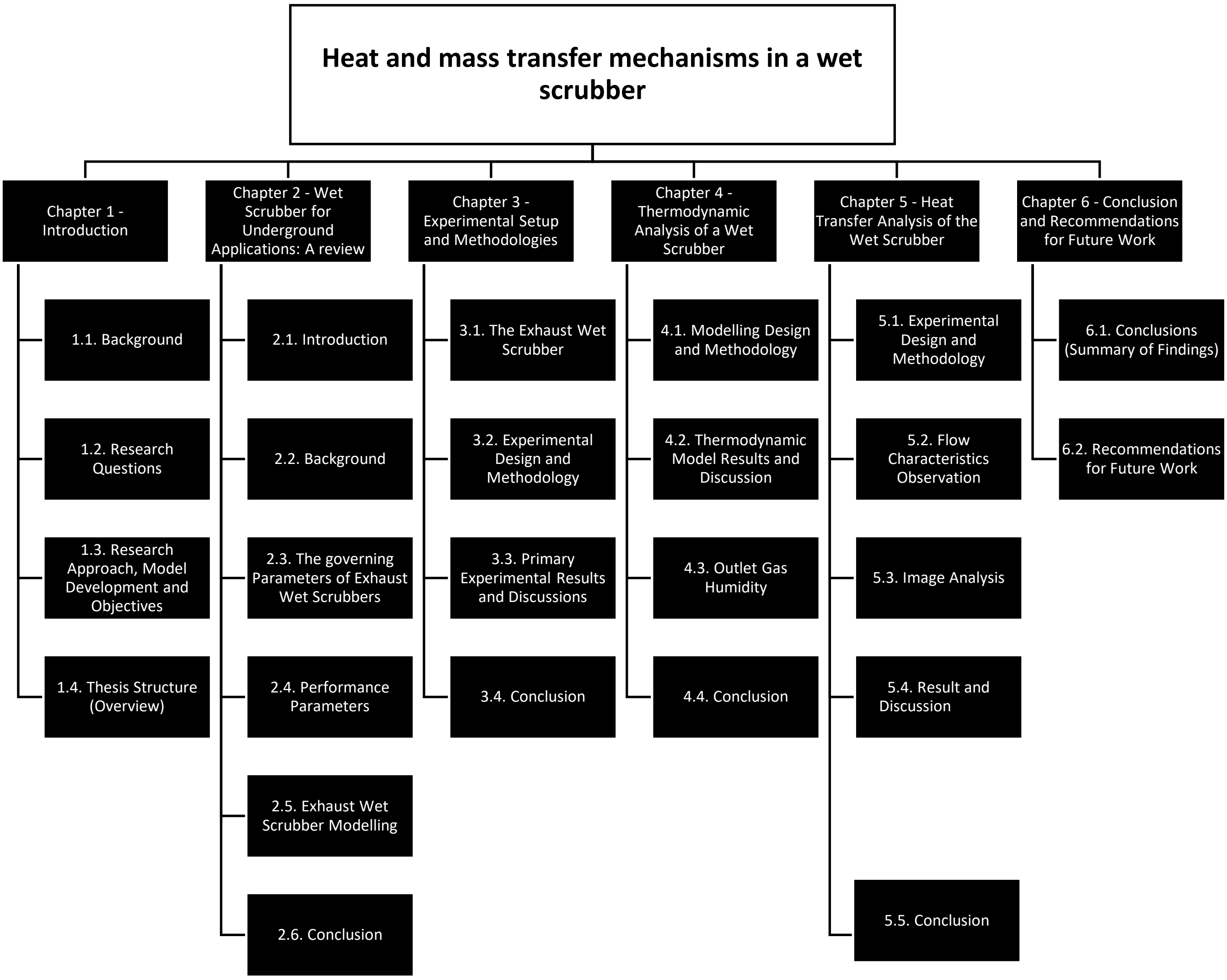

Figure (1-1) Thesis outline.

Chapter 2 - Wet Scrubber for Underground Applications: A Review

2.1. Introduction

Atmospheric air contains pollutants such as nitrogen dioxide (NOx), ground-level ozone (O_3), and particulate matter. These pollutants have a short-term and long-term effect on human health (Ristovski et al. 2012) in addition to their effect on climate change. In 2015, nearly 39% of nitrogen dioxides produced in the European Union were from the transportation sector alone. Significant nitrogen monoxide emissions and 50% of particulate matter are generated by diesel engines (Giechaskiel et al. 2018).

Particulate matter (PM) is a suspended mixture in air, consisting of solid and liquid particles (Giechaskiel et al. 2018, Miljevic 2010). PM particles have different morphologies, sizes and compositions. PM diameter can be measured using different methods based on their suitability. These methods are gravimetric, smoke opacity/smoke number, Laser Light Scattering Photometry (LLSP), Tapered Element Oscillating Microbalance (TEOM), and Scanning Mobility Particle Sizer (SMPS) (Rao et al. 2015). There is another measurement method developed by Volkwein et al. (2008) to estimate PM from engines, based on increasing the pressure across the dry filter.

Several techniques can be used to control engine emissions, especially for underground applications. These methods are low-emission fuel and engines (Rakopoulos et al. 2017), good ventilation, regular engine maintenance, effective filtration systems (for engine exhaust and operator cabin), and workforce education (Groothoff et al. 2013). Also, some special devices (connected with exhaust systems) can reduce these emissions, such as Diesel Particulate Filter (DPF), Engine Gas Recirculation (EGR), and Selective Catalytic Reduction (SCR) systems, etc. One of these devices is a wet scrubber. Wet scrubbers are defined as air pollution removal devices fitted in a stream of exhaust gases, to eliminate PM and acid gases (Mussatti and Hemmer 2002). Such a scrubber has a high resistance to temperature and humidity. Also, the scrubber has a small size (compared with the engine) and can thus be fitted easily to the engine (Situ et al. 2012).

This chapter aims to introduce and summarise the current status of wet scrubbers and similar devices such as the bubble column. It discusses all parameters which have a major effect on scrubber performance as well as ways to reduce both overall production costs and environmental pollution. Furthermore, this chapter reviews scrubbers to show past studies and suggest new methodologies to investigate scrubber performance. The next chapters follow these methodologies except the computational one.

This chapter starts by reviewing the importance of reducing the pollution of underground diesel engines (Figure 2-1). The background section discusses the pollutant-capturing mechanisms in scrubbers, the heat transfer mechanism, and the flow mechanism in a bubble column (due to scrubber similarity). Next, the effect of the governing parameters on scrubber performance is reviewed. This consists of the effects of inlet gas velocity, bubble size, particle density, liquid properties and liquid volume. Subsequently, the performance of the scrubber is defined as the gas conditions at the scrubber exit and the scrubber removal efficiency. The modelling of a scrubber includes a thermodynamic approach and a heat transfer modelling, where the correlations of bubble size, rising velocity and heat transfer coefficients are explained in detail. Finally, a computational simulation of the bubble column is briefly reviewed.

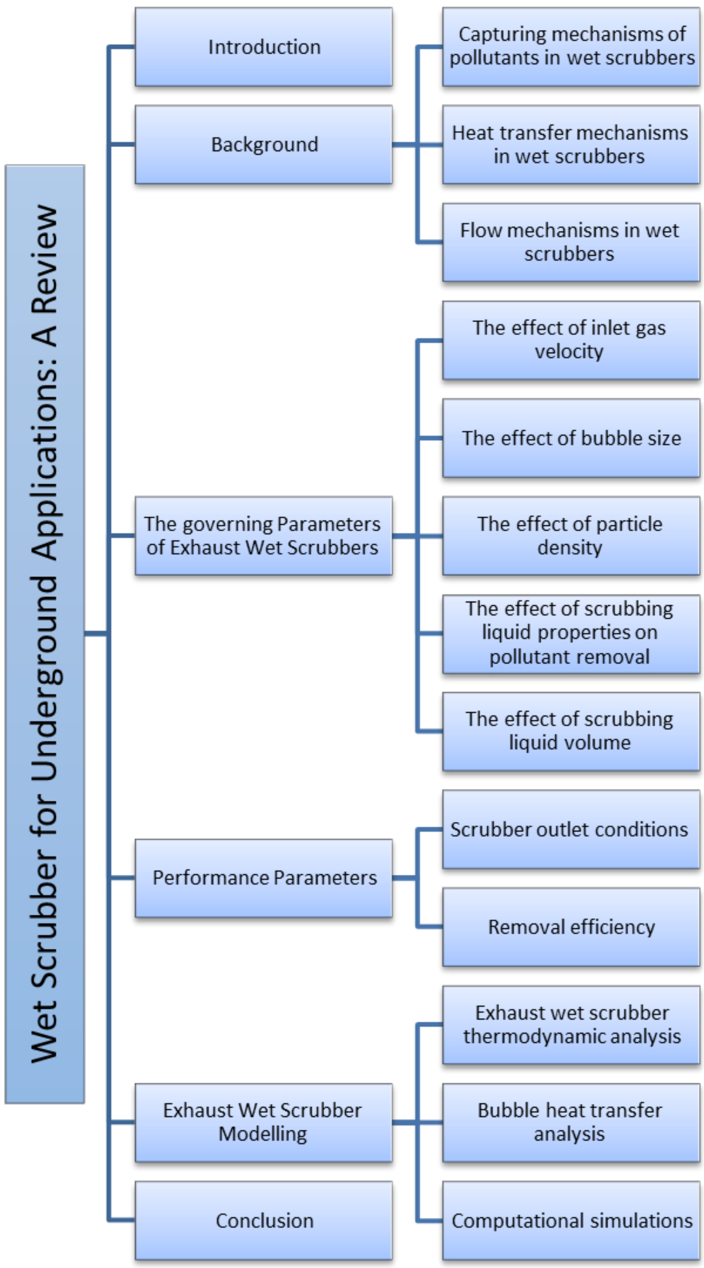

Figure (2-1). The flow chart of review chapter.

2.2. Background

Experts around the world have developed a range of studies concerning scrubber development to reduce PM. Indeed, there are two types of wet scrubbers: those based on liquid droplets and others based on gas bubbles. One example of a gas-bubble based wet scrubber is a wet scrubber for underground applications. This wet scrubber consists of an inlet gases pipe, with an outlet end inserted underneath the scrubbing liquid surface (Figure 2-2). The exhaust gas stream goes through the scrubbing liquid, breaking into bubbles in different shapes and sizes, based on their velocities and locations. These bubbles leave the liquid surface, then the scrubber, through the scrubber exit towards the DPF with lower temperature and higher humidity than the inlet conditions. This design has several advantages, such as strong transfer (for heat and mass), and ease (for operation and construction). Moreover, the absence of moving parts reduces maintenance costs (Youssef 2010), wear and tear (Shaikh and Al-Dahhan 2007).

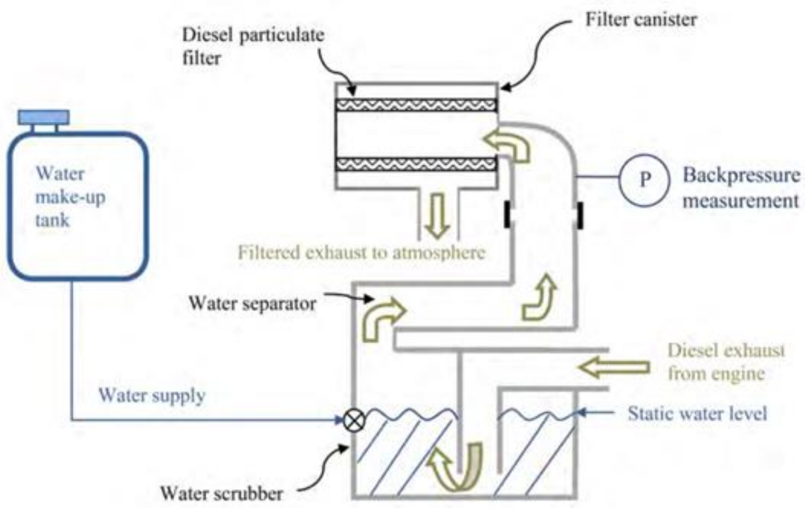

Figure (2-2). Schematic diagram of the exhaust wet scrubber (Rao et al. 2015).

To clarify, the DPF (also known as a particulate trap) is defined as a simple device where particles are trapped. Indeed, more than 80% of particulate matter can be removed based on the filter type. The types of the dry filter are wall-flow monolith, ceramic foam, ceramic fibre trap and sintered metal filters. To explain, Figure (2-3) shows one type of these filters (Rens and Wilde 2005).

Figure (2-3). Diesel particulate filter (Rao et al. 2015).

Wet scrubbers' responsibilities are elimination of sparks before contacting with the surrounding environment, PM filtration and reducing the outlet gas temperatures (Rao et al. 2015). Indeed, the wet scrubber is more effective than other types of scrubbers, even if it is relatively small. Also, these scrubbers can scrub different materials, including those that are sticky, hygroscopic, combustible, explosive, or corrosive (Mussatti and Hemmer 2002). Therefore, Gabriel et al. (Gabriel et al. 2004) converted a wet scrubber into a bio-trickling filter by developing a 10-step procedure. Their experiments confirmed that a bio-trickling filter effectively removes H_2S regardless of concentration.

Although there are several positive aspects of wet scrubbers, they also have negative impacts. Firstly, the increased collection efficiency can lead to cost increments due to a pressure drop across the scrubber. Secondly, there are limits for both the temperature and the flow rate of exhaust gases. Moreover, generating a sludge waste requires treatment or disposal. Another disadvantage is that the moisture presence in the gas stream causes a plume visibility or corrosion in the downstream system (Mussatti and Hemmer 2002).

2.2.1. Capturing mechanisms of pollutants in wet scrubbers

The method of dissolving at least one component of a gas mixture into a liquid is called absorption, which is a feature of the wet scrubber. Two processes occur within this method. The physical process includes dissolving the components by solvent controlled by the properties of solvent and gas and the pollutant-specific temperature (which effects the equilibrium solubility and diffusivity). However, the chemical process represents the reaction between the components and the solvent. Most solvents are liquids, such as water, aqueous solutions and some types of oils such as mineral and nonvolatile hydrocarbon. For economic feasibility, the solvent used to remove pollutants should be low in cost, viscosity and vapour pressure and high in gas solubility. For this reason, water is considered as the most suitable solvent for most applications (Barbour et al. 2002).

Both physical and chemical processes increase by increasing the contact area between the two phases. This contact area depends on bubble size at a constant gas flow rate. Passing gas through an orifice into a liquid pool breaks it up into singular bubbles. Bubble size and shape are dependent on several factors, such as orifice (size and shape), fluid properties and gas velocity. Generally, bubble shape can be classified into three shapes: spherical, elliptical and spherical cap. The transition from spherical to elliptical, and then to spherical cap, results from increasing the gas flow rate within the system. Moreover, bubble size can also increase due to increasing orifice size, viscosity and dissolving an electrolyte concentration in the scrubbing liquid. Bubble size decreases by decreasing surface tension by adding another liquid (such as alcohol) to water (Azzopardi et al. 2011). Furthermore, the liquid height above the orifice has a minor influence on bubble size (Bai 2010).

2.2.2. Heat transfer mechanisms in wet scrubbers

The design and operating principle of the wet scrubber in underground applications is similar to the bubble column reactor. These similarities are flow type, analysis, gas inlet and system types (Figure 2-4). The bubble column reactor is a system containing a large number of gas bubbles in direct contact with the continuum liquid. The gas phase contains some soluble components transferred to the liquid phase (Meikap et al. 2002 and Besagni et al. 2016).

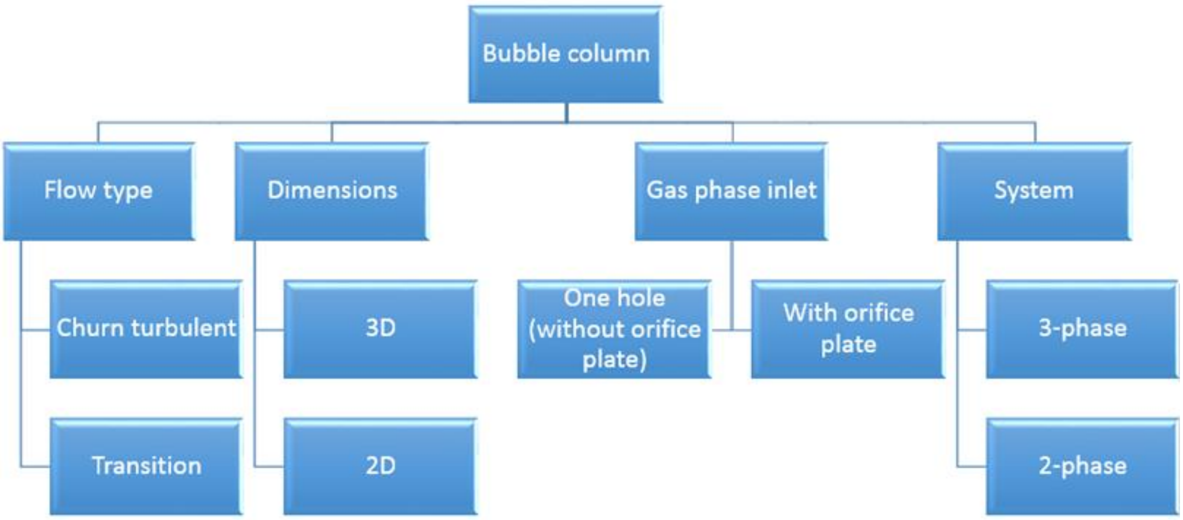

Figure (2-4). Laboratory investigation of bubble column.

Excluding the energies carried by the inlet and outlet gas, heat transfers from the scrubber in several forms: evaporation, condensation and heat loss. Evaporation occurs at the contact area between the liquid and the gas. Condensation and boiling exist in most heat transfer cases of flowing fluid (Lienhard IV and Lienhard V 2011). The phase changes from liquid to gas and vice versa, causing liquid evaporation, in addition to heat and mass transfer. The hydrodynamic behaviour of the wet scrubber is also complex due to significant density compressibility differences in both phases (Mussatti and Hemmer 2002).

Heat transfer coefficient depends on multiple factors: in particular, the liquid properties (temperature variation changes the viscosity) and bubble size (Yang 2000). In other words, bubble motion depends mainly on heat transfer and vice versa, due to direct interactions between bubbles and other structures within the fluid. Indeed, a high heat transfer rate could be achieved by adding particles to the liquid phase (Harris et al. 2004).

Gandhi and Joshi (2010) analysed the heat transfer coefficient of the bubble column. They suggested that the Support Vector Regression (SVR) correlation was better than the empirical and semi-empirical correlations. To explain, their method prediction was more accurate and enhanced for different systems: gas-liquid, a large variety of operating pressures, a wide range of operating temperatures, most velocities of gas and liquid, different column diameters and various liquid heights. Furthermore, Jhawar and Prakash (2007) used fast-response probes in a bubble column to study local heat transfer and dynamics. They added that this reactor should be operated in a heterogeneous region, for high rates of achievement of heat transfer.

2.2.3. Flow mechanisms in wet scrubbers

Three types of flow patterns have been observed in wet scrubbers: homogeneous (bubbly), transitional, and heterogeneous (churn-turbulent). Based on the operating conditions, the most frequently encountered flow region is the churn-turbulent flow (Shaikh and Al-Dahhan 2007). The flow pattern depends mainly on inlet gas velocity, scrubber diameter, and height-to-diameter ratio, in addition to the nature of the gas-liquid system such as pressure, temperature, viscosity, surface tension, solid loading, orifice size, and preformation pitch (Deckwer et al. 1980, Thakre and Joshi 1999, Shaikh and Al-Dahhan 2007) (Figure 2-5). This figure explains how increasing the inlet gas velocity changes the flow region from bubbly to churn-turbulent.

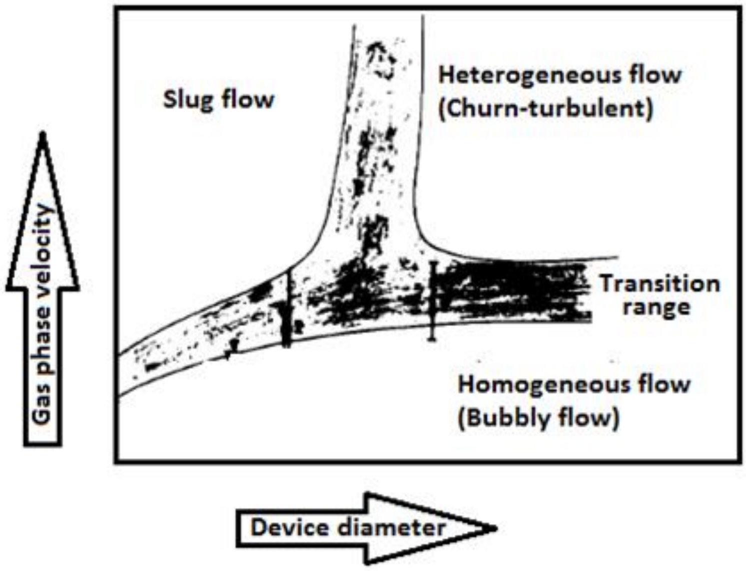

Figure (2-5). Characterising the flow regions in two-phase and slurry column reactors as a function of inlet gas velocity and scrubber dimension (Deckwer et al. 1980).

Each flow region has hydrodynamic characteristics completely different from others, resulting in different mixing as well as mass and heat transfer rates. The homogeneous flow region occurs at low-to-moderate inlet gas velocities. The characteristics of this region are small bubbles of uniform size, travelling vertically with minor transverse and axial oscillations. There is a narrow bubble size distribution without bubble breakup and coalescence. By comparison, heterogeneous flow occurs at high inlet gas velocities. Both small and large bubbles are generated in this flow region, as a result of the intensity of coalescence and breakup, causing wide bubble size distribution. It is called a churn-turbulent region because the large bubbles churn through the liquid (Shaikh and Al-Dahhan 2007). Up flow occurs in the central region of the bubble column, while down flow occurs near the interior surfaces (Thakre and Joshi 1999).

Various experimental techniques have been outlined by Shaikh and Al-Dahhan (2007) to determine the flow region transition. Also, Besagni et al. (2016) explained in detail all possible flow regions in the bubble column and which parameters could affect it. Indeed, flow characteristics might be measured using several techniques such as the photographic method (Giechaskiel et al. 2018), X-ray (Rao et al. 2015), PIV (Kurella et al. 2015, Giakoumis et al. 2017), optical fibre probe (Walsh 2007), conductivity probe (Hoque et al. 2014), pressure transducer (Wang et al. 2005, Higuera and Medina 2006, Situ et al. 2012), electrical capacitance tomography (Lin and Fan 1999) and acoustic probe (Talaia 2007, Rao et al. 2013).

2.3. The governing Parameters of Exhaust Wet Scrubbers

The interrelated bubble parameters, such as bubble velocity, gas-liquid interfacial area and bubble frequency, have a major influence on scrubber performance. Also, other factors affecting scrubber performance include scrubber design (geometry and size), operating conditions (flow rates, temperatures, pressures), and physical properties (Mussatti and Hemmer 2002). Furthermore, particle changes (coagulation and volatility) could occur as a result of their passing through the exhaust system after passing through the engine cylinders (Burtscher 2005).

Non-dimensional numbers can be used to describe the flow and heat transfer mechanisms. This makes the equation independent of equipment shape and size, in addition to properties phases. Seven non-dimensional numbers can be used to investigate wet scrubber performance, namely: Reynolds number (Re), Prandtl number (Pr), Eötvös number (Eo), Eckert number (Ec), Bo, Weber number (We), Stanton number (St) and Nusselt number (Nu) (Table 2-1).

Table (2-1). Non-dimensional numbers that could be valuable in wet scrubber calculations.

No.	Non-dimensional number	Expression	Explanation
1	Reynolds number	$\mathrm{Re} = \frac{uL\rho}{\mu}$	Can be used for the inlet gas and the bubbles inside the scrubber tank. Reynolds number characterises flow regions.
2	Prandtl number	$\mathrm{Pr} = \frac{v}{\alpha}$	Prandtl number is not constant for scrubber fluids because exhaust gases have various concentrations based on engine load and rpm. Also, scrubbing liquids have different properties because both soluble gas and solid particle concentrations increase with time.
3	Bond number Eötvös number (Eo)	$\mathrm{Bo} = \frac{g(\rho_l - \rho_v)L^2}{\sigma}$	Understanding bubble formation mechanisms leads to clarifying heat transfer between the bubbles and surrounding liquid.
4	Eckert number	$\mathrm{Ec} = \frac{u_b^2}{c_p(T_s - T_\infty)}$	This number can be valuable in estimating heat loss through the scrubber.
5	Weber number	$\mathrm{We} = \frac{\rho u_b^2 L}{\sigma}$	This number could be key to the investigation of heat transfer from bubbles.
6	Stanton number	$\mathrm{St} = \frac{h_c}{\rho u_b c_p}$	There is a connection between energy transfer through the scrubber and the liquid thermal properties. Therefore, an ideal scrubbing liquid can be selected based on this number.

7	Nusselt number	$\mathrm{Nu} = \frac{h_c L}{k}$	This number helps to determine bubble and scrubber heat transfer.

2.3.1. The effect of inlet gas velocity

Changing the gas volume flux has a significant effect on scrubber performance (Rao et al. 2015). About 19% absorption of carbon dioxide was caused due to increasing the gas flow rate. Another 10% to 14% increment of absorption was achieved by heating the carbon dioxide. This was based on the heat energy generated from the reaction between water and carbon dioxide. Further, under a certain amount of hydrogen chloride (HCl) concentration, increasing the inlet gas flow rate reduces the removal of HCL (Kurella et al. 2015). Therefore, choosing the scrubber size depends mainly on the inlet gas flow rate (Walsh 2007).

Increasing the inlet gas velocity increases the liquid mixing, reduces bubble size due to high bubble breakup (Youssef 2010) and leads to wider bubble size distribution (Wang et al. 2005). Nevertheless, at low inlet gas velocities, bubble breakup and coalescence were weak, in addition to a narrow distribution being observed (Wang et al. 2005). However, the excessive turbulence and high inlet gas flow rate ejected more liquid from the scrubber exit. This damages the post-scrubber diesel particulate filter, in addition to increasing the maintenance time (Hoque et al. 2014). Usually, underground diesel equipment operates in a continually varied operating condition. Therefore, all these parameters can be expected.

2.3.2. The effect of bubble size

Bubble size and shape are dependent on different factors, such as orifice (size and shape) fluid properties and gas velocity. Bubble shapes can generally be classified into three kinds: spherical, elliptical and spherical cap (Figure 2-6). The transition from spherical to elliptical, and then to spherical cap, is a result of increasing the gas flow rate within the system. Bubbles have spherical shapes for small sizes, and an elliptical one for sizes larger than that; reaching the shape of part of sphere (Azzopardi et al. 2011).

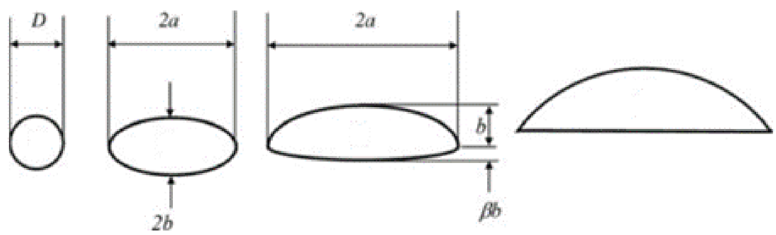

Figure (2-6). Bubbles' shape (Azzopardi et al. 2011).

Wet scrubber performance depends on bubble size because a larger bubble surface area transfers more heat. To explain, Higuera and Medina (2006) investigated bubble generation and coalescence in a quiescent inviscid liquid, using the formulation of potential flow. They injected a constant gas flow rate vertically upward into the liquid. Their results show that bubbles have a constant volume at a low Weber number because bubble growth depends on inertia and buoyancy forces. However, at a high Weber number, this growth was led by the interaction among the bubbles. Moreover, increasing the inlet gas velocity reduces the average bubble diameter (Bandyopadhyay and Biswas 2006). Conversely, bubble size could be reduced as a result of a pressure increment (Lin and Fan 1999). In the scrubber, the inlet gas injects underneath the liquid surface at a variable rate, so the bubbles have non-uniform shapes. Thus, investigating this particular parameter is extremely complex.

2.3.3. The effect of particle density

PM loading is known as dust loading and it is defined as the mass of PM per unit volume at the scrubber inlet. Also, the removal efficiency decreases as the fly-ash loading increases (Bandyopadhyay and Biswas 2006). Furthermore, Guo and Gao (2008) used a wet scrubber to remove both SO_2 and NO_2 using limestone slurry including several operating parameters. Their operating parameters were reaction temperature, oxygen amount in flue gas, and inlet concentration of SO_2 and NO_2. Further, Guo and Gao (2008) claimed that minimising the concentration of the inlet NO_2, the amount of O_2 in the flue gas, and the reacting temperature, reduces the removal efficiency of SO_2. Nevertheless, the NO_2 absorption was increased due to increasing the concentration of the inlet SO_2 and reducing the reaction temperature and the flue gas oxygen. Indeed, the collection efficiency depends on the particle size. Therefore, higher efficiency can be achieved with large particle sizes (Mussatti and Hemmer 2002, Bandyopadhyay and Biswas 2006). Also, for underground diesel equipment, PM depends on fuel type (Rakopoulos et al. 2015) and operating conditions.

2.3.4. The effect of scrubbing liquid properties on pollutant removal

Pollutant diffusion occurs when the liquid has less pollution than the gaseous component (Barbour et al. 2002). For instance, Bhadra et al. (2014) experimentally tested a wet scrubber using a water solution and other components to collect solid particles. Their experiments were conducted by wetting solid particles through direct contact with liquid. After absorption, the solid particles dissolved in the liquid or created a colloidal form that settled down. It was observed that mixing carbonate of calcium (limestone) with exhaust gases from the engine gave a higher emission reduction. In another example, Talaia (2007) experimentally tested the bubble rising velocity in a single column using two liquids (water and glycerol). They suggested that this velocity depended mainly on drag force rather than buoyancy.

The most suitable absorption liquid can be chosen after considering several factors. These factors are availability, cost, pollutant concentrations, removal efficiency, requirements for handling exhaust gas capacity and the recovery value of pollutants. Adding coolants such as urea ($(NH_2)_2CO$) to the scrubbing liquid increases its boiling temperature and life. Indeed, the removal efficiency increases for a limited time (Bhadra et al. 2014). Therefore, it is key point to consider this effect in any underground exhaust wet scrubber investigation.

2.3.5. The effect of scrubbing liquid volume

High scrubbing liquid levels inside the scrubber lead to a 25% reduction in PM emissions (Pratt et al. 1998). However, increasing the liquid level inside the scrubber also increases the liquid leaving the scrubber from the scrubber exit (Rao et al. 2013). The investigation of underground wet scrubber performance should consider this factor to determine which one of these two options is more important.

2.4. Performance Parameters

2.4.1. Scrubber outlet conditions (particularly temperature and humidity)

Reducing the outlet gas temperature is an important role of the wet scrubber. Also, it eliminates sparking possibility at the exhaust (Rens and Wilde 2005). Indeed, increasing the outlet gas temperature reduces the corresponding relative humidity. Equally importantly, liquid evaporation causes most of the scrubbing liquid transportation from the scrubber. This evaporation depends on the inlet gas temperature, while a small amount of the liquid leaves the scrubber due to the aerodynamic process. Another 2-8% of water generates from the combustion and carried by exhaust gas. This percentage is not constant and it is affected by both engine load and speed (Rao et al. 2015). The outlet gas temperature and relative humidity increase with time and any type of thermal energy leaving or entering the scrubber depends on engine rpm (Shaikh and Al-Dahhan 2007).

2.4.2. Removal efficiency

Removal efficiency depends strongly on scrubber configuration and the liquid (Rens and Wilde 2005). It is defined as the number of molecules of a compound removed or destroyed in a system relative to the number of molecules that entered the system:

$$\eta = \frac{C_{in} - C_{out}}{C_{in}}, \tag{2-1}$$

where: C_{in} is the concentration of any component that enters the system and C_{out} is the concentration of any component that leaves the system.

Or (Van Setten et al. 2001):

$$filtration\ efficiency = \frac{Particles\ downstream\ trap}{Particles\ upstream\ trap}\ \mathrm{X}\ 100\%. \tag{2-2}$$

Researchers studied the removal efficiency extensively to reduce the emission. For instance, Tokumura et al. (2016) effectively removed indoor air pollutants using a wet scrubber coupled with the photo-Fenton reaction. This reaction consists of a series of reactions between H_2O_2 at acidic value and Fe(II)/Fe(III) (Huang 2013). Indeed, a high increment in removal efficiency was achieved using this technique (Machulek et al. 2012, Ebrahiem 2017). Also, D’Addio et al. (2013) experimentally tested an electronic wet scrubber by spraying tap water to remove both fine and ultrafine particles from combustion gases. Using a system charging, a 30% increment was achieved in removal efficiency. Therefore, hydrodynamic interaction is less effective than electrostatic interaction. More importantly, high removal efficiency is achieved due to bubbles bursting (Meikap 2002).

2.5. Exhaust Wet Scrubber Modelling

2.5.1. Exhaust wet scrubber thermodynamic analysis

An energy balance can be applied to a wet scrubber with thermodynamic analysis. It balances inlet and outlet masses, in addition to inlet and outlet energies (Figure 2-7) and equation (2-3)(Hoque et al. 2014):

$$\dot{E_{in}} = \dot{E_{out}} + \dot{E_{\Delta v}} + Q_L + \dot{E_w}, \tag{2-3}$$

where: $\dot{E_{in}}$ is the inlet energy of exhaust gases from the diesel engine (kW), $\dot{E_{out}}$ is the outlet gas energy leaving the scrubber from its exit (kW), $\dot{E_{\Delta v}}$ is the energy lost because of changing the liquid volume (due to evaporation) (kW), Q_L is the heat transfer from the scrubber to the surrounding environment through all scrubber surfaces (kW), and $\dot{E_w}$ is the energy stored inside the scrubber (kW).

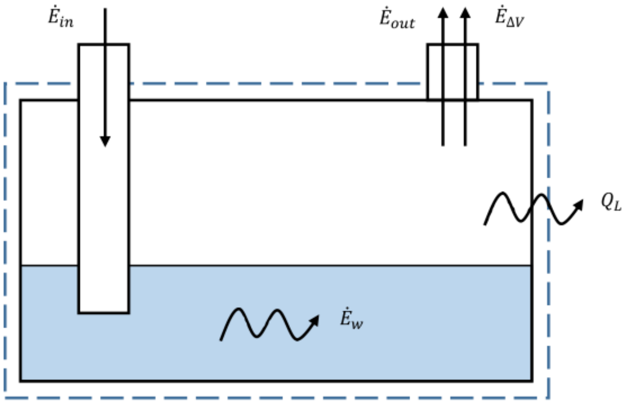

Figure (2-7). Energy balances for the exhaust wet scrubber (Hoque et al. 2014).

The calculations of inlet energies and outlet energies must be based on the components of the exhaust gases. These components are carbon dioxide, water vapour, oxygen, and nitrogen (Equation 2-4):

$$\mathrm{C_{12}H_{23}} + 26.625(\mathrm{O_2} + 3.76\mathrm{N_2}) = 12\mathrm{CO_2} + 11.5\mathrm{H_2O} + 8.875\mathrm{O_2} + 100.11\mathrm{N_2}. \qquad (2\text{-}4)$$

Therefore, inlet energy consists of the inlet energy of each component as:

$$\dot{E_{in}} = \left(\dot{m_{\mathrm{CO_2}}} c_{p_{\mathrm{co_2}}} T\right)_{in} + \left(\dot{m_{\mathrm{O_2}}} c_{p_{\mathrm{o_2}}} T\right)_{in} + \left(\dot{m_{\mathrm{N_2}}} c_{p_{\mathrm{N_2}}} T\right)_{in} + \left(\dot{m_{\mathrm{H_2O}}} c_{p_{\mathrm{H_2O}}} T\right)_{in} \qquad (2\text{-}5)$$

Or:

$$\dot{E_{in}} = \left(\dot{m_{\mathrm{CO_2}}} h_{\mathrm{co_2}}\right)_{in} + \left(\dot{m_{\mathrm{O_2}}} h_{\mathrm{O_2}}\right)_{in} + \left(\dot{m_{\mathrm{N_2}}} h_{\mathrm{N_2}}\right)_{in} + \left(\dot{m_{\mathrm{H_2O}}} h_{\mathrm{H_2O}}\right)_{in} \qquad (2\text{-}6)$$

Similarly, the outlet energy from the wet scrubber exit represents the entire mixture:

$$\dot{E_{out}} = \left(\dot{m_{\mathrm{CO_2}}} c_{p_{\mathrm{co_2}}} T\right)_{out} + \left(\dot{m_{\mathrm{O_2}}} c_{p_{\mathrm{o_2}}} T\right)_{out} + \left(\dot{m_{\mathrm{N_2}}} c_{p_{\mathrm{N_2}}} T\right)_{out} + \left(\dot{m_{\mathrm{H_2O}}} c_{p_{\mathrm{H_2O}}} T\right)_{out}, \qquad (2\text{-}7)$$

Or:

$$\dot{E_{out}} = \left(\dot{m_{\mathrm{CO_2}}} h_{\mathrm{co_2}}\right)_{out} + \left(\dot{m_{\mathrm{O_2}}} h_{\mathrm{O_2}}\right)_{out} + \left(\dot{m_{\mathrm{N_2}}} h_{\mathrm{N_2}}\right)_{out} + \left(\dot{m_{\mathrm{H_2O}}} h_{\mathrm{H_2O}}\right)_{out} \qquad (2\text{-}8)$$

where: $\dot{m}$ is the gas mass flow rate (kg/s), c_p is the specific heat capacity, (kJ/kg·K),), T is the temperature (K), h is the specific enthalpy for the gas or water vapour (kJ/kg), *in* is the scrubber inlet and *out* is the scrubber outlet.

Further, by combining the energy loss due to liquid evaporation with the liquid that leaves the wet scrubber (because it is carrying some energy), the energy loss due to changing the liquid volume can be calculated from:

$$\dot{E_{\Delta v}} = \left(\dot{m_{w_{out}}} - \dot{m_{w_{in}}}\right)\left(h_{fg} + c_{p_f}(T_{out} - T_w)\right) + \left(\frac{dW}{dt} - \dot{m_{w_{out}}} + \dot{m_{w_{in}}}\right)\left(c_{p_f}(T_{out} - T_{in})\right), \tag{2-9}$$

where: h_{fg} is the liquid latent heat (kJ/kg), $\frac{dW}{dt}$ is the mass change rate of liquid (kg/s), and c_{p_f} is the liquid specific heat capacity (kJ/kg·K).

The liquid temperature increases as a result of heat transfer from the inlet gas. This energy stores in the liquid and can be calculated as:

$$\dot{E_w} = m_w c_{p_w} \frac{dT_w}{dt}, \tag{2-10}$$

where $\frac{dT_w}{dt}$ is the liquid temperature changing rate (K/s).

Moreover, the heat loss from the scrubber can be estimated in several methods. These methods are discussed in detail in the thermodynamic analysis chapter. Simply, this heat loss can be calculated based on heat transfers from all scrubber components to the ambient environment due to their temperature difference (Equation 2-11).

$$Q_L = h\,A(T - T_a) = mc_p \frac{dT}{dt} \tag{2-11}$$

2.5.2. Bubble heat transfer analysis

Heat transfer analysis of the wet scrubber investigates the bubbles in the scrubber, their formation mechanism, their growth with time and height and the heat transfer mechanism between the bubbles and their surrounding liquid.

The bubble heat transfer coefficient greatly depends on the two-phase flow region (Deckwer et al. 1980, DeGuzman et al. 1997). One of several classifications of two-phase mixtures is based on their combinations of gas, liquid, solid phases and plasma. In the wet scrubber, all these types exist except plasma. The variations in the two-phase flow occur due to phase combinations and varied interface structures (Ishii and Hibiki 2006).

In scrubber investigation, the influence of all forces acting on bubbles must be considered. Single bubbles do not exist in wet scrubbers due to the nature of the high gas flow rate. However, the heat transfer analysis of the wet scrubber could begin by studying a single bubble, then expanding to multiple bubbles with various sizes and shapes. Forces that affect the bubble vertically are drag force, buoyancy, virtual mass force, and gravity (Deckwer et al. 1980, Xu 2004, Wang and Dong 2009). These forces equal bubble mass multiplied by acceleration, according to Newton's second law of motion as follows:

$$m \cdot a = P + F_D + F_V + F_G, \tag{2-12}$$

where: P is the pressure force, F_D is the drag force, F_V is the virtual mass force, F_G is the gravity force (all forces in (N)), m is the bubble mass (kg) and a is the bubble acceleration (m/s^2).

Pressure forces direct an object upward in liquid due to pressure difference between the top and the bottom of that object. It is equal to the fluid weight displaced by the body:

$$P = G_l = \rho_l g V_{\mathrm{b}}, \tag{2-13}$$

where: V_{b} is the bubble volume (m^3).

The liquid resistance to bubble movement is called a drag force that can be calculated as:

$$F_D = -\tfrac{1}{2}\rho_l C_D \left|u_l - u_g\right| \left(u_g - u_l\right) s_a, \tag{2-14}$$

where: C_D is the drag coefficient due to drag force, and s_a is the bubble front face area (m^2).

Rising bubbles accelerate their surrounding liquid and generate another virtual mass force. This force increases inertial mass effectiveness and interrupts the continuous phase acceleration. However, the virtual mass force can be neglected if the dispersed phase density far outweighs the continuous phase:

$$F_V = \frac{1}{2} V_{\mathrm{b}} \rho_l \frac{d}{dt}\left(u_l - u_g\right) \tag{2-15}$$

Finally, the gravity force acting on the bubble is calculated as:

$$F_G = -m_{\mathrm{b}} g = -\rho_g V_{\mathrm{b}} g. \tag{2-16}$$

2.5.2.1. Bubble size

Bubble motion depends mainly on the bubble's volume (Wang and Dong 2009). Therefore, it is important to investigate this factor to improve scrubber performance. Indeed, bubble volume is calculated from the force balance mentioned in the previous section. On the other hand, the gas flow rate has no effect on bubble volume in a static region (at a small gas flow rate), due to neglecting the two-phase momentums. In the turbulent region, large bubbles shatter into small ones because they cannot survive against the gas turbulence (Xu 2004). Table (2-2) demonstrates some correlations of both dimensional and non-dimensional bubble diameter. This table might be valuable for estimating the bubble diameter in a scrubber. In particular, the correlation proposed by Levich (1962) concerns a churn-turbulent region and the Martínez-Bazán et al. (1999) concerns turbulent flow. At a constant inlet gas velocity, the correlation of the Davidson and Schüler (1999) equation can calculate the bubble diameter without including the fluid properties. Bubble shape can be assumed as spherical or elliptical based on the flow type.

Table (2-2). Bubble size correlations.

No.	Author/Researcher	Correlation	Condition/Technique
1	Leibson et al. (1956)	$d_b = 0.28\ \mathrm{Re}^{-0.05}$	Departure bubble diameter from a single orifice in a turbulent flow Re > 10,000.
2	Davidson and Schüler (1960)	$V_b = 1.722\ \frac{Q'^{\frac{4}{5}}_g}{\mathrm{g}^{\frac{3}{5}}}$	For a constant flow rate at the orifice without including the inviscid liquid properties and surface.
3	Levich (1962)	$d_{max} \approx \frac{3.63\sigma}{u_b^2 \sqrt[3]{\rho_l^2 \rho_g}}$	Churn-turbulent flow region.
4	Wallis (1969)	$d_b = \left[\frac{6 d_o \sigma}{\mathrm{g}(\rho_f - \rho_g)}\right]^{1/3}$	At the orifice diameter comparable with the bubble radius is: $d_0 > \left[\frac{\sigma}{\mathrm{g}(\rho_f - \rho_g)}\right]^{1/2}$
5	Moalem and Sideman (1973)	$\beta = \left[1 - \frac{3}{2}\left(\frac{k_v}{\pi}\right)\tau\right]^{\frac{2}{3}}$ $\beta = \left[1 - \frac{5}{4}\left(\frac{k_v}{\pi}\right)^{\frac{1}{2}}\tau\right]^{\frac{4}{5}}$	Combining the effect of bubble rising velocity and mainstream cross flow to investigate the collapse for pure vapour and at constant bubble velocity. The 1st correlation for a bubble diameter of 0.4–0.8 cm. The 2nd correlation for a bubble diameter of less than 0.2 cm.
6	Anagbo (1991)	$V_b = 0.7\left[\frac{\rho_g}{\rho_f}\right]^{-1/4}\left[\frac{d_0}{2g}\right]^{1/2} Q'_g$	Ellipsoidal bubble formation at free-standing nozzle.
7	Martínez-Bazán et al. (1999)	$d_{max} = \left[\frac{12\sigma}{\beta' \rho_l}\right]^{3/5} \varepsilon^{-2/5}$	The breaking up of injected bubbles into fully developed turbulent flows based on Kolmogorov concept.
8	Lehr and Mewes (2001)	$d_{max} = 2^{1/5} \frac{\sigma^{3/5}}{\rho_l^{3/5} \varepsilon^{2/5}}$	Following the idea of Levich (1962).
9	Zhang et al. (2008)	$d_b = \sqrt[3]{\frac{6Q'_g}{\pi n}}$	The unsteady motion of single bubble rising freely in a quiescent high viscous liquid. The volumetric gas rate and the number of generated bubbles per unit time were used to calculate the bubble volume based on spherical shape assumption.

2.5.2.2. Bubble motion

The rising velocity of a single bubble depends on buoyancy and drag forces. These forces are functions of gravity, fluid properties and equivalent diameters. Dynamic viscosity has a strong effect on terminal velocity (Talaia 2007). Bubble acceleration affects the total drag coefficient (Zhang et al. 2008). Similarly, a slip occurs at the liquid-vapour interface, and liquid cleanliness can be determined by measuring small bubbles (Parkinson et al. 2008). Also, bubble velocity increases due to the bubble size increment. Moreover, the bubble drag coefficient and the aspect ratio decrease with an increasing Reynolds number (Raymond and Rosant 2008). For more details, Table (2-3) shows several correlations to predict bubble rise velocities. It contains some of the most widely used correlations (Kantarci et al. 2005). Indeed, some correlations in Table (2-3) should be examined carefully for their suitability for the scrubber, especially those on Lines 3-5, and 8. For this purpose, a three-dimensional bubble movement should be considered to achieve more accurate results.

Table (2-3). Bubble rising velocity correlations.

No.	Author/ Researcher	Correlation	Condition/ Technique
1	Davies and Taylor (1950)	$u_b = 0.78\sqrt{gR'}$	For very large single isolated bubbles under constant pressure.
2	Moalem and Sideman (1973)	$R'' = -\frac{k\Delta T}{\rho_v \lambda}\left[\frac{2u_r k_v}{\pi \alpha R}\right]^{\frac{1}{2}}$	Collapse for un-pure vapour radius-dependent rising velocity obtained using a simple energy balance by assuming a quasi-steady state.
3	Krishna et al. (1994)	$\frac{u_{b,sm}\mu_l}{\sigma} = 2.25\left(\frac{\sigma^3\rho_l}{g\mu_l}\right)^{-0.273}\left(\frac{\rho_l}{g\rho}\right)^{0.03}$; $\frac{u_{b,lg}\mu_l}{\sigma} = \frac{u_{b,sm}\mu_l}{\sigma} + 2.4\left(\frac{(V_g - V_{g,trans})\mu_l}{\sigma}\right)^{0.757}$, $\left(\frac{\sigma^3\rho_l}{g\mu_l^4}\right)^{-0.077}\left(\frac{\rho_l}{g\rho}\right)^{0.077}$, $\frac{V_{g,trans}}{u_{b,sm}} = 0.5\,exp\left(-193\rho_g^{-0.61}\mu_l^{0.5}\sigma_l^{0.11}\right)$	For a bubble column reactor for different gas densities.
4	Delnoij et al. (1997)	$u_b = \sqrt{\frac{\frac{8}{3}(\rho_g - \rho_l)R_b g}{C_D \rho_l}}$ $C_D = \frac{24}{Re}(1 + 0.15\mathrm{Re}^{0.687})$ For Re < 1000. $C_D =$ 0.44 for Re ≥ 1000.	Small spherical time-dependent two-dimensional gas bubble in a homogeneous region.
5	Tomiyama et al. (1998)	$u_b = \sqrt{\frac{2\sigma}{\rho_L d} + \frac{\Delta\rho g d}{2}}$	For a single bubble under normal and micro gravity effect.
6	Tomiyama et al. (2002)	$u_T = \frac{\sin^{-1}\sqrt{1 - AR^2} - AR\sqrt{1 - AR^2}}{1 - AR^2}\sqrt{\frac{8\sigma}{\rho_l d}AR^{4/3} +}$	For a single bubble rising through an infinite stagnant liquid in surface tension including surfactant

			concentration effects.
7	Chen (2004) ; Ali (2014)	$\mathrm{Re}_b = \frac{\rho_l \lvert u_l - u_g \rvert d_b}{\mu_l}$	For a single spherical bubble rising at a steady state.
8	Talaia (2007)	$u_b = (0.694 \mp 0.021)\left[\frac{\mathrm{g} d_e \Delta\rho}{\rho_l}\right]^{1/2}$	Re = 3425–7490 & C_d = 2.68–2.76
		$u_b = \left[0.289\frac{g d_e \Delta\rho}{\rho_l} + 877.193\frac{\mu_l g^{1/2}}{\rho_l d_e^{1/2}}\right]^{1/2}$	Re = 695–3425 & d_e = 0.31–1.34 cm
		$u_b = (1.5 \mp 0.045)\left[\frac{g d_e \Delta\rho}{\rho_l}\right]^{1/2}$	Re = 255–695 & d_e = 0.14–0.31 cm
		$u_b = 0.415\frac{g d_e \Delta\rho}{\rho_l} - \left[0.529\frac{g^{1/2}\mu_l}{\rho_l d_e^{1/2}} - 2.386 \times 10^{-2}\frac{g d_e \Delta\rho}{\rho_l}\right]^{1/2}$	Re = 1.3–8.3, d_e = 1.85–3.9 cm & C_d = 9.1–38.1

2.5.2.3. Bubble heat transfer

Bubble heat transfer rate is influenced by several factors, such as bubble size, bubble orientation, temperature, and the physical properties of both gas and liquid (Gandhi and Joshi 2010). Heat transfer increases with increasing the inlet gas velocity and the working pressure (Lin and Fan 1999). Simply, the heat transfer can be calculated from the energy balance at the interface of the bubble by assuming the bubble to have a spherical shape. This heat transfer can be expressed mathematically (Davidson and Schüler 1997):

$$(-q")(4\pi R^2) = (\rho_g h_{fg})\left(\frac{dV_b}{dt}\right) \tag{2-17}$$

Subsequently, the heat transfer coefficient can be calculated from correlation (Chen and Mayinger 1992):

$$h_c = \frac{-k(\frac{\partial T}{\partial y})W}{T_W - T_\infty}. \tag{2-18}$$

Indeed, the heat transfer coefficient can become more complex during rising motion. Therefore, Equation (2-17) can be re-written (Chen and Mayinger 1992):

$$h_c = -\frac{\rho_g h_{lg} V_b}{\frac{1}{2} A_b (T_W - T_\infty) t_k}, \tag{2-19}$$

where: h_c is the heat transfer coefficient and t_k is the condensation time(s).

Moreover, the heat transfer can be calculated using other correlations. Some of them were reported by Gandhi and Joshi (2010) (Table 2-4). The most suitable correlations for this scrubber are Nos. 6-7, 9 and 14-15 due to the similarities in flow and system.

Table (2-4). Heat transfer correlations.

No.	Author/ Researcher	System	Correlation	Conditions
1	Fair et al. (1962)	Air-water	$h_c = 1200 u_b^{0.22}$	For vessel size at least 18" and superficial gas velocity = 0–0.5ft/s.
2	Mikic and Rohsenow (1969)		$q = \frac{2k\Delta T\sqrt{n_b}}{\sqrt{\pi\alpha}}$ $\left(\frac{q}{A}\right)_{nc} = 0.54\rho_l c_{pl}\left[\frac{\gamma g (T_W - T_\infty)^5 \alpha^3}{\sqrt{A_{total}} v}\right]^{1/4}$ $\left(\frac{q}{A}\right)_{nc} = 0.14\rho_l c_{pl}\left[\frac{\gamma g (T_W - T_\infty)^4 \alpha^2}{v}\right]^{1/3}$	For pool boiling with heating surface. The 2nd correlation is for pool boiling in a laminar range $10^5 < \mathrm{Ra} < 2 \times 10^7$ The 3rd correlation is for pool boiling in a turbulent range $2 \times 10^5 < \mathrm{Ra} < 3 \times 10^{10}$.
3	Moalem and Sideman (1971)	Non-homogenous distribution	$q = q_o\sqrt{K_v}$, $q_o = \frac{k(T_W - T_\infty)}{R\sqrt{\pi}}\sqrt{\frac{2RU_\infty}{\alpha}}$, $K_v = 0.25\,\mathrm{Pr}^{-\frac{1}{3}}$	For bubble condensation.
4	Theophanous and Fauske (1973)	Liquid-metal vapor	$q = k_l\sqrt{\frac{2U_\infty}{\pi\alpha_l R}}(T_W - T_{l\infty})$, $Q = 4\pi R^2 q = 4k_l\sqrt{\frac{2\pi U_\infty R^3}{\alpha_l}}(T_W - T_{l\infty})$	For single large vapor bubble condensates in a cool liquid.
5	Moalem and Sideman (1973)		$\mathrm{Nu} = \frac{2}{\sqrt{\pi}}(k_v \mathrm{Pe})^{1/2}$	For a single bubble in a single and two-component system.
6	Hart (1976)	Air-water, Air-ethylene	$h_c \propto \frac{u_b^{0.25} g^{0.25} \rho^{0.75} c_p^{0.4} k^{0.6}}{\mu^{0.35}}$	For bubble-agitated system with *U*s > 0.00159 ft/s.
7	Ozisik and Kress (1978)	UO_2 & Sodium	$h_c(t) = \frac{q(t)}{T_\infty - T_W(t)}$ $Q_{0\to t} \cong (T_\infty - T_W(t)) h_c t$	Large rising vapour-gas bubble condensation in a hypothetical core.

		vapours containing non-condensable fission gas.		
8	Deckwer et al. (1980)	Nitrogen-xylene, Kogasin, decalin, nitrogen-paraffin-powdered Al_2O_3	$\mathrm{St} = 0.1[(\mathrm{ReFrPr}^2)^{-0.25}]$	Based on Kolmogoroffs theory of isotropic turbulence and u_r = 0.003–0.04 m/s.
9	Hikita et al. (1981)	Air-water Air-butanol Air-sucrose methanol	$h_c = 0.411 g^{0.308} u_g^{0.149} c_p^{0.333} k^{0.667} \rho^{0.69}$ $\frac{h_c}{\rho_l u_g c_p}\left(\frac{c_p \mu_l}{k}\right)^{0.66} = 0.268\left(\frac{u_g^3 \rho_l}{\mu_l g}\right)^{-0.303}$	1st condition $5.4 \times 10^{-4} < \frac{u_g \mu}{\sigma} < 7.6 \times 10^{-2}$ 2nd condition $4.9 < \frac{c_p \mu}{k} < 93$ 3rd condition $7.7 \times 10^{-12} < \frac{\mu^4}{\rho \sigma^4} g < 1.6 \times 10^{-6}$
10	Saxena (1989)	Air-water, air-water-magnetic	$h_{c,max} = 0.12\left(\frac{\rho g^2}{\mu}\right)^{1/6}\left(\frac{\rho - \rho_g}{\rho}\right)^{1/3}(k \rho c_p$	For a cylindrical probe immersed in a bubble column and u_g = 0.015–0.333 m/s.
11	Chen and Mayinger (1992)	Ethanol, propanol, R113 an water	$\mathrm{Nu} = 0.6\ \mathrm{Re}^{0.6}\mathrm{Pr}^{0.5}$ $\mathrm{Nu} = 0.185\ \mathrm{Re}^{0.7}\mathrm{Pr}^{0.5}$	At the detachment moment: The 1st correlation is for bubble growing period (formation). The 2nd correlation is for bubble collapsing period (bubble rising).
12	Yang et al. (2000)	Nitrogen-Paratherm NF heat transfer fluid-glass beads	$\mathrm{St} = 0.037\left[\mathrm{ReFrPr}^{1.87}\left(\frac{\varepsilon_g'}{1 - \varepsilon_g'}\right)\right]^{-0.22}$	For slurry bubble columns with P ≤ 4.2 MPa and T ≤ 81 °C.
13	Cho et al. (2002)	Air-viscous fluid	$h_c = 11710 u_g^{0.445} \mu_l^{-0.06} P^{0.176}$	For pressurised bubble columns with gas velocity =0-0.12 m/s, pressure=0.1-0.6 MPa & liquid viscosity =1-38 mPa.s
14	Lee et al. (2003)	R11	$Q = \dot{m} h_{fg} = 4\pi \rho_v h_{fg} R^2 \frac{dR}{dt}$	For partial nucleate boiling on a constant wall temperature microscale heater.
15	Jhawar and Prakash (2007)	Air-tap water	$h_c = 8.65\left[\frac{u_g}{\epsilon_g}\right] + 1.32$	For a bubble column using a fine and a coarse gas distributor:

		$h_c = 2\left[\frac{u_g}{\epsilon_g}\right] + 3.3$	The 1st correlation is for $\frac{u_g}{\epsilon_g} \leq 0.3$ m/s The 2nd correlation is for $\frac{u_g}{\epsilon_g} > 0.3$ m/s.
16	Leong et al. (2017)	$q'' = h_{fg}\rho_g^{1/2}[\sigma(\rho_l - \rho_v)]^{1/4}\left[\frac{1+\cos\beta}{16}\right] \times \left[\frac{2}{\pi}(1-\sqrt{\phi})\frac{r+\cos\beta}{1+\cos\beta} + \frac{\pi}{4}(1-\sqrt{\phi})^{1/2}(1 + \cos\beta'')\cos\phi'\right]^{1/2}$	Critical heat flux for pool boiling by adopting the force balance approach including the effects of capillary wicking force and the modified Taylor wavelength.

2.5.3. Computational simulations

Two-phase flow analysis usually starts from general principles that govern all matter behaviour, in particular mass, momentum, and energy conservation because they can be expressed mathematically at any time and in any position (Munkejord et al. 2008). Wallis (1969) is considered to be the first scientist who used the one-dimensional drift flux to analyse the fluid flow.

Several studies focused on simulating bubble columns (Table 2-5). Different computational fluid dynamics methods were used to study the bubble column hydro-dynamically. For example, Direct Numerical Simulation (DNS) describes the whole flow physics using the Volume of Fluid (VOF) approach in software such as FLUENT (Akhtar 2007) and OpenFOAM (Andras et al. 2009). Therefore, special algorithms are necessary for fluid interfaces, tracing between continuous and particle, as well as a very fine mesh grid to garner all time and length scales.

The interface motion can be modelled using different methods (Khan 2014), for example, Eulerian-Lagrangian (E-L), Eulerian-Eulerian (E-E) and two-dimensional and transient study of a single particle (Lapin and Lübbert 1994). Different turbulence models adopted the E-E method, such as the Reynolds Stress Model (RSM), large eddy simulation (Ekambara and Dhotre 2010), explicit algebraic Reynolds stress model, baseline models (Masood et al. 2014), and multi-fluid turbulence model (Ali 2014). Solving the motion equations for individual bubbles, or bubble tracking describes the gas phase (Monahan 2007).

Table (2-5) Computational Simulations

No.	Researcher	CFD Models technique
1	Wallis (1969)	1D, drift flux.
2	Jacobs and Mqajor (1982)	Bubble collapse, three phase, heat transfer model and quasi-steady integral boundary layer approach.
3	Thakre and Joshi (1999)	Gas-liquid system, drag force and radial lift force, 2D, transient, E-E, k− ε model, constant slip velocity and Magnus force.
4	Glover et al. (2000)	Fluent and algebraic slip mixture model.
5	Pfleger and Becker (2001)	3D, E-E, single phase, k− ε model.
6	Ekambara and Joshi (2003)	3D.
7	Mouza et al. (2004)	Population balance, coalescence and break-up models, homogenous region and air-water system.
8	Chen (2004)	Coalescence models, Euler-Euler, ASMM, bubble population balance equation and churn-turbulent region.
9	Deen et al. (2004)	Multi-scale modelling, and Euler–Lagrange model.
10	Ekambara et al. (2005)	1D, 2D, 3D and k–ε model.
11	Wu et al. (2005)	Cross-correlation function analysis and three regions.
12	Zhang et al. (2006)	CFX-4.4., sub-grid scale model, turbulence in k–ε model.
13	Wang et al. (2006)	Computational fluid dynamics–population balance model (CFD-PBM) coupled model and bubble coalescence and breakup.
14	Law et al. (2006)	Fluent 6.2, 2D, 3D and gas-liquid flow.
15	Mousavi et al. (2007)	3D, FLUENT, kinetic model and gas-liquid interactions.
16	Akhtar (2007)	Volume-of-fluid (VOF) approach in FLUENT.
17	Kulkarni et al. (2007)	LDA measurements and 2D.
18	Tabib et al. (2008)	3D, transient CFD, Reynolds Stress Model and three different turbulence closure (k–ε, RSM and Large Eddy Simulation (LES)) models.
19	Bhole et al. (2008)	Finite volume, Eulerian framework, CFD-PBM approach and axisymmetric steady state flow.

20	Díaz et al. (2008)	Eulerian-Eulerian approach, transient two-phase flow and MUSIG model.
21	Laborde-Boutet et al. (2009)	3D, unsteady, Euler/Euler by FLUENT, RANS approach for turbulence modelling, three k–ε model (Standard, RNG, Realisable), and three different modalities for gas-phase effects (Dispersed, Dispersed + Bubble Induced Turbulence, Per-Phase).
22	Andras et al. (2009)	Fluent (VOF model) and OpenFOAM.
23	Ekambara and Dhotre (2010)	3D, Euler-Euler approach, different turbulence models (k–ε, k–ε RNG, k–ω), Reynolds Stress Model (RSM) and Large Eddy Simulation (LES), and ANSYS-CFX.
24	Masood and Delgado (2014)	3D, Explicit Algebraic Reynolds Stress Model (EARSM), re-normalisation group (RNG), RNG bubble induced turbulence (BIT), k–ε models and CFD.
25	Masood et al. (2014)	Transient Euler-Euler, ANSYS CFX, Explicit Algebraic Reynolds Stress Model (EARSM), k–ε models and Baseline models (BSL).
26	Ali (2014)	Eulerian-Eulerian multifluid approach, standard k-ε turbulence model, unsteady state and COMSOL Multiphysics software.

Currently, there is no available simulation for this type of wet scrubber due to the complex flow (churn-turbulent) and the extremely complex design compared with a bubble column. As a starting point, simulation simple cases of wet scrubber flow can be achieved using ANSYS Fluent with several assumptions included.

2.6. Conclusion

Diesel engines release a range of harmful components into the environment in the form of gases, liquids and particulate matter. Wet scrubbers are used to clean diesel exhaust emissions for underground equipment by bubbling them through a liquid to reduce their temperature and remove some soluble components and particles. Then, these emissions pass through a dry filter to remove further diesel particulate matter. This chapter reviewed the particulate matter capturing mechanism, the heat transfer mechanism and the flow mechanism of the wet scrubber.

The performance of the wet scrubber depends on several parameters including the scrubber design and operating conditions. It is important to reduce the humidity of the outlet gas to prolong the life of the dry filter after the scrubber. This produces two benefits: increasing the operating time and reducing the maintenance cost. However, few studies have focused on this type of wet scrubber. Two of these studies (Situ et al. 2012; Hoque et al. 2014) investigated a limited range of operating conditions. One of these studies considered the transient heating process through the scrubber, and the other one analysed the scrubber experimentally.Therefore, it is fruitful to have an up-to-date and informative database about this device, especially for countries with mining sites or which have mining equipment production. This study considered the steady state heating process. It investigates the effect of more operating conditions, designing parameters and wide range of operating conditions on the scrubber performance. For example, the inlet gas temperature range from 20 $^{\circ}$C to 650 $^{\circ}$C.

Finally, wet scrubber performance can be investigated using experiments, thermodynamic analyses, heat transfer analyses and computational simulation. In this study 3 of these analyses combined to achieve the optimum performance of the wet scrubber: experiments, thermodynamic, heat transfer. The experiments analysed independently and their raw data used for further investigation in thermodynamic analysis and heat transfer analysis. Thesis aims achieved by combining the 3 analyses mentioned earlier such as reducing the gas relative humidity and the liquid at the scrubber exit.

Chapter 3 – Experimental Set-up and Methodologies

Chapter 2 explained and reviewed the possible methods that could be used to investigate the wet scrubber such as thermal analysis and heat transfer analysis. This chapter explores in detail the experimental set-up and the analysing methodology of the scrubber. It consists of three main sections: the exhaust wet scrubber, the experimental design and methodology, and the primary experimental results and discussions. The scrubber consists of the scrubber tank with gas supply system and measuring instruments, including thermocouples and a humidity probe.

The experiments include three sets of campaigns: transient heat loss estimation, steady-state heating and flow visualisation. The transient heat loss experiments are essential to obtain the heat loss from the scrubber. This heat loss estimation is hence used to analyse the scrubber thermodynamically through the steady-state heating experiments. This analysis obtains the theoretical outlet gas condition in the scrubber energy balance, in particular the relative humidity. Then, an optimum operating condition for the scrubber is suggested partially based on these results. The flow visualisation experiments directly investigate the bubbles dynamically and thermally. The third section of this chapter shows and discusses the experiments' observations and some relationships between the experiments controlled and the measured parameters. Finally, this chapter provides the necessary data for further investigations of the scrubber explained in detail in Chapters 4 and 5.

3.1. The Exhaust Wet Scrubber

The experiments were conducted with a laboratory apparatus (Figure 3-1). This apparatus was made based on the design of ANDERSON GROUP OF COMPANIES that located in Australia with scale 1:1. The laboratory apparatus consists of a scrubber tank, a gas-phase supply, an industrial air blower, a high-speed video camera system and other instruments such as thermocouples and a humidity probe.

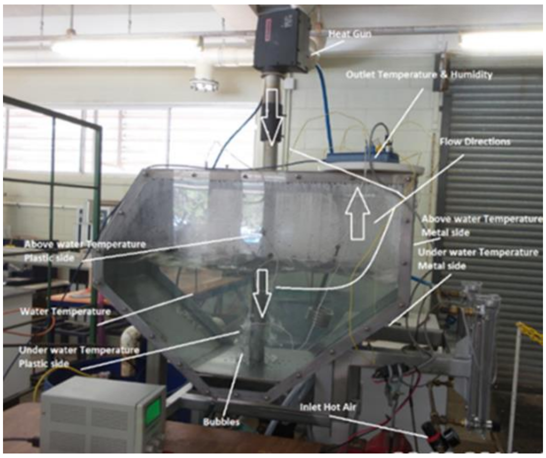

Figure (3-1). The laboratory apparatuses.

The scrubber tank main dimensions are 94.5cm×65cm×47cm (Figure 3-2). It is made of two materials. Most of the structure including the orifice plates is stainless steel. The stainless steel avoids possible erosion due to reaction with liquid and gas. The remaining front and back tank sides are made of transparent high-temperature resistant polycarbonate. This simply provides a clear view to monitor and film the bubbles using a high-speed camera.

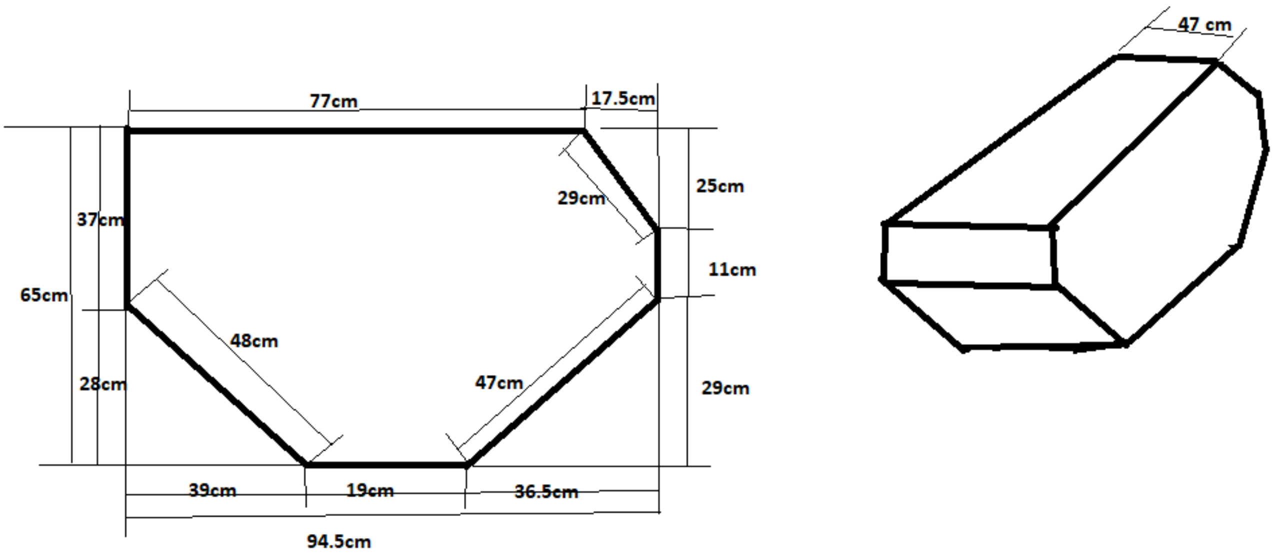

Figure (3-2). The laboratory apparatus dimensions.

An inlet gas vertical pipe is located at the scrubber centre. This pipe supplies gas to the tank nearly at its bottom. A horizontal plate with a number of orifices was installed above the pipe outlet. The purposes of using this orifice plate are to break the gas-phase stream into small bubbles (since this might increase the heat transfer) and to simplify monitoring the bubbles for the heat transfer investigation. Three orifice plates were used in the experiments in addition to the inlet pipe without any orifice plate (Figures 3-3 and 3-4). The three orifice plates have different orifice sizes: 5mm, 7.5mm or 10mm, with a number of orifices 100mm, 44mm or 32mm, respectively. The number of these orifices was selected because the total orifice area must be equal to the cross-sectional area of the inlet gas pipe to avoid increasing the flow back pressure.

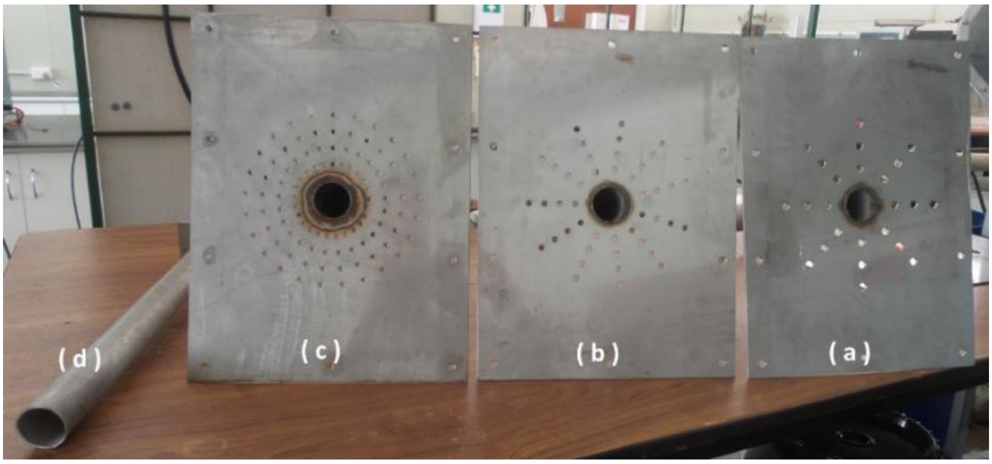

Figure (3-3). Different orifice plates (a) 10 (b) 7.5 (c) 5mm and (d) the inlet pipe without a plate.

In the flow visualisation experiments, in order to simplify monitoring and filming the bubbles, most orifices were blocked except one row (Figure 3-4). The remaining row consists of four orifices of 7.5mm or 5mm (Figure 3-4, b & c), or three orifices of 10mm (Figure 3-4, a). This blockage would increase the flow back pressure causing a slight scrubber vibration and bubbles departing from the orifice like a pulse.

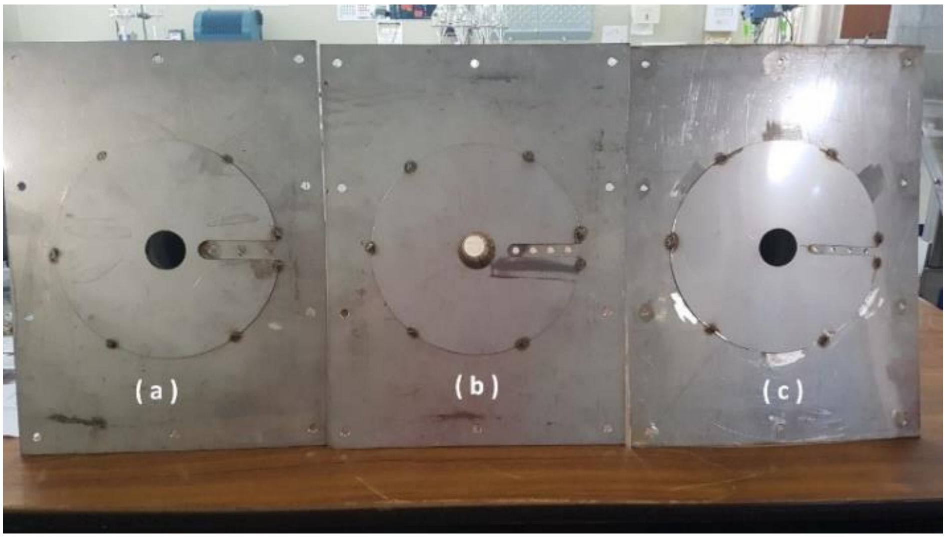

Figure (3-4). One row of orifices for the flow visualisation experiments.

The front and back polycarbonate sides of the scrubber tank are combined firmly with the scrubber frame, using bolts and a silicone gasket to prevent any liquid leakage. A drain is attached to the bottom scrubber surface to flush the liquid for different purposes such as scrubber cleaning and liquid volume adjusting. Some properties of these materials used to investigate the scrubber thermally are illustrated (Table 3-1).

Table (3-1). Apparatus materials specifications.

Part Name	Material	Thickness (mm)	Density (Kg/m^3)	Specific heat (kJ/kg)	Thermal conductivity (W/m.K)
Scrubber tank (except the front and back sides) and orifice plates.	316 stainless steel	3	8,030	502	14
Front and back tank sides.	Transparent high-temperature resistant polycarbonate	8	1,300	1,100	0.22
Inlet gas pipe of 49mm inner diameter.		2	8,030	502	14

3.1.1. Gas supply system

The gas was controlled before entering the system to provide different study cases. Air was supplied as a gas-phase from a laboratory compressor. Then, it passed through a water trap to remove any possible condensate water carried by the gas (Figure 3-5). A water trap is an essential component, to prevent damaging the downstream *Leister hotwind premium* blower that is mentioned later in this section.

The inlet gas flow rate is measured and controlled using *Dwyer* flow meters (Figure 3-5). They were placed in a parallel arrangement. These two direct-reading flow meters are compatible for both gas and liquid at any temperature below 54°C and pressure below 6.9bar. These two flow meters have different capacities, 10 and 30 Standard Cubic Feet per Minute (SCFM). Therefore, they are suitable for all the aimed inlet gas flow rates and together can measure the inlet gas flow rate from 0.0 to 850 Standard Litre Per Minute (SLPM). The measurement accuracy for the one of capacity 283 SLPM (10 SCFM) is ±5.6 SLPM, and it is ±56 SLPM for the other flow meter of 850 SLPM (30 SCFM).

Figure (3-5). The inlet gas flow meters and the water trap.

The inlet gas is passed through the *Leister hotwind premium* blower (Figure 3-6). This air blower is one of the *Leister products (HOTWIND PREMIUM)* with power consumption 5.4kW at 400V. The inlet gas volumetric flow rate can be set from 200 to 900 SLPM (at 20°C) and the inlet gas temperature can be raised to 650°C via the potentiometers on the blower side. This blower has a liquid crystal display screen to display both settings and actual temperature values. The blower was attached to the inlet gas pipe and received the gas from the air compressor via an adjacent rubber tube.

Figure (3-6). *Leister hotwind premium* air blower.

3.1.2. Instrumentation

For all experiments, several highly developed instruments were used to collect and/or record the experimental data and to minimise measurement error.

3.1.2.1. Relative humidity instrument

One of the most focussed aims of optimising scrubber performance is to reduce the humidity at the scrubber exit (Chapter 2). The Relative Humidity (RH) is effectively measured at various locations using a *Thermoworks* humidity probe (Figure 3-7). This high accuracy model (TW-USB-2) measures temperature, relative humidity, and dew point within the limits -35ºC to +80°C and 0-100% RH. The accuracy of this probe is ±0.3°C and ±2% RH at the relative humidity range from 20% to 80%, and ±1.5°C and ±4% RH for the relative humidity 80-100%. This probe operates independently and it can be connected directly to a laptop via a universal serial bus (USB) storing up to 16,382 measured readings. Moreover, the humidity probe contains a LED alarm indicator to indicate any possible hazard condition during the measurements and/or before downloading the data. To confirm the accuracy, this probe was calibrated before starting the tests to minimise error. An alarm was set up before each test to provide a clear indicator for any temperature and/or relative humidity excess and/or less than the set-up ones.

Figure (3-7). The humidity probe.

3.1.2.2. Temperature instrumentation

All temperatures were measured using thermocouples placed at different locations (Figure 3-8). These thermocouples were placed at the scrubber outlet, the mid-height below the liquid surface for both the transparent high-temperature resistant polycarbonate and the stainless steel sides, the mid-height above the liquid surface for both the transparent high-temperature resistant polycarbonate and the stainless steel sides, and two within the liquid. These thermocouples connected to a *Picolog* data logger and then to the laptop using the USB cable. It did not require any external power supply. This data logger has eight channels designed to measure and record any temperature from -270°C to 1,820°C, in high resolution and accuracy ±0.5°C.

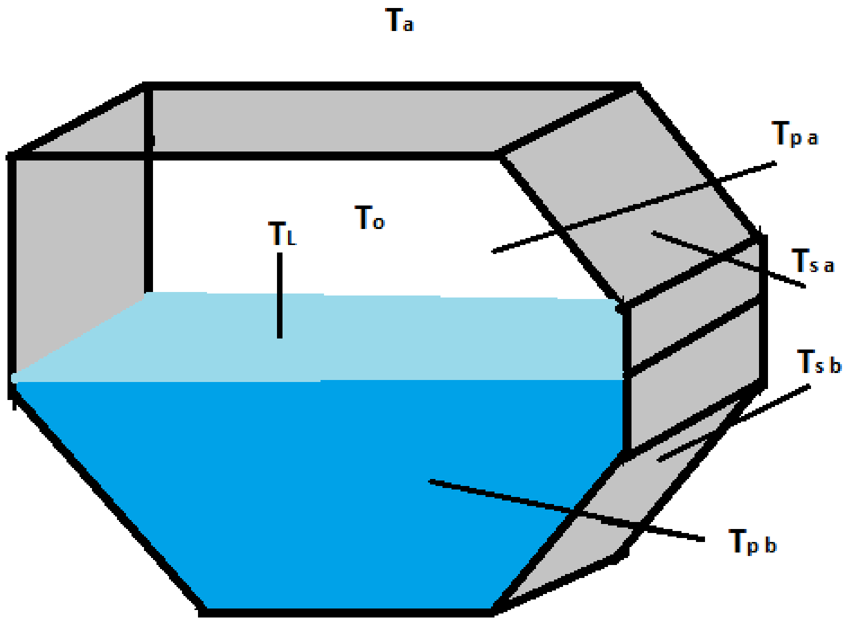

Figure (3-8). Thermocouple locations.

3.1.2.3. Pressure gauge

The inlet gas pressure can be read directly from a pressure gauge. This gauge was assembled with a control valve and a water trap. The importance of this assembly is to monitor and control the inlet gas pressure to avoid damaging any of the scrubber components. The pressure gauge has two scales: in bar, with a maximum reading of 10 bar at the accuracy of 0.2 bar, and in psi, with a maximum reading of 140psi at the accuracy of 2psi.

3.1.2.4. Scrubbing liquid heater

Rising the liquid temperature is essential to estimate the heat loss from the scrubber in heat loss estimation experiments. However, this process consumes a long period of time, especially, in the need to run several tests continuously. Therefore, a *SEI IMMERSION* heating element was used to reduce the required time to warm up the liquid. This portable heating element is a heating coil of 2.4kW at 240V and its coil is made of 75mm diameter high-quality stainless steel.

3.1.3. Flow visualisation system

The flow visualisation experiments were performed to capture the bubble size, shape and distribution. To clarify, both photos and movies were filmed using a *Photron FASTCAM Viewer* high-speed camera (Model UX100, 1,280x1,024 pixels at 4,000fps, 12-bit monochrome, 36-bit colour) as shown in Figure (3-9). This camera aligned horizontally to visualise the flow and it was operated at 1,000 frames per second (fps). The *Photron FASTCAM* connected to the laptop via an Ethernet cord.

A Light-Emitting Diode (LED) light was set up behind the high-speed camera and angled towards the transparent high-temperature resistant polycarbonate side. Further, high-quality bubble images and videos were achieved by connecting the camera with a *Nikon* 105 Lens in addition to placing a white background behind the back side of the scrubber.

Figure (3-9). The high-speed camera for the flow visualisation experiments.

3.2. Experimental Design and Methodology

3.2.1. Liquid and gas phases

Filtered air from the air compressor at an average of $23^{\circ}C$ and 13.5% RH was pumped into the test section from 115 to 285 SLPM. This air was chosen as an inlet gas for several reasons: availability, fitting with the thermodynamic standard properties, avoiding hazardous gases and eliminating any chemical reaction with the liquid and the scrubber.

The system was cleaned before running the experiments to remove contaminant. Then, fresh distilled water was added as the scrubbing liquid. The purpose of using the fresh distilled water was to eliminate any reaction that could occur with the inlet gas and to idealise the liquid to fit the thermodynamic standard properties tables. Different liquid volume ratios (LVR) (the ratio of the liquid volume to the total scrubber volume) 16-48% were investigated.

3.2.2. The experiments

Three major types of experiments investigated the wet scrubber. The first group of tests was steady-state heating experiments. This group investigated the energy balance of the whole scrubber based on the steady-state assumption. This analysis considers the heat loss from the scrubber body as one of several dependant parameters. Transient cooling estimation experiments were performed to obtain this heat loss. The third experiments observed the bubble and how it can be affected by the surrounding liquid, such as size, motion and heat transfer. The results of these experiments are used in the upcoming chapters for further analyses.

In this study, choosing the operating conditions are very important. For example, the inlet gas temperatures start from $20\ ^{\circ}C$ to $650\ ^{\circ}C$, and the inlet gas flow rates start from 4 SCFM to 10 SCFM. However, the mining equipment have different capacities such as one of CATERPILLAR engines produces exhaust gas at $539\ ^{\circ}C$ and 1,851 SCFM. This means that this study already covered the inlet gas temperature effect. The inlet gas flow rates were much less that the reality. However, the heat transfer analysis of the scrubber can be achieved only at low inlet gas flow rates because of the liquid turbulence. Therefore, this disagreement in simulating the flow rate is considered as a study strength.

3.2.2.1. Steady-state heating experiments

The steady-state heating tests consisted of supplying hot air at a specific mass flow rate and temperature, for a chosen liquid volume ratio and orifice size (Figure 3-10). These experiments started by supplying the gas at a certain temperature (for example $150^{\circ}C$) into the scrubber until it reached a steady-state condition based on the liquid temperature. This steady-state condition was considered when the rising of liquid temperature had a negligible value with time. For example, temperature changes should be less than 1°C over 10 minutes. Temperatures at different points were measured as mentioned earlier (*3.1.3.2. The temperature instrumentation*). The inlet gas temperature was recorded directly from the digital display of the hot air blower. The relative humidity was measured at the scrubber outlet, the inlet gas and the scrubber surrounding. All data of both temperature and relative humidity was downloaded at the end of each test through two specialist software applications. The inlet gas flow rate was read directly from the *Dwyer* flow meters. Also, to check the evaporation rate, the liquid level inside the scrubber was recorded before and after each test.

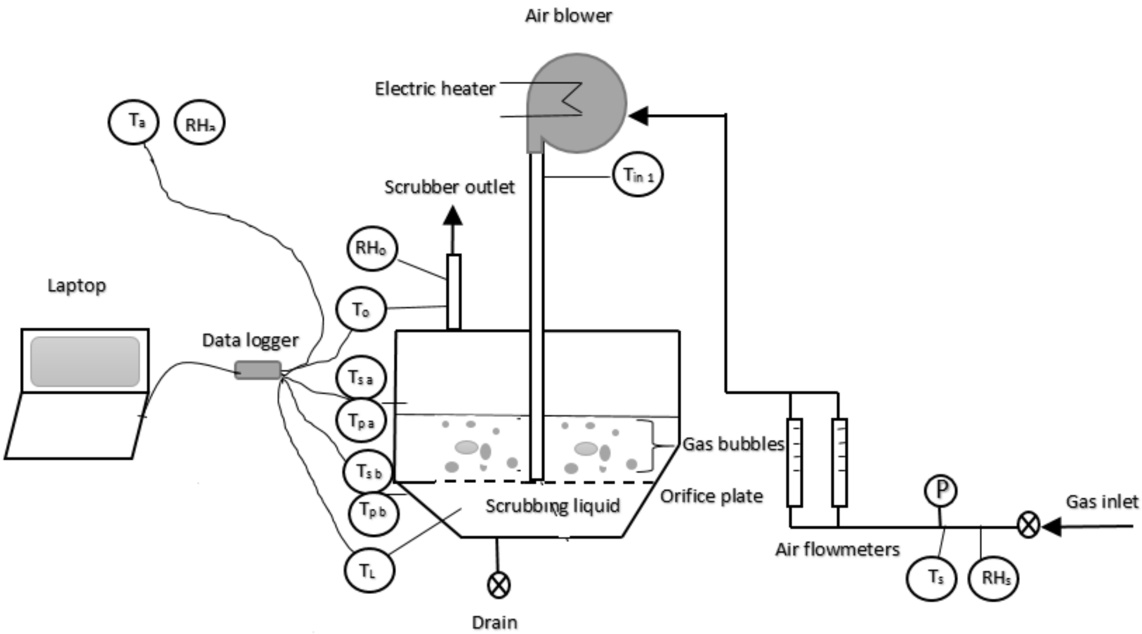

Figure (3-10). The schematic diagram for the apparatus set up for the steady-state experiments.

To change to another operating condition, the inlet gas temperature was increased (for example to 250°C) at the same gas flow rate as the previous test. To run another test, the inlet gas temperature was increased again, and the same steps mentioned earlier in this section were repeated for 350 °C, 450 °C, 550 °C and 650°C. After that, the inlet gas flow rate was increased via the flow meters valves to achieve the next test condition. The same steps were repeated again here for all of the gas flow rates of 115, 170, 225 and 285 SLPM and other new measurements were recorded. This procedure was continued until the inlet gas flow rate reached the gas source capacity at 285 SLPM.

The orifice plate was changed to study the effect of the orifice size on the measured data, and all the previous steps were repeated here. Finally, the effect of liquid volume ratio on the investigating parameters was tested for one condition only (without the orifice plate). In conclusion, these experiments investigated the inlet gas temperature and flow rate effect on the outlet gas condition of the scrubber. The 115 steady-state heating experiments conditions are shown in Table (3-2).

Table (3-2). The experimental conditions of the steady-state heating experiment.

Test series number	**Test series symbol**	**Inlet gas-phase flow rate (SLPM)**	**Inlet gas-phase temperature (T_{in1}) (°C)**	**Liquid volume ratio (%)**	**Orifice size (mm)**
1	□	115	150, 250, 350, 450, 550, 650	20	N/A
2	◇	170	150, 250, 350, 450, 550, 650	20	N/A
3	○	225	150, 250, 350, 450, 550, 650	19	N/A
4	△	285	150, 250, 350, 450, 550	16	N/A
5	□	115	150, 250, 350, 450, 550, 650	48	N/A
6	◇	170	150, 250, 350, 450, 550, 650	42	N/A
7	○	225	150, 250, 350, 450, 550, 650	46	N/A
8	△	285	150, 250, 350, 450, 550	45	N/A
9	□	115	150, 250, 350, 450, 550, 650	38	5
10	◇	170	150, 250, 350, 450, 550, 650	37	5
11	○	225	150, 250, 350, 450, 550, 650	36	5
12	△	285	150, 250, 350, 450, 550	36	5
13	□	115	150, 250, 350, 450, 550, 650	38	7.5
14	◇	170	150, 250, 350, 450, 550, 650	38	7.5
15	○	225	150, 250, 350, 450, 550, 650	38	7.5
16	△	285	150, 250, 350, 450, 550	38	7.5
17	□	115	150, 250, 350, 450, 550, 650	42	10
18	◇	170	150, 250, 350, 450, 550, 650	42	10
19	○	225	150, 250, 350, 450, 550, 650	42	10
20	△	285	150, 250, 350, 450, 550	42	10

3.2.2.2. The transient heat loss estimation experiments

Heat loss from scrubber should be considered to analyse the scrubber thermodynamically, based on the first law of thermodynamics. Different approaches can be used to achieve this purpose and they are discussed in detail in the next chapter. Two of these approaches depend on separate experiments to estimate the heat loss. Heat loss experiments consist of warming up the liquid to 80°C without supplying the gas using the portable heating element. The 80°C temperature was selected below boiling temperature to avoid liquid evaporation and to provide an acceptable temperature difference between the liquid and the ambient. The liquid was kept at this temperature for a specific time then let cool down. This procedure was repeated for several times for initial liquid temperatures 75 °C, 70 °C, 65 °C and 60°C respectively. The ambient temperature (T_a) nearly was constant at 29°C during these tests.

After that, the recorded temperature data were processed using the exponential smoothing method to remove the noise in the original signals (Table 3-3). This exponential smoothing method uses a time series to generate a forecast with lesser weights given to the observations further back in time. These curves were analysed directly after a certain period of shutting down the heating element. This period of time represents the transient energy loss. It differs for each investigated scrubber and fluid components that mentioned in Table (3-3). For example, the start point for cooling of the liquid temperature curve is different from the above liquid level steel side temperature curve. The temperature drop rate was obtained using all five warming and cooling experiments mentioned earlier in this section. More detail will be explained in the next chapter in addition to introducing other methods to estimate the energy loss through scrubber sides.

Table (3-3). The initial temperatures of the transient heat loss estimation experiments (°C).

Test No.	**1**	**2**	**3**	**4**	**5**
Liquid (T_l)	80	75	70	65	60
Below the liquid surface of the stainless-steel side (T_{sb})	77.7	72.5	68.3	63.3	59.1
Above the liquid surface of the stainless-steel side (T_{sa})	69.9	64	61.6	55	55.1
Below the liquid surface of the transparent high-temperature resistant polycarbonate side (T_{pb})	59.9	56.7	55.4	50.9	47.1
Above the liquid surface of the transparent high-temperature resistant polycarbonate side (T_{pa})	45.6	43.2	42.7	39	38.5

3.2.2.3. Flow visualisation experiments

These tests investigated the effect of the inlet gas temperature, the orifice size and the inlet gas flow rate on scrubber performance using the experimental set up (Figure 3-11). There are three main differences between these experiments and the steady-state heating ones. Firstly, it depends on using a flow visualisation system (a high-speed camera) to record both videos and images. Then these images and videos were analysed to investigate the flow characterisation.

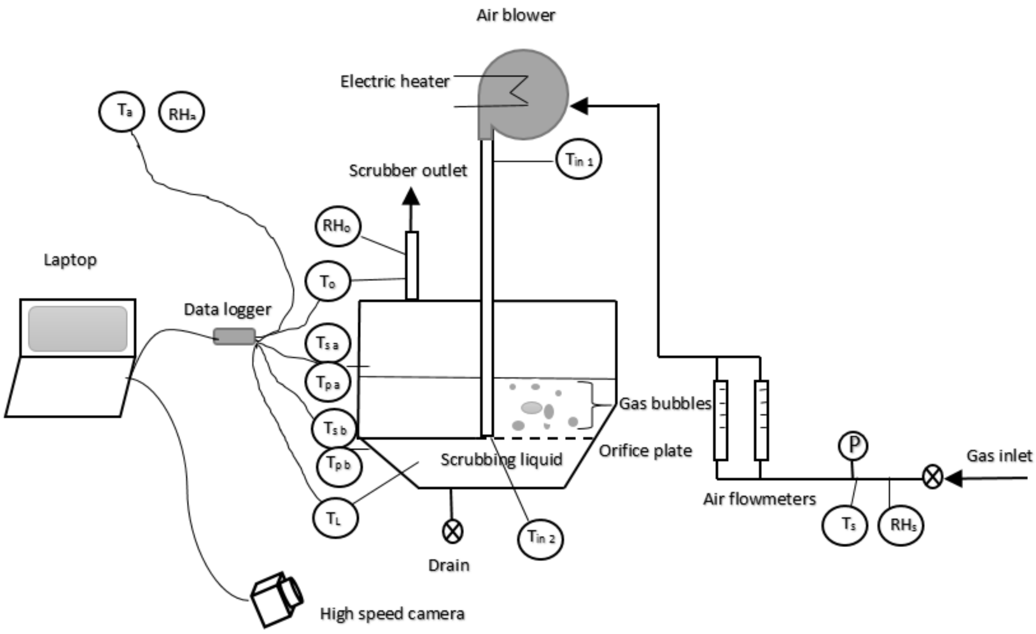

Figure (3-11). The schematic diagram for the flow visualisation experiment.

The second difference is essential to improving the visualisation system by blocking all orifices except one row as explained and shown earlier (Figure 3-4). It is scarcely complex to monitor the bubble motion and size without blocking these orifices because of bubbles overlapping (Figure 3-12).

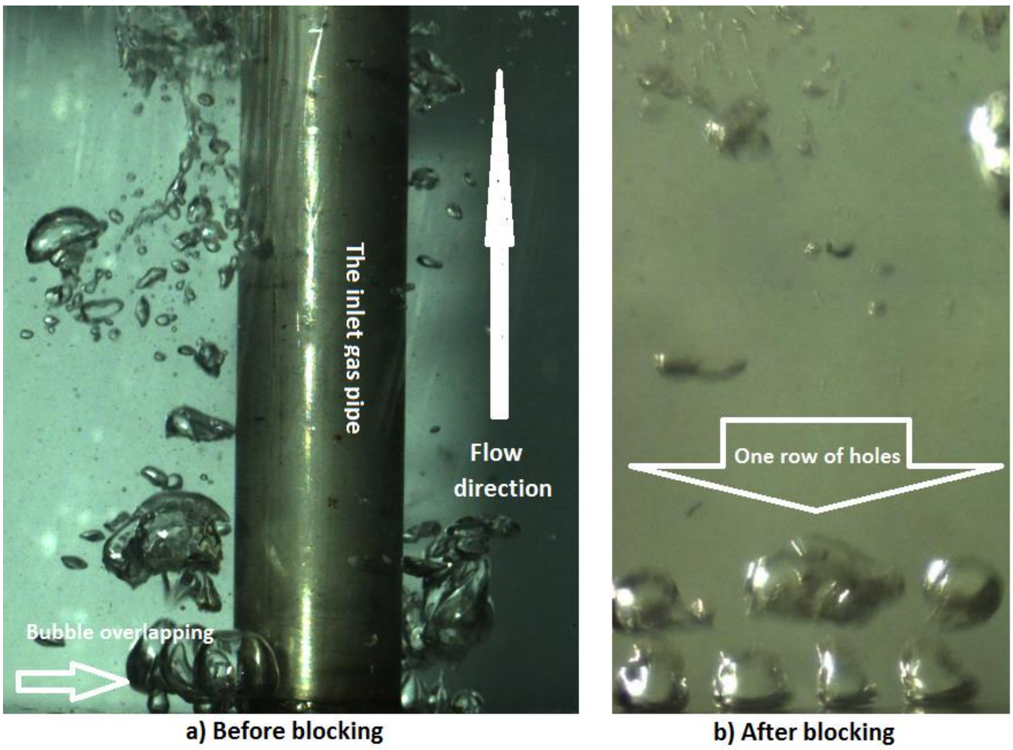

Figure (3-12). The purpose of blocking several orifices.

The third difference is related to the inlet gas temperature consideration. The thermocouple was placed near the outlet of the inlet gas pipe (Figure 3-13) instead of considering the temperature measurement after the heat gun directly. Further, the gas temperature reduces by passing through the inlet gas pipe as a result of the forced convection at the outside wall of the inlet gas pipe due to high temperature differences. The majority of this convection heat loss was with the liquid and the minority with the gas above the liquid surface. The liquid has higher thermal capacity than the gas. The temperature difference between the two ends of the inlet pipe affects the bubble temperature in several ways, such as the selection of the thermal properties.

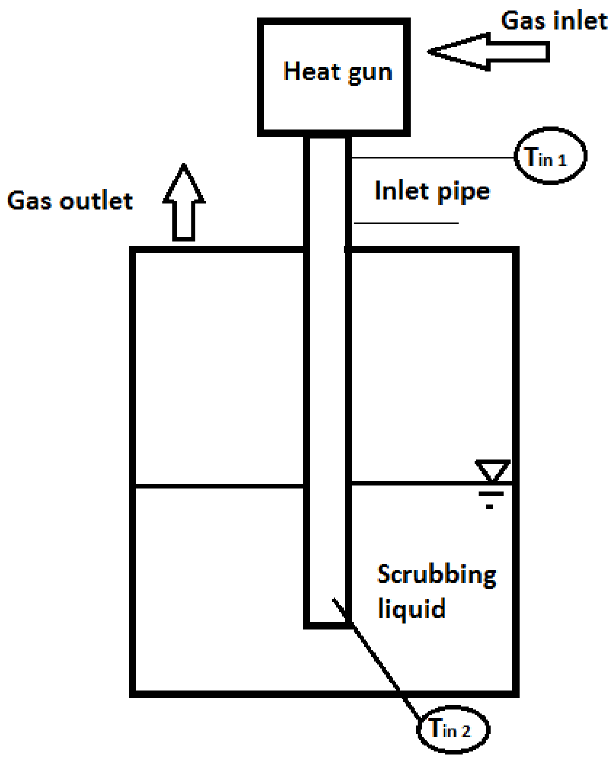

Figure (3-13). Inlet gas temperature measurement for flow visualisation experiment.

The flow visualisation experimental conditions consisted of 16 tests (Table 3-4). Both liquid volume ratio and the liquid temperature were maintained constant at 42% and 20°C respectively to eliminate their possible effects on the wet scrubber performance. Monitoring bubbles became simpler and more accurate using the orifice plate. Therefore, the three size orifices were tested to find their possible effect of this size on the bubble formation. However, this study did not include the case of the inlet pipe without any orifice plate, due to the complexity of monitoring the bubbles as a result of turbulence as explained earlier (Figure 3-12).

Table (3-4). Flow visualisation experimental conditions.

Test number	Inlet gas flow rate (SLPM)	Inlet gas temperature (T_{in1}) ($^{\circ}C$)	Orifice size (mm)
1	115	20,100, 300,500, 650	5
2	170	20	5
3	225	20	5
4	285	20	5
5	115	20	7.5
6	170	20	7.5
7	225	20	7.5
8	285	20	7.5
9	115	20	10
10	170	20	10
11	225	20	10
12	285	20	10

3.3. Primary Experimental Results and Discussions

Three types of tests were conducted separately to investigate the scrubber. These experiments were the transient heat loss estimation, the steady-state heating and the flow visualisation. The first two experiments were used to study the scrubber thermodynamically, while the flow visualisation experiments were used for the heat transfer investigation. Some observations in the steady-state heating experiments and flow visualisation experiments were specified for the inlet gas flow rate or orifice size or inlet gas temperature and they are discussed in detail in the following sections.

3.3.1. Steady-state heating experiments

The observed effect of the controlled parameters on the measurements are explained in depth in this section.

3.3.1.1. Inlet gas flow rate effect

The inlet gas flow rate has a major effect on scrubber performance. The gas enters the scrubber from the inlet pipe and leaves this pipe from below the liquid surface, causing turbulence. The degree of the flow turbulence depends mainly on the inlet gas flow rate. The gas bubbles move upward, overlap, break up and/or coalesce then burst and/or move down near the scrubber surfaces based on the turbulence degree. Bubbles move adjacent to the inlet gas pipe with high overlapping percentages in cases of orifice plate absence. Indeed, this turbulence depends slightly on the orifice size. Moreover, the bubbles depart differently from the orifices, from one plate to another, and from one gas flow rate to another. For example, bubbles departed from the inner row of orifices more than from the outer ones (Figure 3-14).

Figure (3-14). More bubbles departing from inner orifices than the outer ones.

Turbulence causes liquid ejection from the scrubber, especially for the high liquid volume ratio and high inlet gas flow rate, which agrees with Hoque et al. (2014). It is noticeable that the orifice plate reduces the turbulence and liquid ejection in addition to distributing bubbles uniformly.

3.3.1.2. Inlet gas temperature effect

The inlet gas temperature has another major effect on scrubber performance. Increasing the inlet gas temperature increases the liquid temperature (Table 3-5). This table shows the effect of increasing the inlet gas temperature on the liquid temperature and of both the outlet gas relative humidity and temperature at 170 SLPM, liquid volume ratio 42% and 10mm orifice size. The inlet gas temperature increment increases energy received by the liquid, despite the liquid volume ratio or the orifice size, as a result of increasing the inlet energy. Also, increasing the inlet gas flow rate reduces the time required to reach the steady-state condition. Further data for all other experiments are available in Appendix A.

Table (3-5). The effect of the inlet gas temperature on both the liquid and the outlet gas conditions.

Inlet gas temperature (T_{in1}) (ºC)	Liquid temperature (T_l) (ºC)	Outlet gas temperature (T_o) (ºC)	RH_o (%)
150	42.2	41.2	74
250	42.3	41.3	96
350	42.4	41.5	94
450	42.9	41.8	96
550	43.4	42.2	96

650	44.5	43.4	96

The outlet gas temperature increased with increasing the inlet gas temperature due to more energy input to the system, despite liquid volume ratio or orifice size. This is due to the energy leaving the scrubber at a higher rate for the higher inlet gas flow rate and/or temperature. This type of scrubber effectively reduces the gas temperature from 650°C to about 50°C (Figure 3-15). This could be a result of losing the energy from the liquid to the ambient due to high-temperature difference. Analysing the scrubber thermodynamically in the next chapter explains more about the outlet gas conditions.

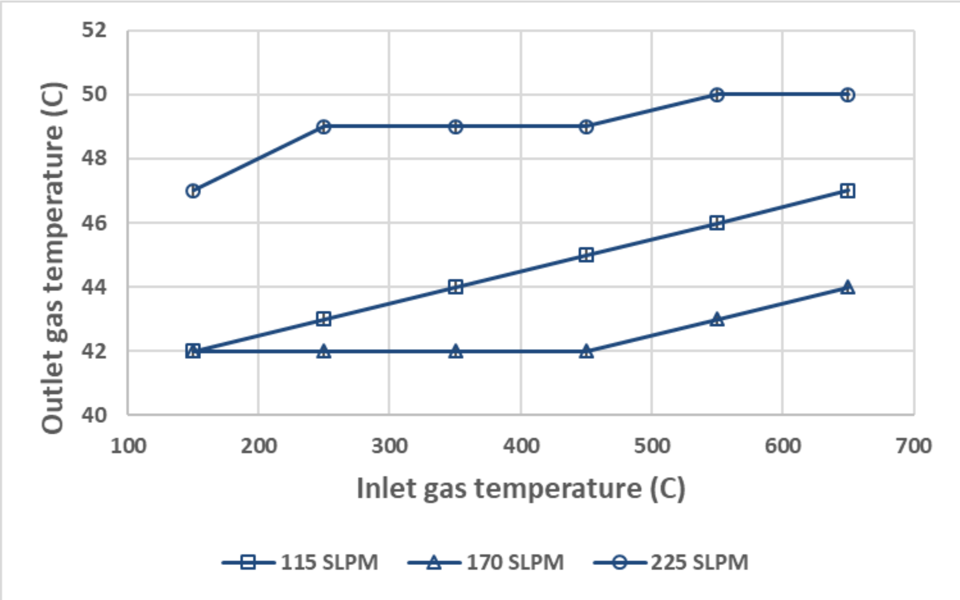

Figure (3-15). The relationship between the inlet and outlet gas temperatures.

The gas mostly leaves the scrubber in a saturation condition due to the high rate of evaporation (Figure 3-16). The outlet gas relative humidity for most experiments was between 96-98%. If the error of the humidity probe is taken into account, the relative humidity can be considered as 100%. However, the outlet gas relative humidity was observed as less than saturation in a few tests of the inlet gas temperature at 150°C. This is because this temperature was not enough to evaporate more liquid based on the inlet gas flow rate. The next chapter investigates this relationship and it compares these results with the theoretical one obtained from the energy balance. The liquid temperature and both the temperature and relative humidity of the outlet gas were independent of the orifice size and the liquid volume ratio. Indeed, using less liquid and/or an orifice plate reduced the time required to reach the steady-state condition due to better mixing.

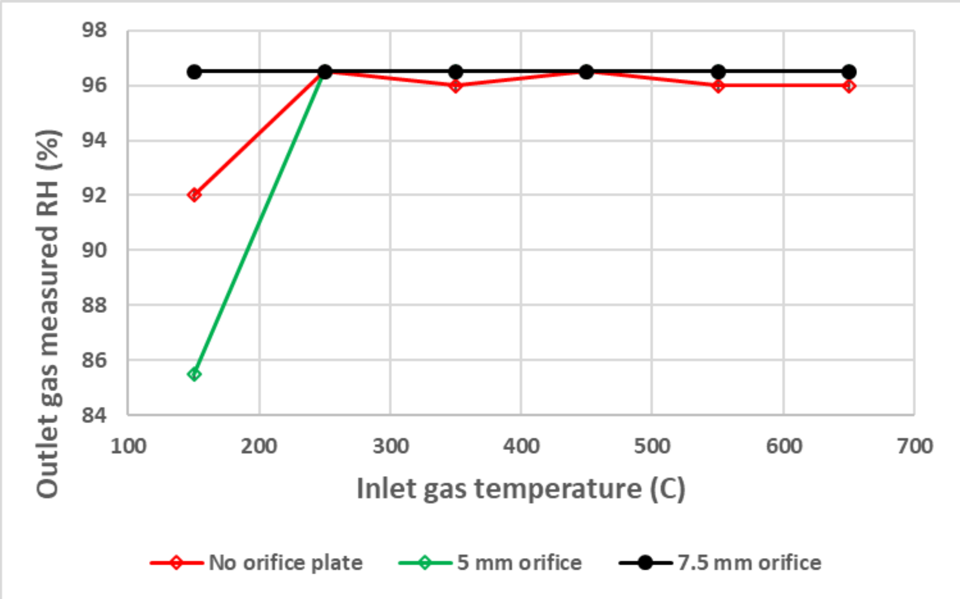

Figure (3-16). The relationship between the inlet gas temperature and the outlet gas relative humidity.

3.3.2. Flow visualisation experiments

Although these experiments mostly followed the same procedure as the steady-state heating process, there were some primary observations made during these experiments.

3.3.2.1. Gas temperature drop through the inlet pipe

The inlet hot gas passed through the inlet gas pipe and lost some of its heat through the pipe wall as a result of forced convection from the pipe outside. Therefore, its temperature was reduced (Figure 3-17). This explains the need to place a thermocouple near the exit of the inlet gas pipe because this was considered as the initial bubble temperature in the heat transfer calculations in Chapter 5. The relationship between the temperatures at the inlet pipe ends used to calculate the bubble temperature exactly at the orifice can be expressed as:

$$T_{in2} = 0.8\,T_{in1} + 19.8, \tag{3-1}$$

where: T_{in2} is the bubble temperature at the inlet pipe exit ($^{\circ}$C) and T_{in1} is the inlet gas temperature directly after the air blower ($^{\circ}$C).

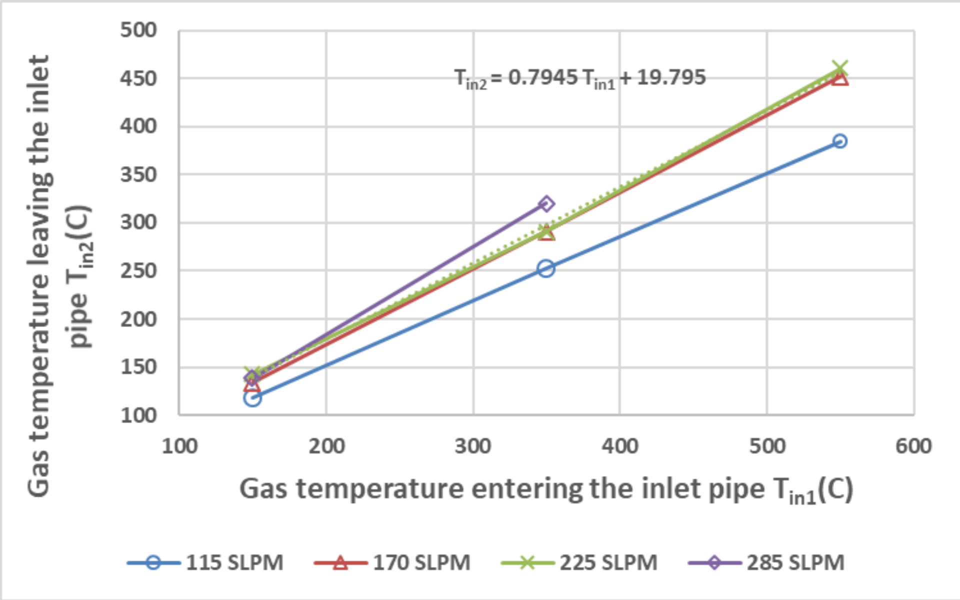

Figure (3-17). Inlet gas temperature reduction across the inlet gas pipe.

3.4.2.2. Flow regions

The turbulent flow is the most complex and highly unsteady flow of all flow types. In this scrubber, the bubbles' paths can be divided into three regions based on the inlet gas flow rate and/or temperature (Figure 3-18). The turbulence strongly affected the development of these regions. At high gas flow rates, the regions formation was very quick. Therefore, only one region (churn-turbulent) was recognised in the flow in this case. More details are included in Chapter 5.

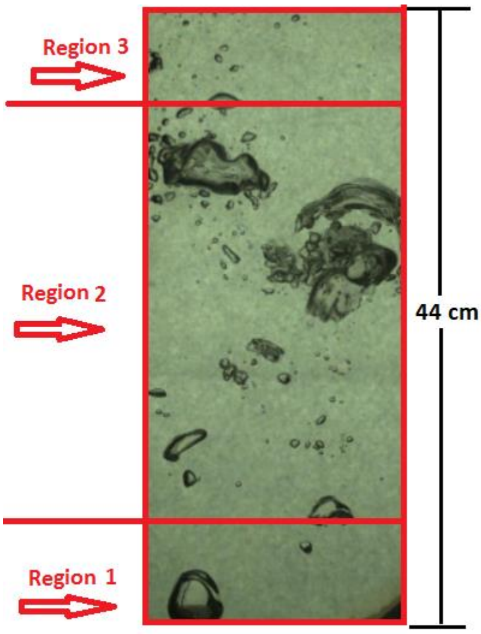

Figure (3-18). Observation of three flow regions in the scrubber.

3.4.2.2.1. Region one / departing region

The first region of the scrubber flow is located directly above the orifice and it contains clear recognition bubbles. These bubbles are defined as parent or mother bubbles and they moved upward. Their growth was fairly smooth for a low-inlet gas flow rate. At this flow rate, the maximum bubble size occurred after a short time directly above the orifice. This maximum bubble size also depended on the orifice size. For example, the large orifice produces larger bubbles than the smaller orifice. Each bubble travels separately from others without breaking or overlapping. This region was limited vertically from the orifice until the next region and this depends on the inlet gas flow rate. For example, it was observed to be about one-quarter of the liquid height at 115 SLPM inlet gas flow rate. This region was independent of the liquid volume ratio and the inlet gas temperature.

3.4.2.2.2. Region two / churn-turbulent region

The second region was located downstream and upward from the previous one directly. It contains both big bubbles due to coalescence and small bubbles as a result of bubble breakup. Also, there is a possibility of some bubbles from the departing region. These bubbles were in continuous change of their shape and size. A high percentage of bubbles overlapping was observed in this region. Most important, the flow turbulence leads bubbles' number, shape, size and movement direction in this region. This is a good agreement with Clift et al. (1978) who noted that in a multiphase flow equipment, the bubbles' size distribution is led by the breakup and coalescence dynamics. These bubbles move upward towards the liquid surface or/and towards the interior scrubber surfaces based on flow turbulence. At higher inlet gas flow rate, the travelling time of the bubbles from the orifice to the liquid surface is very short (Figure 3-19). This region is independent of orifice size. However, it was strongly affected by the inlet gas flow rate and the liquid volume. For example, the flow turbulence changes the liquid state of low volume easier than the high one. This region was slightly affected by the inlet gas temperature as a result of increasing the bubble velocity as explained (see Chapter 5).

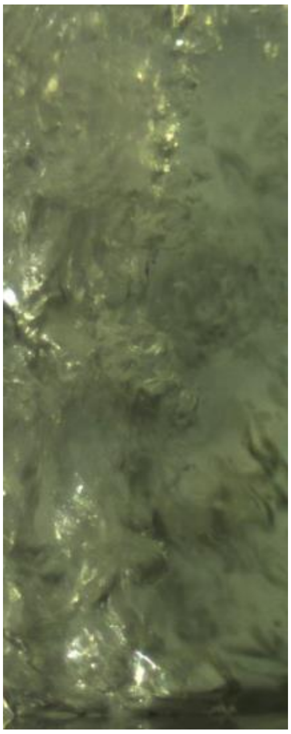

Figure (3-19). Two flow regions at high inlet gas flow rate.

3.4.2.2.3. Region three / bubbly region

The third region of the scrubber flow is located near the liquid surface, and the appearance of this region is also led by turbulence. It contains small bubbles that shaped after breaking up the bubbles of region two into smaller ones. These bubbles are defined as outlet (daughter) bubbles. Most of these bubbles burst at the liquid surface with temperature equals to the outlet gas temperature. However, some of these small bubbles moved downward at the interior scrubber surfaces following the effect of the flow turbulence. This region depends mainly on the flow turbulence, in particular region 2, as a result of the inlet gas flow rate. However, it was independent of the orifice size, the liquid volume and the inlet gas temperature.

3.4. Conclusion

The wet scrubber investigated experimentally including several controlled parameters such as inlet gas flow rate, inlet gas temperature and liquid volume ratio. The investigation includes some designing parameters such as orifice size. The experimental results confirmed that the scrubber effectively reduces the inlet gas temperature from 650°C to about 50°C based on equation. However, the outlet gas relative humidity increased due to the high liquid evaporation rate. Adding the orifice plate reduces the turbulence and the liquid leaving the scrubber from the outlet.

Three flow regions were observed at the low inlet gas flow rate: departing, churn-turbulent and bubbly. The most complex region is the churn-turbulent one because it contains all bubble overlapping, breaking and/or coalescing. The departing region has nearly the same height as the bubbly one. This height equals about one-quarter of the total liquid height. About a half of the liquid height was observed for the churn-turbulent region. However, only the churn-turbulent region was observed at a high inlet gas flow rate from the orifice to the liquid surface. Further, the bubbles' distribution was not uniform for all orifices. Indeed, more bubbles departed the inner orifices ring than the outer ones.

The results of these experiments were used to analyse the whole scrubber thermodynamically in Chapter 4, in addition to analysing the scrubber using the heat transfer analysis of bubbles in Chapter 5. The thermal analysis of the scrubber based on the steady-state heating experiments in the next chapter depends on the heat transfer estimation experiments. The bubble heat transfer and hydrodynamic analysis inside the scrubber achieved was based on the flow visualisation experiments. The dependence of the scrubber performance on which controlled parameter was recognised after completing these analyses in the next two chapters.

Chapter 4 – Thermodynamic Analysis of a Wet Scrubber

Wet scrubber performance can be analysed thermodynamically based on the first law of thermodynamics (Abdulwahid et al. 2018). In this chapter, the thermodynamic analysis of the scrubber was achieved depending on the experimental data obtained from Chapter 3, in particular, the steady-state heating experiments and the heat loss estimation experiments. This analysis assumed that the energy carried by the inlet gas can be balanced by both the energy terms at the scrubber outlet and the scrubber boundaries in the steady-state experiments. This steady-state assumption was used previously to evaluate the energy balance for the wet scrubber. This method has shown that the temperature increment at the scrubber outlet corresponds to the reduction in the outlet gas relative humidity (Situ et al. 2012). This approach was used also by Zizka et al. (2017) to investigate the bubble column. However, a transient-state assumption was used by Hoque et al. (2014) to test the wet scrubber thermodynamically. Hoque et al. (2014) observed that gas leaving the scrubber carried some liquid due to turbulence. This might damage the dry particulate filter and increase the production cost because of maintenance downtime and spare part costs.

This chapter consists mainly of three sections: the modelling design and methodology, the thermodynamic model results and their discussion and the outlet gas humidity calculations. The wet scrubber model set-up description is explained in detail in the first section of this chapter. This section includes the necessary assumptions that were used to analyse the scrubber. Then, the steady-state thermodynamic analysis section introduces the scrubber energy balance, the mass balance, the results and their discussion. The analysis section also includes the estimation of the heat loss from the scrubber, the comparison between several methods to estimate this heat loss, the convective heat transfer coefficient for the outer sides of the wet scrubber and the steady-state heating experiments. Finally, the outlet gas relative humidity calculations based on the energy and the mass balances of the scrubber are explained and compared with the measured ones in section three of this chapter. To conclude, this chapter aims to develop the thermodynamic model of the scrubber based on the steady-state assumption using the non-dimensional approach. As a result of that, wet scrubber performance can be optimised to prolong the dry particulate filter and to reduce the overall production cost.

4.1. Modelling Design and Methodology

The scrubber was investigated experimentally (Chapter 3) including 115 operating conditions for the steady-state heating tests. This chapter analyses the scrubber thermodynamically based on these data. All of these operating and measured parameters were converted into a non-dimensional form. The inlet gas flow rate was described using the inlet gas Reynolds number (Re) of range 1,200 to 3,300. This Reynolds number was calculated based on the inlet gas inner pipe diameter. The inlet gas temperature ratio (θ) equals the inlet gas temperature over to the ambient one (Equation 4-1). These two temperatures were chosen because both are independent of scrubber performance and they can be measured directly using the thermocouples. The inlet gas temperature ratio was tested for different values from 1.4 to 3.

$$\theta = \frac{T_{in1}}{T_a}, \tag{4-1}$$

where; θ is the inlet gas temperature ratio at the pipe inlet, T_{in1} is the inlet gas temperature after the heat blower (K) and T_a is the ambient temperature (K).

The next non-dimensional controlled parameter is the orifice ratio (β). It is the orifice diameter d_o in (mm) over the pipe diameter D in (mm) as shown in Equation (4-2). Each orifice plate has a number of orifices and their total areas equal the inlet gas pipe diameter (D) to avoid the back-pressure increment. Moreover, this chapter investigates several orifice ratios (β): N/A, 0.1, 0.15 and 0.2 as shown earlier in the past chapter particularly in Figure (3-3).

$$\beta = \frac{d_o}{D} \tag{4-2}$$

The liquid to gas ratio (L/G) is usually used in wet scrubber analysis. However, the Liquid Volume Ratio (LVR) was used here instead of the L/G because there is no liquid feeding in this type of scrubber. The LVR represents the scrubbing liquid volume over the total scrubber volume (Equation 4-3). This chapter investigates different LVR from 16 to 48% as explained in the previous chapter particularly in Table (3-2).

$$\mathrm{LVR} = \frac{V_l}{V_{sc}}, \tag{4-3}$$

where; V_L is the liquid volume (m^3) and V_s is the total scrubber tank volume (m^3).

The laboratory apparatus used in this investigation was explained in detail in Chapter 3 (Figures 3-1 and 3-10). The non-dimensional form of the inlet gas phase is represented by the inlet gas of Prandtl number range 0.698-0.726, and the liquid phase represented by Prandtl number 7.6, respectively. Table 4-1 explains the operating conditions in the non-dimensional form instead of the dimensional form (Table 3-2). For some tests, the liquid volume ratio was maintained constant to eliminate the possible effect of changing the liquid volume on thermodynamic analysis.

Table (4-1). The operating conditions in the non-dimensional forms.

Test number	Test symbol	Re	θ	LVR (%)	β
1	□	1,200	1.4, 1.7, 2, 2.4, 2.7, 3	20	N/A
2	◇	1,800	1.4, 1.7, 2, 2.4, 2.7, 3	20	N/A
3	○	2,400	1.4, 1.7, 2, 2.4, 2.7, 3	19	N/A
4	△	3,300	1.4, 1.7, 2, 2.4, 2.7	16	N/A
5	□	1,200	1.4, 1.7, 2, 2.4, 2.7, 3	48	N/A
6	◇	1,800	1.4, 1.7, 2, 2.4, 2.7, 3	42	N/A
7	○	2,400	1.4, 1.7, 2, 2.4, 2.7, 3	46	N/A
8	△	3,300	1.4, 1.7, 2, 2.4, 2.7	45	N/A
9	□	1,200	1.4, 1.7, 2, 2.4, 2.7, 3	38	0.1
10	◇	1,800	1.4, 1.7, 2, 2.4, 2.7, 3	37	0.1
11	○	2,400	1.4, 1.7, 2, 2.4, 2.7, 3	36	0.1
12	○	3,300	1.4, 1.7, 2, 2.4, 2.7	36	0.1
13	△	1,200	1.4, 1.7, 2, 2.4, 2.7, 3	38	0.15
14	□	1,800	1.4, 1.7, 2, 2.4, 2.7, 3	38	0.15
15	◇	2,400	1.4, 1.7, 2, 2.4, 2.7, 3	38	0.15
16	△	3,300	1.4, 1.7, 2, 2.4, 2.7	38	0.15
17	□	1,200	1.4, 1.7, 2, 2.4, 2.7, 3	42	0.2
18	◇	1,800	1.4, 1.7, 2, 2.4, 2.7, 3	42	0.2
19	○	2,400	1.4, 1.7, 2, 2.4, 2.7, 3	42	0.2
20	△	3,300	1.4, 1.7, 2, 2.4, 2.7	42	0.2

4.1.1. Assumptions

The thermodynamic investigation of the scrubber can be simplified by applying some assumptions. For instance, both the outlet gas and the inlet gas contain pure air and water vapour. The dry air consisted of 79% nitrogen and 21% oxygen based on volume. Furthermore, the inlet gas has a constant relative humidity of 13.5% and constant temperature of 23°C. This was calculated based on the average of two measurements at the flow meters before the industrial gas blower.

The conductive heat loss from the outer of the inlet pipe was neglected due to its insignificant surface area compared with the total scrubber surface area. However, the convective heat transfer coefficient between the scrubber and the ambient had a uniform and constant value for all scrubber sides. In fact, this coefficient depends on the surface orientation and roughness (Incropera and DeWitt 2002). It is important to neglect the slight amount of liquid carried occasionally by the outlet gas at higher inlet gas Reynolds number and higher liquid volume ratio. Therefore, there was no heat loss due to this term.

4.1.2. Steady-state energy and mass balances of the wet scrubber

The steady-state thermodynamic analysis of the scrubber consists of energy balance according to the first law of thermodynamics and the mass balance according to the continuity equation. The energy equation balances between the inlet and the outlet energies including the boundaries (Equation 4-4 and Figure 4-1):

$$\dot{E}_{in} = \dot{E}_{out} + \dot{E}_{\Delta v} + Q_L, \tag{4-4}$$

where: $\dot{E}_{in}$ is the inlet gas energy (kW), $\dot{E}_{out}$ is the outlet gas energy (kW), $\dot{E}_{\Delta v}$ is the energy lost due to liquid evaporation (kW) and Q_L is the heat loss from the scrubber to the surroundings through the scrubber sides (kW).

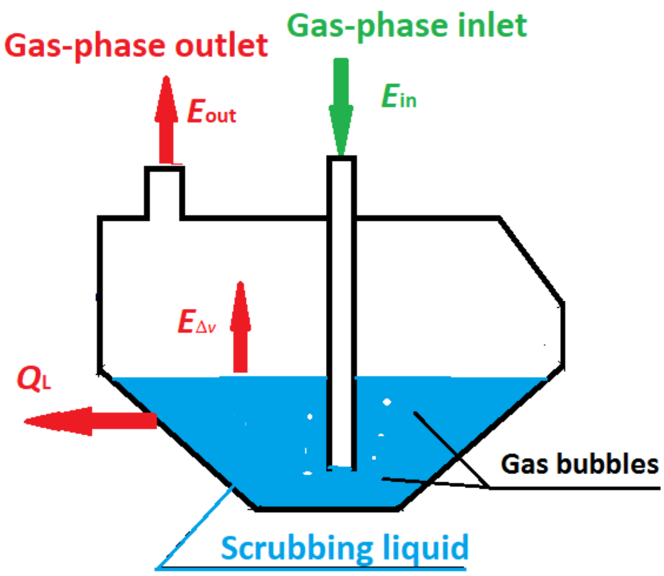

Figure (4-1). The scrubber energies.

The inlet and outlet energies were calculated based on the air components, which include oxygen (O_2), nitrogen (N_2) and water vapour (H_2O) (Equations 4-5 and 4-6). The following two equations can be written in terms of heat capacity (c_p) and temperature instead of the enthalpy.

$$\dot{E}_{in} = \left(\dot{m}_{\mathrm{H_2O}in}\, h'_{\mathrm{H_2O}in}\right) + \left(\dot{m}_{\mathrm{O_2}in} h'_{\mathrm{O_2}in}\right) + \left(\dot{m}_{\mathrm{N_2}in} h'_{\mathrm{N_2}in}\right), \tag{4-5}$$

$$\dot{E}_{out} = \left(\dot{m}_{\mathrm{H_2O}out}\, h'_{\mathrm{H_2O}out}\right) + \left(\dot{m}_{\mathrm{O_2}out}\, h'_{\mathrm{O_2}out}\right) + \left(\dot{m}_{\mathrm{N_2}out}\, h'_{\mathrm{N_2}out}\right), \tag{4-6}$$

where: $\dot{m}$ is the component mass flow rate (kg/s) and h' is the component specific enthalpy (kJ/kg.K).

Increasing the inlet gas temperature warms the liquid and leads to a phase change from liquid to gas. If the liquid condensation at the scrubber inside is ignored, the energy loss due to liquid evaporation can be calculated (Equation 4-7). This liquid evaporation depends on several factors such as temperature difference between the gas and the liquid and the liquid turbulence degree.

$$\dot{E}_{\Delta v} = \dot{m}_{\Delta v}\, h'_{fgL}, \tag{4-7}$$

where: $\dot{m}_{\Delta v}$ is the liquid mass change rate due to evaporation in (kg/s) and it equals $\left(\dot{m}_{\mathrm{H_2O}out} - \dot{m}_{\mathrm{H_2O}in}\right)$ and h'_{fgL} is the liquid latent heat (kJ/kg.K).

The heat loss through the scrubber sides can be calculated using different methods, such as conduction, convection and the combination of convection and radiation. All these methods are discussed in detail in the upcoming transient heat loss estimation section in this chapter.

The scrubber conversion of the mass equation can be written as:

$$\sum \dot{m}_{in} = \dot{m}_{\Delta v} + \sum \dot{m}_{\mathrm{out}}, \tag{4-8}$$

where: $\sum \dot{m}_{in}$ is the sum of masses for all components of the gas phase entering the scrubber and $\sum \dot{m}_{\mathrm{out}}$ is the sum of masses for all phases leaving the scrubber.

4.2. Thermodynamic Model Results and Discussion

All energies and masses were calculated mainly based on the controlled parameters such as Re, θ, LVR and β. All energies calculations also included measured parameters such as temperatures and the relative humidity at different locations. However, it is essential to estimate the heat loss from the scrubber to the ambient and to include this term in the energy balance equation. This heat loss can be estimated using the transient-state heat loss tests. The steady-state assumption cannot be used to estimate the heat loss because this means that the liquid and the metals' temperatures do not change with time, which means there is no heat loss. Further, heat leaves the scrubber from its sides by conduction, then to the surrounding area possibly in one or more than one method such as radiation and/or convection. This section explains these three methods to estimate the heat loss, the comparison between them, the free convection heat transfer coefficient calculations and the steady-state heating experiments.

4.2.1. Estimation of heat loss through scrubber sides

To start the thermodynamic analyses, the heat loss from the scrubber tank should be considered firstly and included in the energy balance equation. This section examines in detail the possible method(s) to estimate the heat transfer from the scrubber boundaries such as conduction, convection and radiation.

4.2.1.1. Conduction between the inner and the outer surfaces of the scrubber

Heat leaves the scrubber towards the outside through its sides because of the temperature difference between the scrubber and the ambient. The thermocouples were placed in different places (Chapter 3, Figure 3-9). Due to turbulence, the measured liquid temperatures at two different places within the liquid have the same value.

The heat loss from the scrubber passing through its sides by conduction can be expressed as:

$$Q_{L\,cond.} = -\left(k_s A_{sb}\frac{(T_L - T_{sb})}{th_s} + k_s A_{sa}\frac{(T_o - T_{sa})}{th_s} + k_p A_{pb}\frac{(T_L - T_{pb})}{th_p} + k_p A_{pa}\frac{(T_o - T_{pa})}{th_p}\right), \tag{4-9}$$

where: k is the thermal conductivity (W/kg.K), A means the surface area (m^2), T means the temperature (K), (th) means the side thickness (m), (s) represents the stainless steel material, (b) means below the liquid surface, (a) means above the liquid surface, (o) means the outlet and (p) means transparent high-temperature resistant polycarbonate sides.

The majority of heat loss passing through the steel part above the liquid surface (Q_{sa}) was 73% of the total heat loss (Figure 4-2). This was for two reasons: the 316 stainless steel thermal conductivity is much higher than the transparent high-temperature resistance polycarbonate (Table 3-1). Also, the 316 stainless steel part above the liquid level has a larger surface area compared with other sides including the 316 stainless steel one below the liquid surface level. The below-liquid level stainless steel side transferred (Q_{sb}) 17% of the total heat loss for the same first reason. The polycarbonate side above the liquid surface had less surface area compared with the below-liquid surface. Therefore, it transferred less heat (Q_{pa}) to the one below (Q_{pb}).

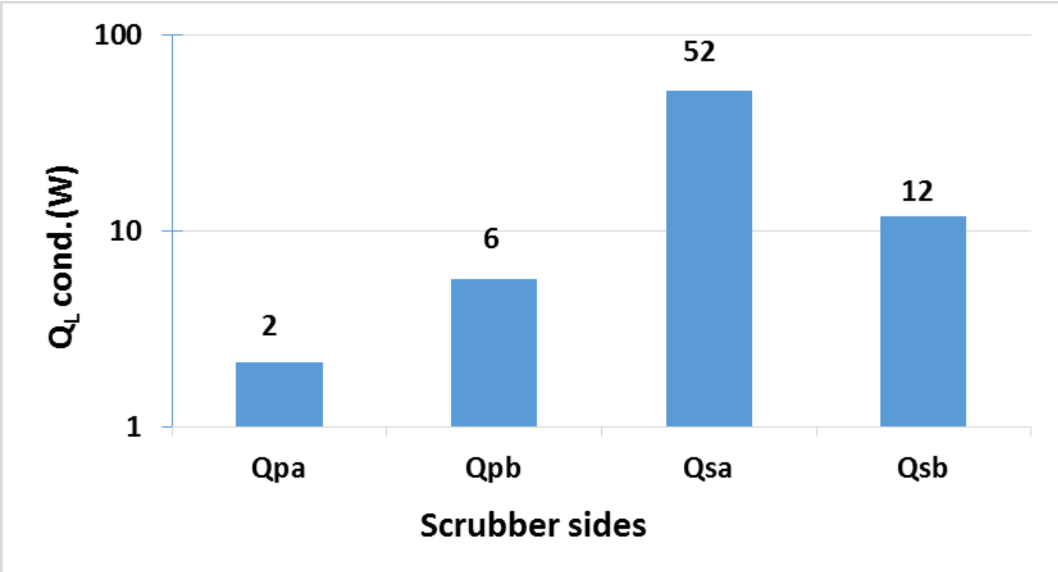

Figure (4-2). Conductive heat transfer for the scrubber sides.

4.2.1.2. Heat transfer from the outer surfaces of the scrubber to the ambient

Heat might leave the scrubber from the outside surfaces in two possible methods, radiation and/or convection. A new approach was used to confirm which one has the major effect on the heat transfer rate. In this approach, the transient heat loss experiments (Chapter 3) were considered, in particular, the section of the transient heat loss estimation experiments. The experimental data was smoothed (Figure 4-3) to remove the curve noise. These curves were analysed carefully to select the start cooling down time. This time represents starting of the transient energy loss. This time was different for each curve such as liquid temperature and above-liquid surface level stainless steel sides' temperature. The temperature drop rate was obtained by considering all five warming up and cooling down experiments (Chapter 3).

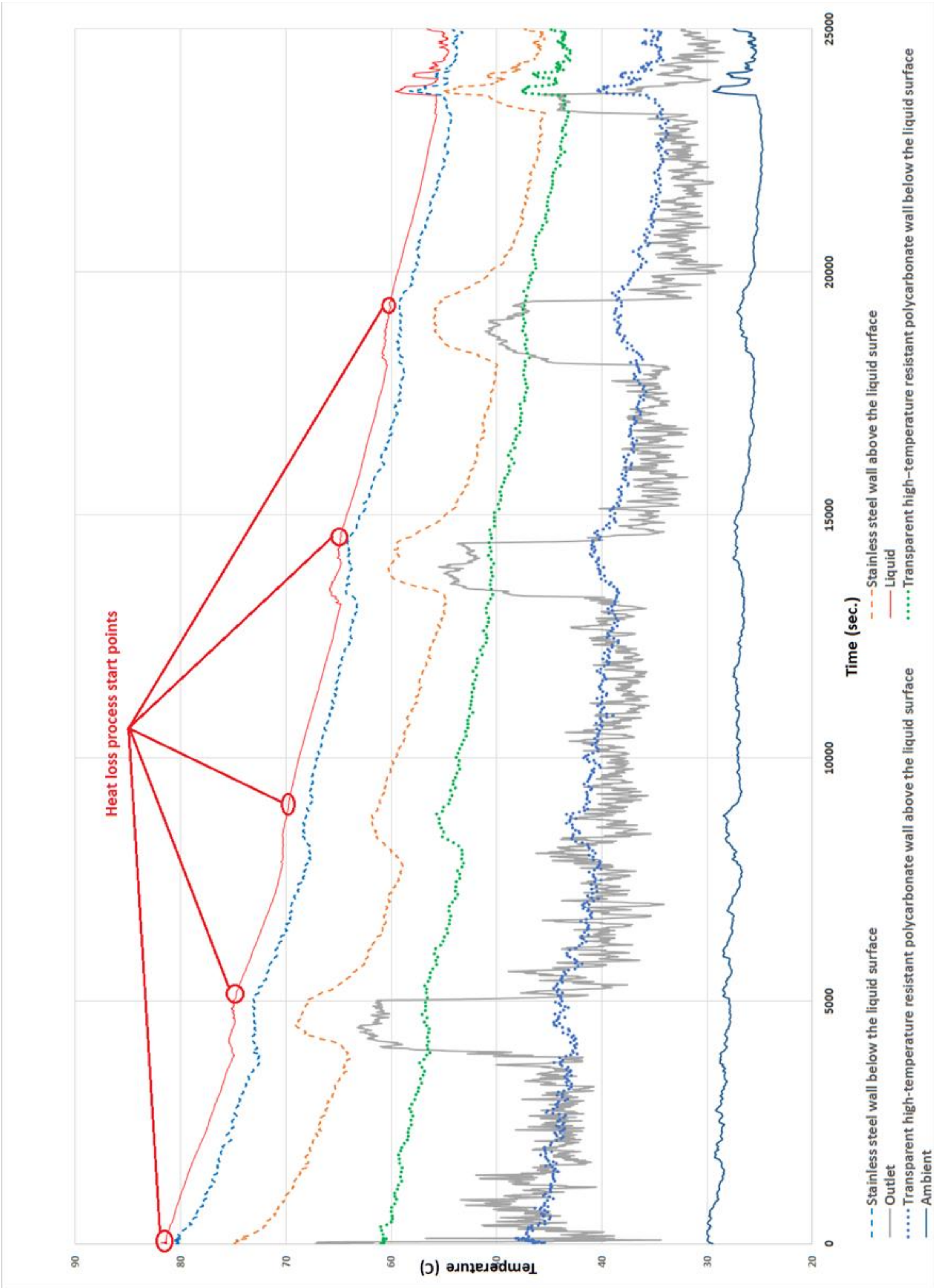

Figure (4-3). The measurement of all temperatures of the transient heat loss estimation experiments.

4.2.1.2.1. Radiation and convection heat transfer

The radiation heat transfer might be contributed to the heat loss from the scrubber to the ambient. Therefore, another approach was used to examine its weight based on the Newton-Stefan cooling law (Equation 4-10) (O'Sullivan 1990):

$$Q_L = A[h(T - T_a) + \epsilon\sigma(T^4 - T_a^4)], \tag{4-10}$$

where: h is the free convection heat transfer coefficient (W/m^2.K), T is the side temperature (K), ϵ is the side emissivity, and σ is the Stefan constant, which is also known as Stefan-Boltzmann constant ($5.67 \times 10^{-8}\ \frac{\mathrm{W}}{\mathrm{m^2K^4}}$).

However, the heat loss cannot be calculated directly using Equation (4-10), because it contains the unknown value of the convection heat transfer coefficient (h). The first step to solve this issue is to re-write Equation (4-10) as:

$$\frac{Q_L}{A} = \epsilon\sigma(T - T_a)^4 + 4\epsilon\sigma T_a(T - T_a)^3 + 6\epsilon\sigma T_a^2(T - T_a)^2 + (h + 4\epsilon\sigma T_a^3)(T - T_a) \tag{4-11}$$

Figure (4-3) was separated into five figures based on the initial heating temperature 80°C, 75°C, 70°C, 65°C and 60°C, respectively. Figure (4-4) represents the heat loss experiments starting from the initial liquid temperature 80°C until the next liquid heating of 75°C. This figure confirmed that the heat loss has four values based on the scrubber side material, the surface area and the temperature differences between the scrubber surfaces and the ambient.

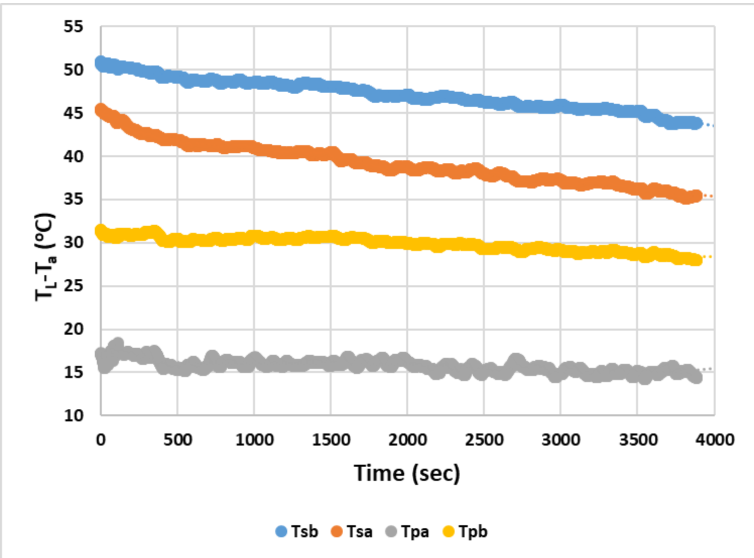

Figure (4-4). The scrubber sides temperatures of the heat loss estimation experiments with initial liquid temperature 80°C.

These curves had the best fit with the polynomial fifth-degree approach. This was used to obtain the following Equation (4-12) with different values for each term as shown in Table (4-2):

$$T = \mathrm{a}\, t^5 + b\, t^4 + c\, t^3 + d\, t^2 + et + f \tag{4-12}$$

where: *t* is the cooling time (sec.) and a, b, c, d, e, f are constants.

Table (4-2). The constant of the best fit equations of the heat loss estimation temperature curves of initial temperature 80°C.

Scrubber side section	***a***	***b***	***c***	***d***	***e***	***f***
Stainless steel below the liquid surface	-1×10^{-16}	1×10^{-12}	-5×10^{-9}	7×10^{-6}	-6×10^{-3}	51
Stainless steel above the liquid surface	-2×10^{-16}	2×10^{-12}	-7×10^{-9}	1×10^{-5}	-1×10^{-3}	45
Transparent high-temperature resistant polycarbonate below the liquid surface	-1×10^{-16}	1×10^{-12}	-4×10^{-9}	6×10^{-6}	-4×10^{-3}	31
Transparent high-temperature resistant polycarbonate above the liquid surface	-7×10^{-17}	8×10^{-13}	-4×10^{-9}	7×10^{-6}	-5×10^{-3}	17

After that, the second derivative of Equation (4-12) yields to:

$$\frac{dT}{dt} = 5\mathrm{a}\, t^4 + 4b\, t^3 + 3c\, t^2 + 2dt + e \tag{4-13}$$

Then, Equation (4-13) was compared with Equation (4-11) to compare the radiation heat transfer with the convection one. The fourth-order term of this equation (5a) represents the radiation heat transfer and the first-order term (2d) refers to the free convection heat transfer. This procedure was repeated for the remaining four tests of initial temperatures 75°C, 70°C, 65°C and 60°C. It was found that the radiation heat transfer just represented 0.4% of the total heat loss. Therefore, it can be neglected because it has insignificant value (Figure 4-5).

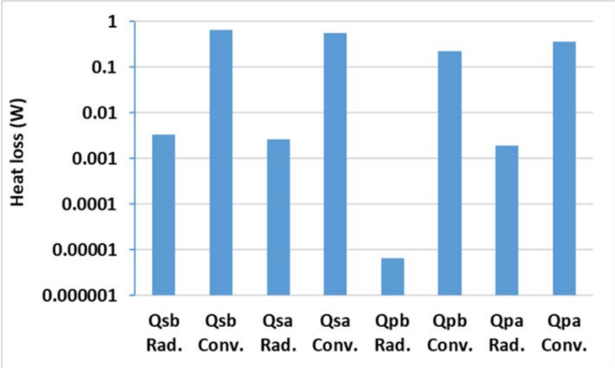

Figure (4-5). Heat transferring from the scrubber to the ambient mainly by convection.

The heat leaving the scrubber from the stainless-steel sides under the liquid surface level were found to be less than the above-liquid surface level, because the above-surface area was larger than the below one. However, the scrubber loss heat from the transparent high-temperature resistant polycarbonate side under the liquid level was higher than the above-surface level, because the above one had the larger temperature difference than the below part. The higher thermal capacity of the stainless steel compared with the transparent high-temperature resistant polycarbonate caused more energy loss from the stainless-steel sides.

4.2.1.2.2. Convection heat transfer

In the previous section, it was confirmed that the radiation heat transfer had a minor effect on the scrubber heat loss. Therefore, the free convection heat transfer considered was based on a different approach. This procedure investigated the five cooling periods separately, including the liquid and the gas inside the scrubber based on heat capacity (Equation 4-14):

$$Q_{L\,conv.} = Q_s + Q_p + Q_l + Q_g \tag{4-14}$$

where: Q_s is the heat loss from all the 316 stainless steel sides, Q_p is the heat loss from the transparent high-temperature resistant sides, Q_l is the heat loss from the liquid, Q_g is the heat loss from the gas above the liquid surface within the scrubber, and the unit of all of these terms are in (W).

The following equations explain in detail each term of Equation (4-14);

$$Q_s = \rho_s th_s c_{ps}\left(A_{sb}\frac{dT_{sb}}{dt} + A_{sa}\frac{dT_{sa}}{dt}\right) \tag{4-15}$$

$$Q_p = \rho_p th_p c_{pp} \left(A_{pb} \frac{dT_{pb}}{dt} + A_{pa} \frac{dT_{pa}}{dt} \right) \tag{4-16}$$

$$Q_l = \rho_l V_l c_{pl} \frac{dT_l}{dt} \tag{4-17}$$

$$Q_g = \rho_g V_g \, c_{pg} \frac{dT_o}{dt} \tag{4-18}$$

Temperature drop curves were obtained based on Figure (4-3) by careful tracking for each scrubber side temperature curve (Figure 4-6).

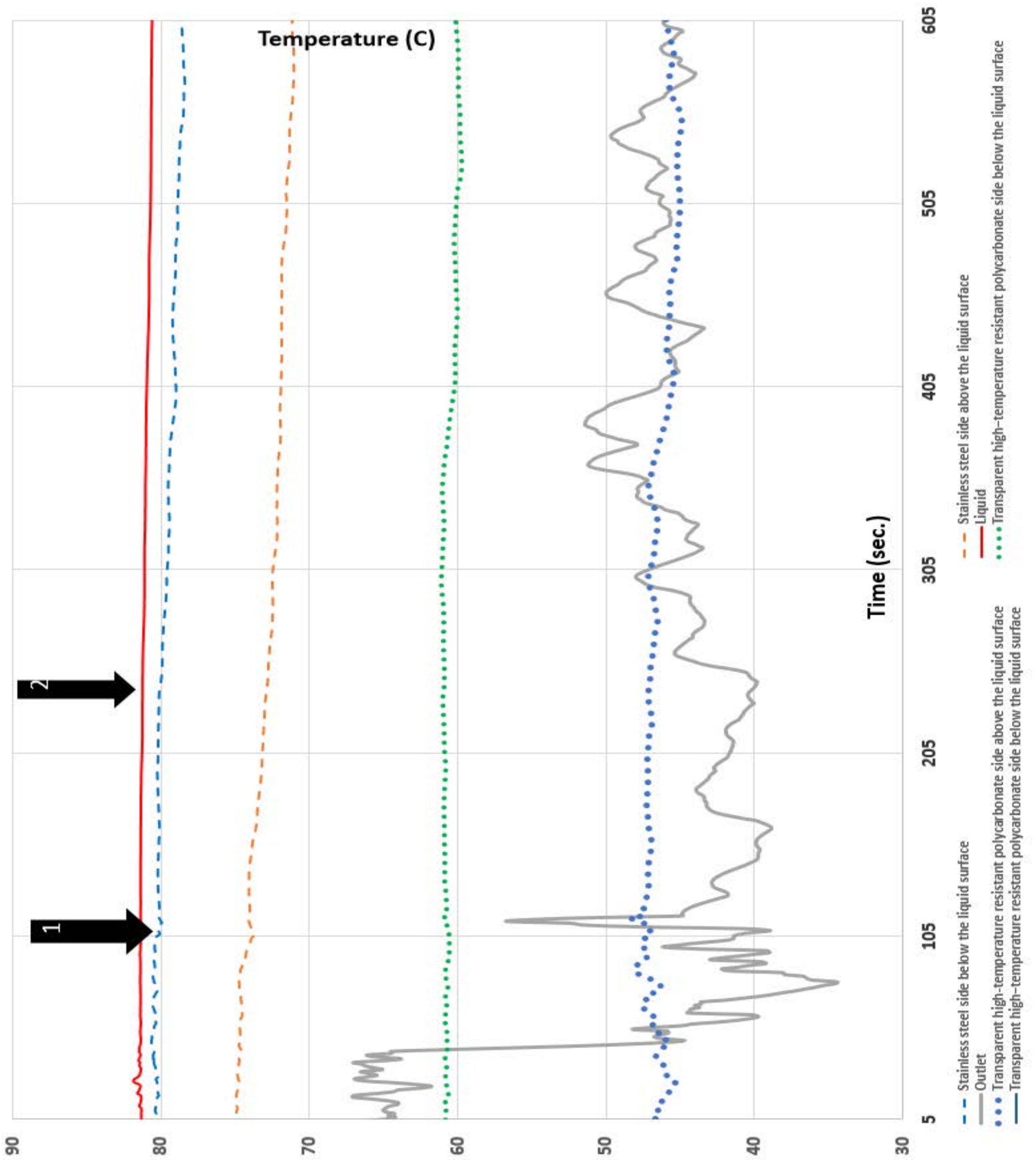

Figure (4-6). Obtaining the accurate start cooling down time of the initial liquid temperature 80°C.

The best fifth-degree polynomial equation curve fit is shown in Equation (4-19). This curve shows that the cooling down experiments started after about 98 seconds, and the temperature differences during this time were about 3°C. Most importantly, each term of Equations (4-15) to (4-16) had a different start cooling down time. This was because of external effects such as the ambient temperature, the surrounding air movement and the liquid turbulence, or/ and an internal effect such as the heat capacity of the metal and the fluid.

$$T_{s\,a} = -3 \times 10^{-8}t^3 + 4 \times 10^{-5}t^2 - 2 \times 10^{-2}t + 76.2 \qquad (4\text{-}19)$$

The first derivative of the previous equation is shown in Equation (4-20). Then, by assuming that this derivative equals zero, the accurate time of start cooling down curve was calculated (Figure 4-7).

$$\frac{T_{sa}}{dt} = -9 \times 10^{-8}t^2 + 8 \times 10^{-5}t - 2 \times 10^{-2} \qquad (4\text{-}20)$$

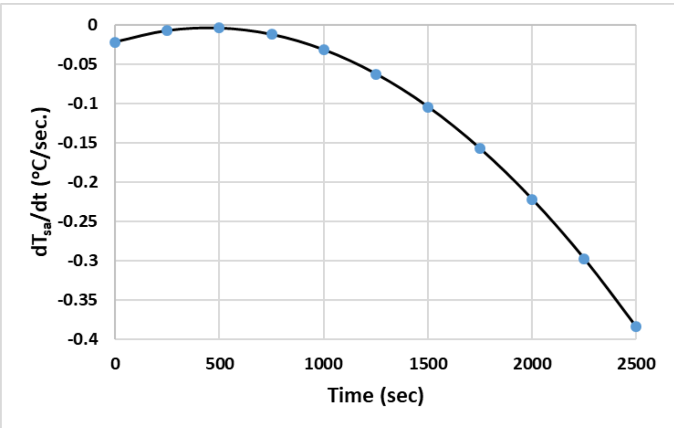

Figure (4-7). Obtaining the accurate time of start cooling down of the initial liquid temperature 80°C, for the steel side above the liquid surface.

The heat loss mentioned in Equations (4-15) to (4-18) can be calculated separately at this temperature (Figure 4-8). Figure 4-8 shows that the major heat loss (88%) is dependent on the liquid. The heat loss from the gas above the liquid comes in the second order with 3.5%. The heat left the scrubber from the polycarbonate sides with 5.6% divided into two parts: 4% from the below liquid surface and 1.6% from the above liquid sides. Minimum heat loss was found at 2.9% of the total heat loss with 1.9% from above the liquid surface and 1% from below the liquid surface.

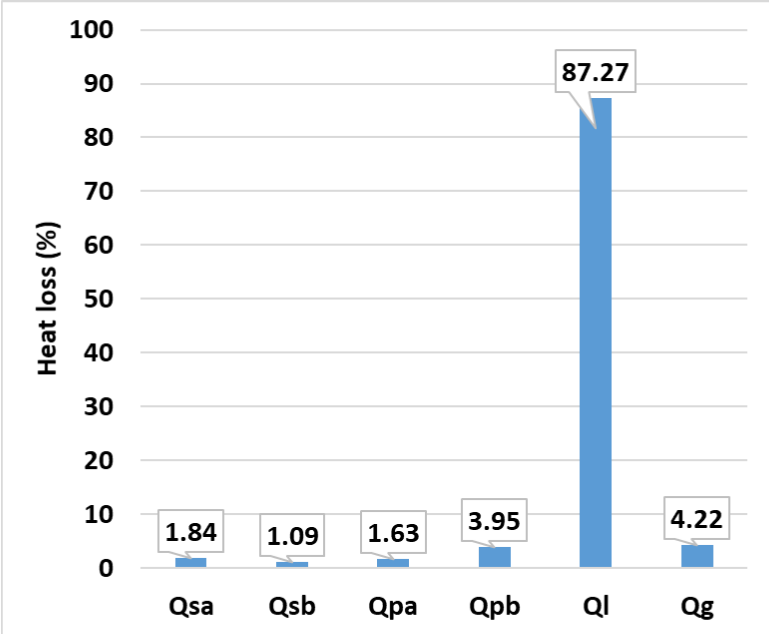

Figure (4-8). Convection heat loss percentage at the initial liquid temperature of 80°C.

For accurate results, the same procedure was repeated for the remaining heating up and cooling down experiments of initial temperatures 75°C, 70°C, 65°C and 60°C. The results of the five cooling down tests are shown in Figure (4-9).

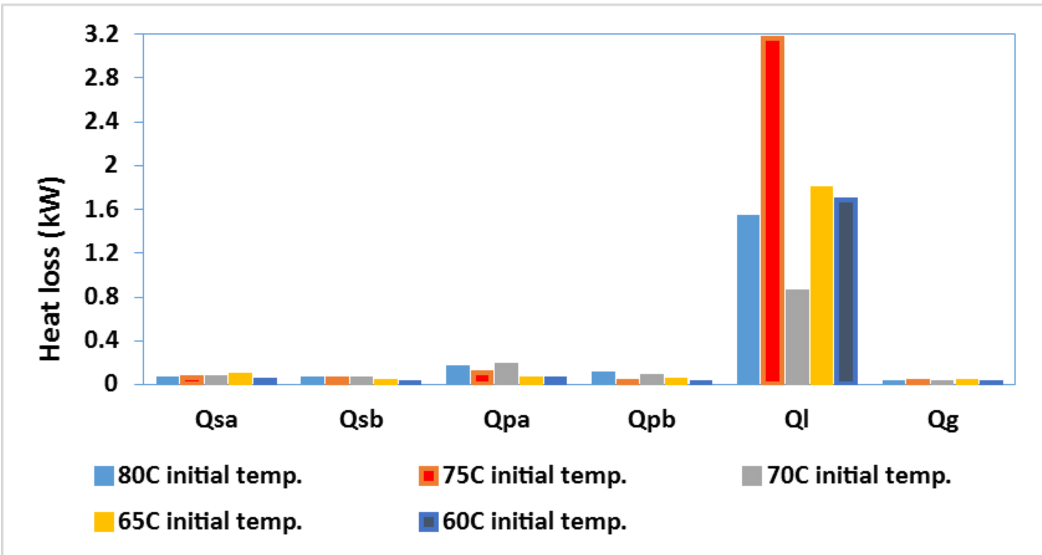

Figure (4-9). Scrubber heat loss components.

By combining all results from Figure (4-9), it was found that heat leaves the scrubber in different rates (Table 4-3).

Table (4-3). Heat leaving the scrubber at different percentages.

Q_l (%)	Q_g (%)	Q_{pb} (%)	Q_{pa} (%)	Q_{sb} (%)	Q_{sa} (%)
87	1	2.5	5	1.5	3

Based on this method, the liquid temperature has a major effect on the scrubber heat loss (Figure 4-9 and Table 4-3) because the liquid has higher heat capacity and larger mass. Therefore, the heat loss from the scrubber can be considered as a function of the liquid temperature only. In other words, increasing the liquid volume ratio inside the scrubber would play a positive role in reducing the outlet gas temperature. However, the heat loss from other components of the scrubber has minor significance. Two reasons for that are that the gas heat capacity is always much less than the liquid heat capacity, and the scrubber sides have a smaller mass compared with the liquid.

Lastly, the relation between the heat loss from the scrubber and the liquid temperature is shown in Equation (4-21) and Figure (4-10). It confirms that the heat loss increases due to increasing the liquid temperature because of the temperature difference increment between the liquid and the ambient. Three points of this curve were far from the average line, and this could be a result of inaccurate estimation of the start cooling down time and/or the equation type temperature drop rate curve. For example, Equation (4-9) might not be polynomial and/or it might have a different order. Indeed, this linear equation is the simplest fit to start the investigation and it can be used in future to be more accurate. This correlation can be used to estimate the heat loss from this scrubber only because it is in a dimensional form.

$$Q_L = 0.113\, T_l - 5.1 \qquad (4\text{-}21)$$

where: Q_L in kW and T_l in $^{\circ}$C.

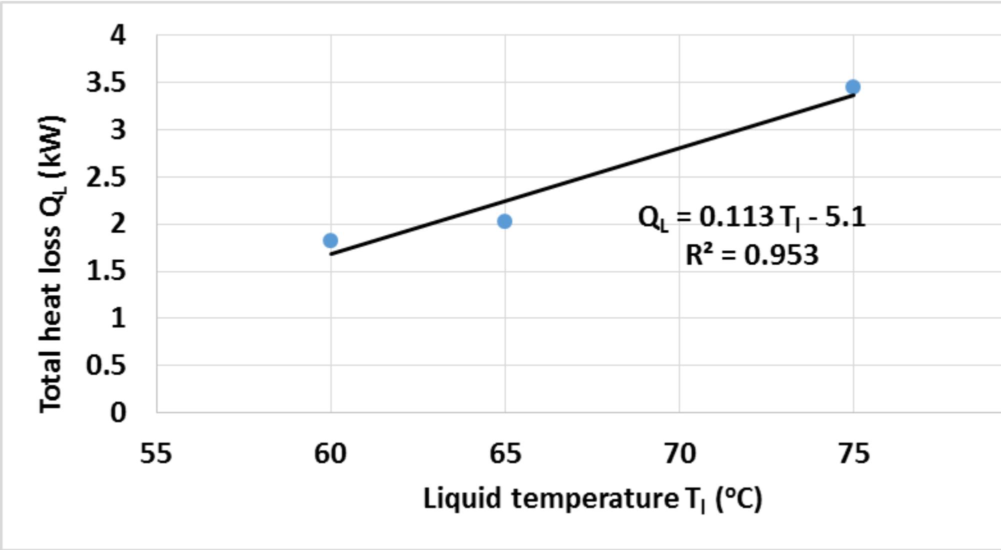

Figure (4-10). The relation between the scrubber heat loss and the liquid temperature.

4.2.2. Heat loss estimation methods comparison

Heat leaves the scrubber mainly from the above liquid surface of the stainless-steel scrubber sides (Figures 4-2 and 4-5) by conduction or by combining radiation and convection. This was because of the larger surface area of the stainless steel above the liquid compared with others in addition to the higher heat capacity of the stainless-steel metal compared with the polycarbonate sides. However, the convection method showed that this side transfers heat as a second major comparing with others. Indeed, this could be as a result of a slight error in the estimated time of the start cooling down process.

Another important matter is that the heat loss through the scrubber sides can be calculated based on the conduction Equation (4-9) or the convection Equation (4-21) as mentioned earlier in this section. It also can be obtained by applying the first law of thermodynamics for the steady-state approach on the scrubber (Equation 4-4). The conduction heat transfer equation can be applied for all of the four sides sections: above and below the liquid surface level for both the transparent high-temperature resistant polycarbonate and the stainless-steel sides. This value was much higher than the calculated heat loss from the energy balance (Figure 4-11 refers to the case of 1,200 Re, 20% LVR and N/A β). Figure (4-11) confirmed that the conduction method is not suitable for calculating the heat loss from the scrubber. This could be a result of some impractical assumptions such as that the outside surface temperature for each section is uniform and constant; the inner scrubber surface temperature equals the liquid temperature for the below-liquid surface level, and as the outlet gas temperature for the above one.

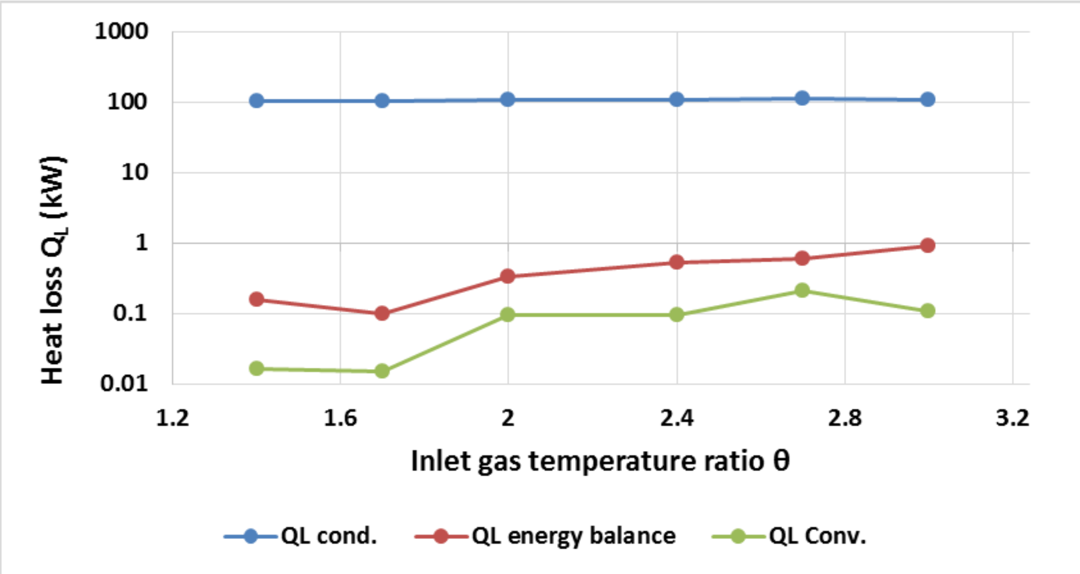

Figure (4-11). Comparison between the conduction, the convection and the energy balance heat loss at 1,200 Re, 20% LVR and N/A β.

The heat loss was estimated based on the slope of the heat loss experiments that were achieved without involving any condition of the inlet gas such as the flow rate and/or the temperature. Both of these two parameters played a significant role in the scrubber performance as explain later in this chapter and the next one.

The radiative heat transfer was neglected because it had an insignificant value (Figure 4-5). However, the major heat loss from the scrubber depended on the liquid (Figure 4-8). Therefore, the heat loss from the scrubber was estimated based on the liquid temperature only in the energy balance calculation. Added to this, the convection heat transfer that was calculated using Equation (4-21) had a value lower than the one calculated from the first law of thermodynamics (Figure 4-11). To match the heat loss calculated based on energy balance, a compensating factor C is added in Equation (4-21). The new form of this equation is shown in Equation (4-22) and Figure (4-12). This equation can be applied for this scrubber only at 3,300 Re, 38% LVR and 0.15 β. For other operating conditions, this constant C should be based on the inlet gas Reynolds number and the liquid volume. The results of the constant *C* for all other steady-state heating tests are available in Table (B-1) in Appendix B.

$$Q_L = C\ (0.113T_l - 5.1) \tag{4-22}$$

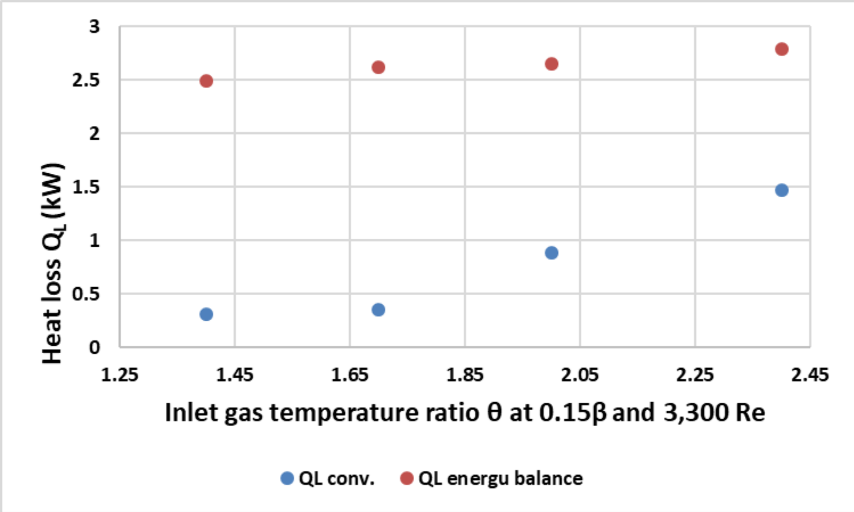

Figure (4-12). Heat loss comparison between the convection and the energy balance at 3,300 Re, 38% LVR and 0.15 β.

Furthermore, Figure (4-13) suggests that the heat loss from the scrubber was a function of the inlet gas temperature ratio because it increased the temperature differences between the scrubber inside and the ambient. However, increasing the inlet gas Reynolds number had a non-uniform effect on the heat loss due to the liquid turbulence. Therefore, it is extremely complex to obtain the relationship between the scrubber heat loss and the inlet gas Reynolds number. This shall be investigated in the future research.

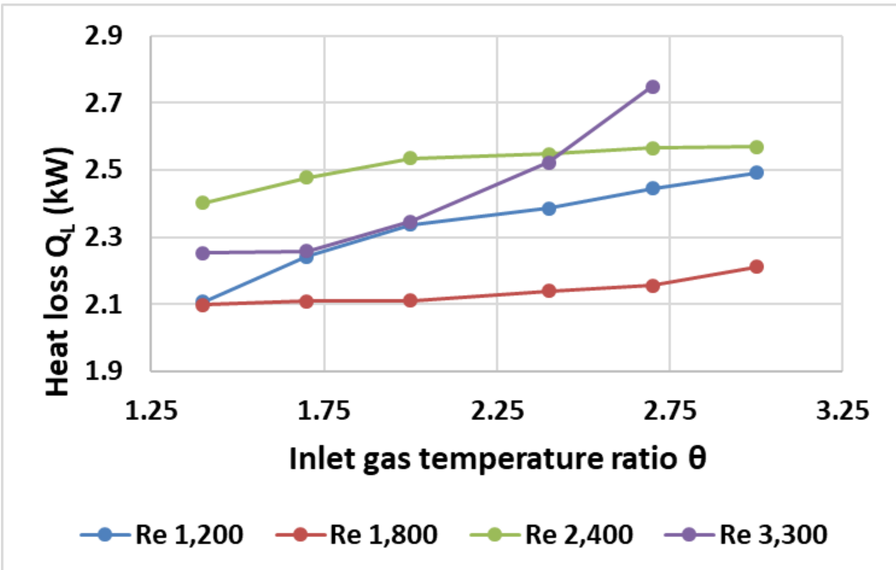

Figure (4-13). Dependency of the heat loss on the inlet gas flow rate and temperature.

4.2.3. Free convection heat transfer coefficient calculations

This section confirms that heat transfers from the scrubber sides to the ambient by convection. For the transient heat loss estimation, the free convection heat transfer coefficient between the scrubber and its surroundings was assumed constant and has a uniform value. Indeed, it can be calculated using two different methods. The first one depends on the heat loss from all of the scrubber components and the liquid, and it can be calculated from:

$$Q_L = hA(\Delta T), \tag{4-23}$$

where: h is the free convection heat transfer coefficient (kJ/kg.K) and ΔT is the temperature difference between the outside scrubber surfaces and the ambient (K).

The free heat transfer coefficient can be calculated also using some empirical correlations such as Churchill & Chu (Incropera and DeWitt 2002):

$$\overline{Nu} = \left[0.825 + \frac{0.387\mathrm{Ra}^{1/6}}{\left(1 + \left(\frac{0.492}{\mathrm{Pr}}\right)^{9/16}\right)^{8/27}}\right]^2, \tag{4-24}$$

where: $\overline{Nu}$ is the mean Nusselt number, Ra is the Rayleigh number and Pr is the Prandtl number.

This correlation depends on some non-dimensional numbers, such as Rayleigh and Nusselt numbers (Table 4-4). There are some differences between the experimental and the empirical values of the free convection heat transfer coefficient as shown in this table. These differences are due to some assumptions related to the characteristic length calculations and the surfaces' orientation. Also, both Rayleigh and Nusselt numbers are decreased due to reducing the liquid temperature. This as a result of decreasing the heat transfer from the scrubber due to temperature differences between the scrubber and the ambient. This correlation could cause an error up to 25% due to the ambient turbulence and the surface roughness (Incropera and DeWitt 2002). Current error percentages are shown (Table 4-4) for the coefficient. This confirms that the heat loss estimation at the initial liquid temperatures of 80°C and 70°C was incorrect due to the absence of the inlet gas effect as mentioned in the explanation of Equation (4-22). Therefore, we ignored both of them in obtaining the heat loss estimation Equation (4-21) based on Figure (4-10).

Table (4-4). The average values of the outer surfaces of scrubber sides.

Initial liquid temperature (T_l) (°C)	**$h_{experimental}$ (W/m^2.K)**	**$h_{empirical}$ (W/m^2.K)**	**Error in h (%)**	**Ra**	**Nu**
80	7.44	5.2	30	7.6×10^8	113
75	5.9	5	15	6.6×10^8	108
70	10	4.7	53	5.6×10^8	103
65	4.9	4.6	6	5.2×10^8	101
60	4.8	4.5	6	4.6×10^8	97

4.2.4. Steady-state heating experiments

The calculations of these experiments were achieved depending on the raw data obtained by considering all the steps mentioned in Chapter 3 (experimental design and methodology, section 3.2). The following sections explain all energies related with the two phases.

4.2.4.1. Inlet energy

The system receives energy from the inlet gas only, and this energy was calculated using Equation (4-5). Increasing the inlet gas temperature ratio and/or Reynolds number increased the inlet energy because this energy depends on enthalpy and mass of both of the gas components. In Figure (4-14), the orifice ratio of 0.2 was chosen to show this effect because it has the same liquid volume ratio to eliminate this parameter effect. Table (4-5) shows that both LVR and β do not affect the inlet gas energy because this energy was calculated at the system inlet.

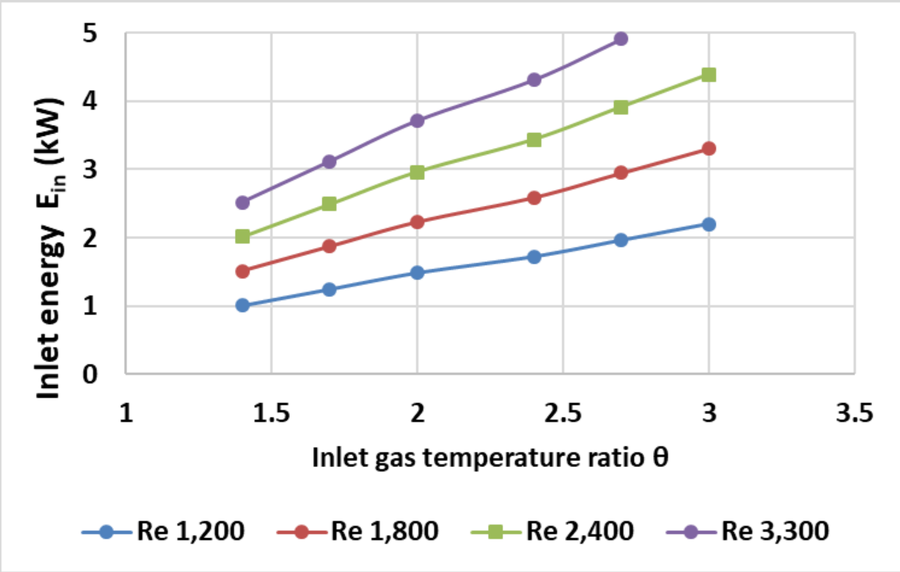

Figure (4-14). The relation of the inlet energy and the inlet gas condition.

Table (4-5). The inlet gas energy (kW) independent on LVR or β.

θ	1.4	1.7	2	2.4	2.7	3
1,200 Re, 0.2 β, 42% LVR	1.01	1.25	1.49	1.72	1.96	2.2
1,200 Re, 0.15 β, 38% LVR	1.02	1.25	1.48	1.72	1.96	2.2
1,800 Re , 0.2 β, 42% LVR	1.52	1.86	2.23	2.59	2.95	3.31
1,800 Re , 0.15 β, 38% LVR	1.52	1.85	2.23	2.59	2.95	3.31
2,400 Re , 0.2 β, 42% LVR	2.04	2.5	2.96	3.44	3.94	4.39
2,400 Re , 0.15 β, 38% LVR	2.04	2.5	2.96	3.44	3.9	4.39
3,300 Re , 0.2 β, 42% LVR	2.55	3.11	3.71	4.31	4.82	
3,300 Re , 0.15 β, 38% LVR	2.55	3.11	3.71	4.31	4.8	

4.2.4.2. Outlet energy

The energy carried out by the gas that was calculated using Equation (4-6) increased slightly due to increasing the inlet gas θ (Figure 4-15 and Table 4-6). Also, Table (4-6) shows the outlet gas energy was more dependent on the inlet gas Reynolds number. However, the outlet gas energy is independent on liquid volume ratio or the orifice ratio.

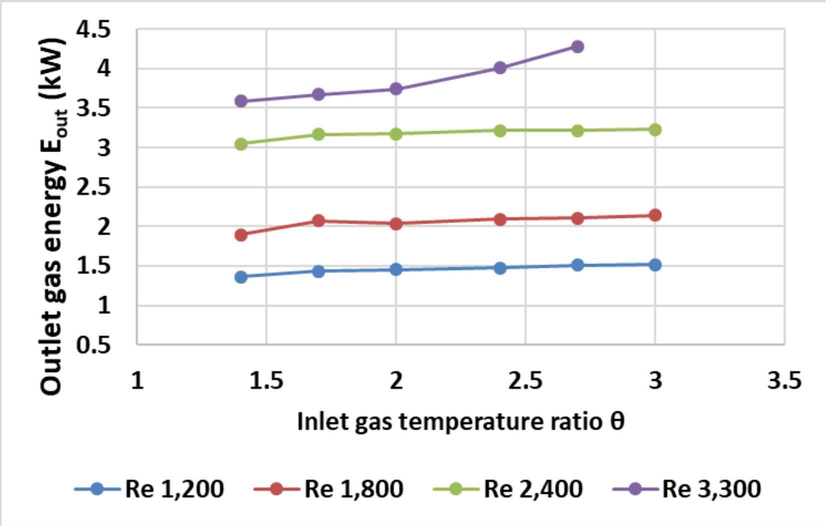

Figure (4-15). The relation between the outlet energy and the inlet gas condition.

Table (4-6). The outlet gas energy (kW) independent on LVR or β.

θ	1.4	1.7	2	2.4	2.7	3
1,200 Re, 0.2 β, 42% LVR	1.14	1.29	1.45	1.47	1.5	1.51
1,200 Re, 0.15 β, 38% LVR	1.09	1.3	1.46	1.5	1.55	1.59
1,800 Re , 0.2 β, 42% LVR	1.57	1.86	2.03	2.07	2.1	2.15
1,800 Re , 0.15 β, 38% LVR	1.62	1.86	2.08	2.1	2.11	2.2
2,400 Re , 0.2 β, 42% LVR	2.27	2.7	2.94	3.1	3.14	3.18
2,400 Re , 0.15 β, 38% LVR	2.19	2.53	3.23	3.37	3.4	3.47
3,300 Re , 0.2 β, 42% LVR	2.92	3.26	3.73	4.02	4.31	
3,300 Re , 0.15 β, 38% LVR	2.83	3.31	3.73	4.3	4.65	

Increasing the inlet gas temperature reduced the outlet to the inlet energies ratio (Figure 4-16). At a low inlet gas Reynolds number, this ratio has a minimum value due to less mixing between the two phases. This ratio decreased due to increasing the inlet gas temperature ratio. This means that the gas transferred more energy to the liquid because of temperature differences. The inlet energy might be transferred into the evaporative one and/or leave the scrubber through its sides at high Re and/or θ of the inlet gas.

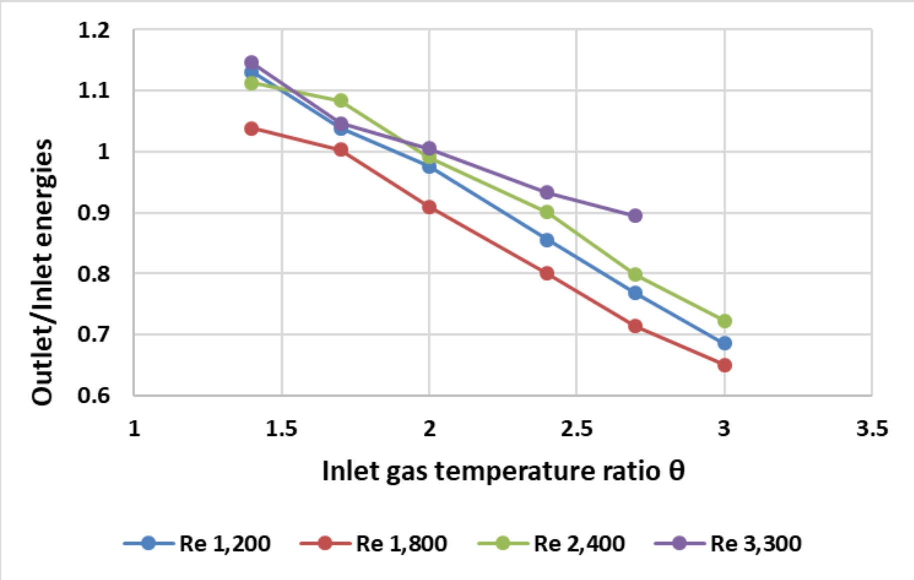

Figure (4-16). The relation between the outlet/inlet energy ratio and inlet gas temperature ratio.

The outlet gas energy increases by increasing the inlet gas Reynolds number. This is because of the time reduction required to transfer the inlet energy to other forms such as heat loss through scrubber surfaces. In other words, increasing inlet gas Re and/or θ plays a negative role in scrubber performance. Also, increasing the liquid volume ratio and/or adding the orifice plate did not affect the leaving energy. The results of other operating condition are shown in Table (B-2) in Appendix B.

4.2.4.3. Evaporative energy

The liquid evaporated from the scrubber as a result of inlet gas temperature being higher than the boiling temperature of the liquid. Increasing the inlet gas temperature ratio and/or Reynolds number increased the evaporation rate (Figure 4-17). The evaporated mass was calculated from the scrubber mass balance. Table (B-3) in Appendix B contains all results of the liquid mass evaporation.

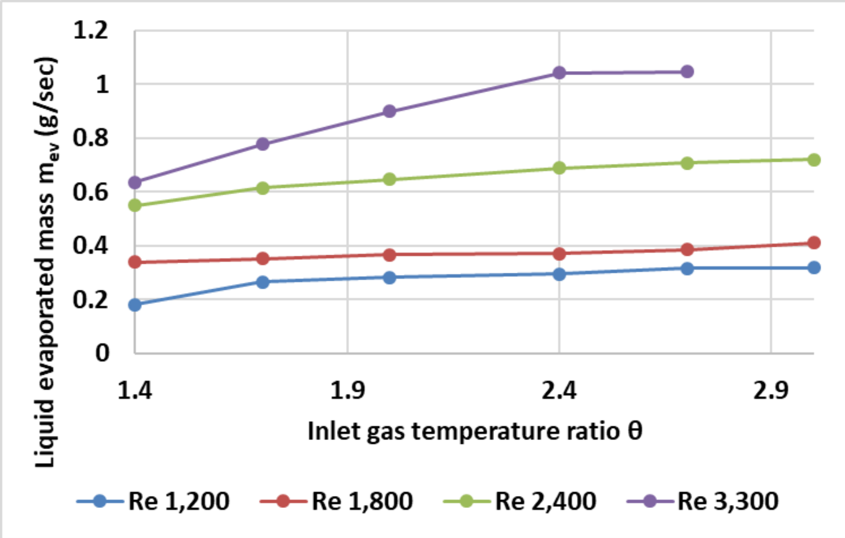

Figure (4-17). The evaporated liquid mass and the inlet gas Re and θ.

Increasing the liquid evaporation increased the evaporative energy, which was calculated using the Equation (4-7) due to phase change (Figure 4-18).

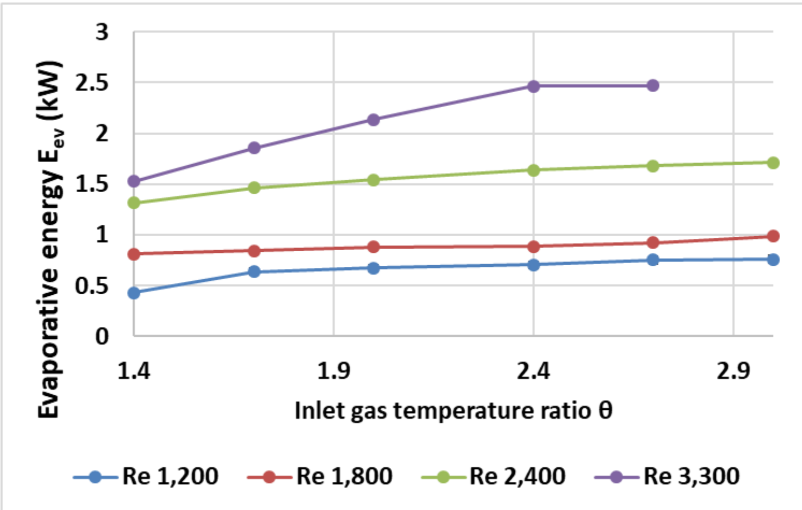

Figure (4-18). The effect of the inlet gas condition on the evaporative energy.

Moreover, Figure (4-19) illustrates that increasing the inlet gas θ reduced the liquid evaporation/inlet energy ratio for all tests. However, increasing liquid volume ratio and/or adding the orifice plate did not affect the evaporative energy.

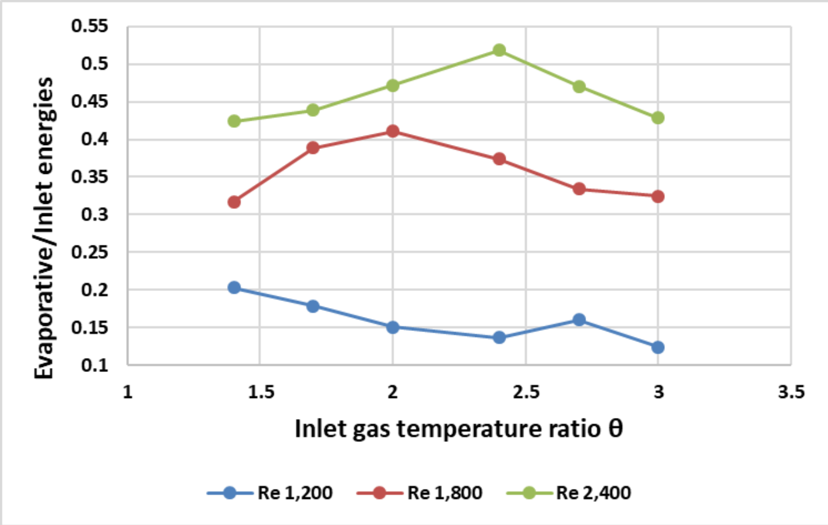

Figure (4-19). The relation between the evaporative/inlet energies ratio to θ.

4.3. Outlet Gas Humidity

The outlet gas relative humidity calculation is explained in detail in this section. The relative humidity was calculated using the energy and mass balances of the scrubber. The calculated result was compared with the measured ones from Chapter 3.

4.3.1. Outlet gas relative humidity calculations

Reducing the outlet gas humidity was one of the main aims of this project because the high humidity at the scrubber outlet caused the DPF blockage and increased the overall production cost (Abdulwahid et al. 2018). Further, the energy loss from the scrubber was estimated based on Equation (4-21). The theoretical outlet gas energy was calculated based on this heat loss using Equation (4-4). After that, the outlet gas relative humidity was calculated based on this theoretical outlet gas energy.

During some of the steady-state heating experiments, the calculated outlet gas relative humidity showed an over-prediction of using the scrubber energy and mass balances in addition to some differences between this RH and the measured ones (Figure 4-20). This could be a result of the humidity probe error ±4%, and the inlet gas condition estimation error mentioned earlier in this chapter, in addition to another error caused by heat loss (Equation 4-21). To eliminate this error, the inlet gas condition must be measured separately for each test. This required some modifications to the apparatus. In average, 10.25% error was found between the calculated and measured outlet gas relative humidity is shown in Figure (4-20). This average error can be calculated from Equation (4-25):

$$Average\ error = \frac{1}{N}\sum_{1}^{N}\frac{|RH_{cal} - RH_o|}{RH_o} \times 100\%, \tag{4-25}$$

where: N is the number of tests.

For some tests of the inlet gas temperatures ratios below the 1.7, the measured relative humidity values varied between 74% and 86%, due to the lower inlet gas energy required to evaporate saturated vapour. Indeed, increasing the inlet gas Re and/or θ would increase the liquid evaporation and hence the outlet gas relative humidity.

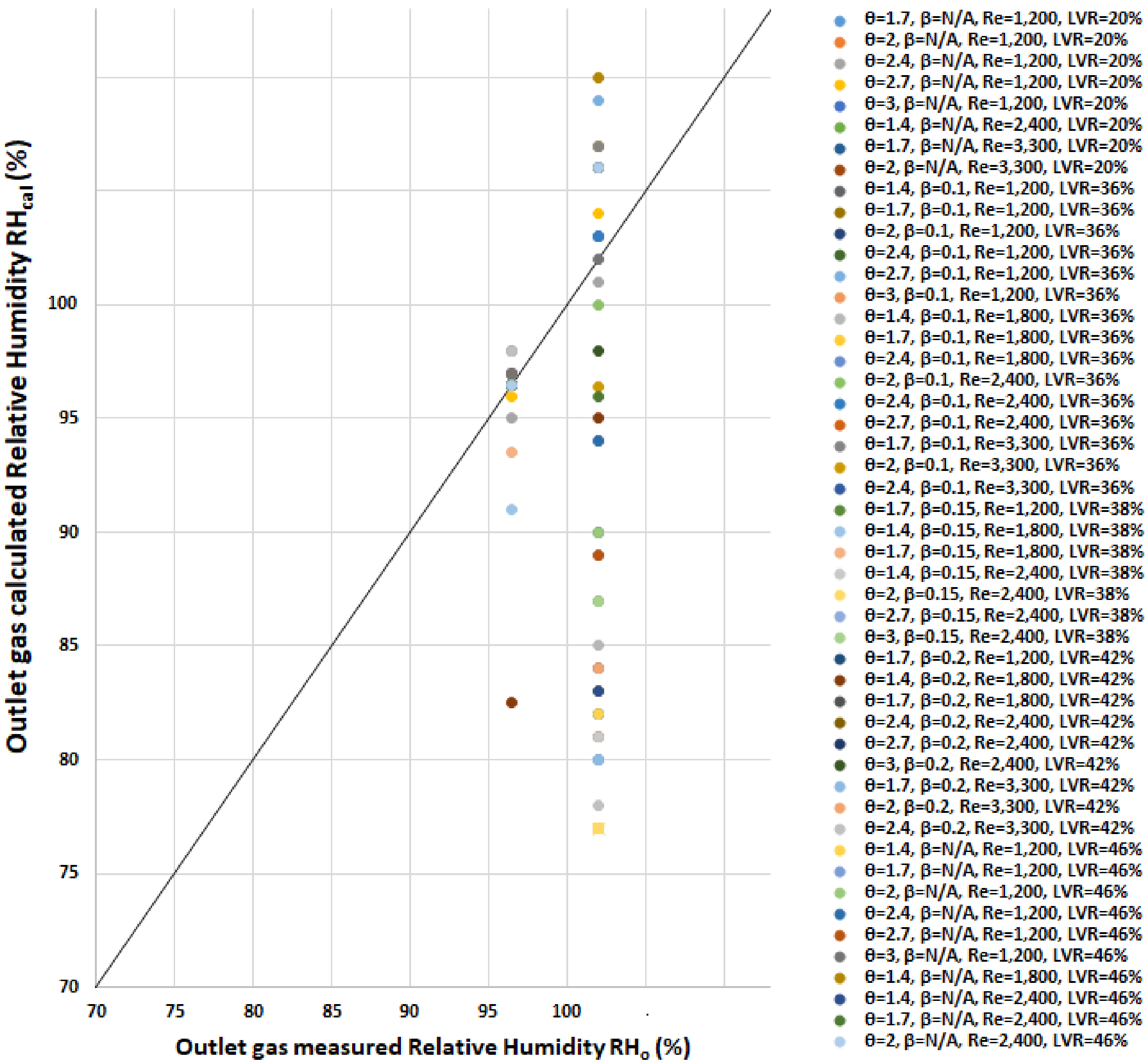

Figure (4-20). Measured and calculated relative humidity of the outlet gas.

4.3.2. Comparison with the experimental results

The measured data confirmed that the gas left the scrubber mostly in a saturation condition (considering the humidity probe error ±4%). However, the outlet gas relative humidity at the inlet gas temperature ratio of 1.4 was measured at 74-90% (Figure 4-20). This means that there was a slight amount of the inlet gas energy at this temperature transformed to the evaporative one. This explains why the outlet gas temperature mostly equals the liquid temperature. The minimum exhaust gas temperature measured at half load at the exit of a diesel engine (just before the scrubber) was about 300°C (Al-Shemmeri and Oberweis 2011). In other words, this project investigated inlet gas temperatures much higher than the actual ones.

4.4. Conclusion

This chapter investigated the wet scrubber thermodynamically for different operating conditions in a non-dimensional form, in particular, the inlet gas Reynolds number range 1,200-3,300 and temperature ratio 1.4-3, in addition to orifice ratios range N/A, 0.1, 0.15 and 0.2, and the liquid volume ratio range 16-48%. The raw data from Chapter 3 was used in this investigation. The scrubber was analysed based on the steady-state heating experiments, the first law of thermodynamics and the continuity equation. However, the heat loss from the scrubber was calculated based on the transient convection heat transfer. This is the most suitable method compared with others such as conduction and radiation. Based on the convection approach, the liquid temperature had the major effect on the heat loss from the scrubber. The other possible methods of heat loss from the scrubber were explained and compared in detail.

The results show that increasing the liquid volume ratio reduced the outlet gas temperature. Scrubber performance can be affected by increasing the inlet gas temperature ratio and/or Reynolds number in several ways, in particular, increasing the liquid evaporation and the inlet energies, outlet energies and evaporative energies. However, increasing the liquid volume ratio and/or adding the orifice plate did not affect the leaving energy and the evaporative energy. The results confirmed that the gas leaves the scrubber mostly in a saturation condition. Finally, scrubber performance can improve thermodynamically by reducing the inlet gas flow rate and/or temperature.

Chapter 5 – Heat Transfer Analysis of the Wet Scrubber

The previous chapter dealt with the whole scrubber as one control volume while this chapter investigates the interaction between the gas bubbles and their surrounding liquid. This approach treats the bubble itself as a control volume. The experimental data from Chapter 3 is used in this chapter in non-dimensional form to investigate the heat transfer of the scrubber. This chapter explains in detail the effect of increasing the inlet gas Reynolds number (Re), the inlet gas temperature ratio (θ) and the orifice ratio (β) on the bubble size, motion and heat transfer. This chapter consists of five main sections: the experimental set up, the observed flow characteristics, the flow image analysis, the results and discussion and the final correlations. The first section explains the flow visualisation system, the experimental methodology and the necessary assumptions to analyse the scrubber using the heat transfer model. The flow is described in section two, in addition to explaining the three flow regions in most inlet gas flow rates. Thousands of images and videos are analysed in section 3 using *ImageJ* software. Section four explains in detail the results and a discussion, followed by the final non-dimensional correlations that can be applied to optimise scrubber performance and/or to suggest a new scrubber design.

5.1. Experimental design and methodology

5.1.1. Non-dimensional parameters set-up

This study investigates the effect of the inlet gas temperature, the orifice size and inlet gas flow rate on the scrubber performance in terms of non-dimensional forms. The non-dimensional forms are the inlet gas temperature ratio (θ), the orifice size ratio (β) and the inlet gas Reynolds number (Re) respectively. The experimental procedure was explained in detail in Chapter 3, in particular, the section of *flow visualisation experiments*. In these tests, both the liquid Prandtl number and liquid volume ratio were maintained constant at 7.6 and 42% respectively. Also, the liquid volume ratio, the liquid type and the liquid temperature were maintained constant to eliminate possible effects on scrubber performance. For example, changing the liquid type means changing the properties, and this effects the heat transfer rate. Another example, increasing the liquid volume ratio increases the traveling time of gas through the liquid.

Three different orifice sizes were tested because bubble visualisation becomes simpler and more accurate using the orifice plate. It also investigates the orifice size effect on the bubble heat transfer. This study does not include the case of the inlet pipe without the orifice plate due to the complexity of monitoring the bubbles as a result of turbulence (Figure 3-12).

Further, Table (5-1) explains the current 16 operating conditions in non-dimensional form, which represents Table (3-4) in dimensional form.

Table (5-1). The non-dimensional form of the operating conditions.

Test number	Re	θ	Pr*g*	β
1	1,200	1, 1.3, 2, 2.6, 3	0.698-0.726	0.1
2	1,800	1	0.698	0.1
3	2,400	1	0.698	0.1
4	3,300	1	0.698	0.1
5	1,200	1	0.698	0.15
6	1,800	1	0.698	0.15
7	2,400	1	0.698	0.15
8	3,300	1	0.698	0.15
9	1,200	1	0.698	0.2
10	1,800	1	0.698	0.2
11	2,400	1	0.698	0.2
12	3,300	1	0.698	0.2

5.1.2. Image analysis set-up

Bubble size, shape and distribution were investigated using the image analysis method. *ImageJ* software was used successfully to analyse several sequences of images and videos for each operating condition. A glass ball with a known diameter (Figure 5-1) was used to calibrate the images and to convert the measurements from pixels to millimetres.

Figure (5-1). *ImageJ* software calibration.

After calibration, both videos and images were converted to a form of 8-bit. Then, a suitable threshold from the process command (after comparing several threshold) was applied on the binary images to increase the analysing efficiency of *ImageJ* software. Analysing these images and movies using *ImageJ* provided all the details about the bubble motion such as their position, area and orientation in several options. One option was to outline all bubbles with red numbers (Figure 5-2).

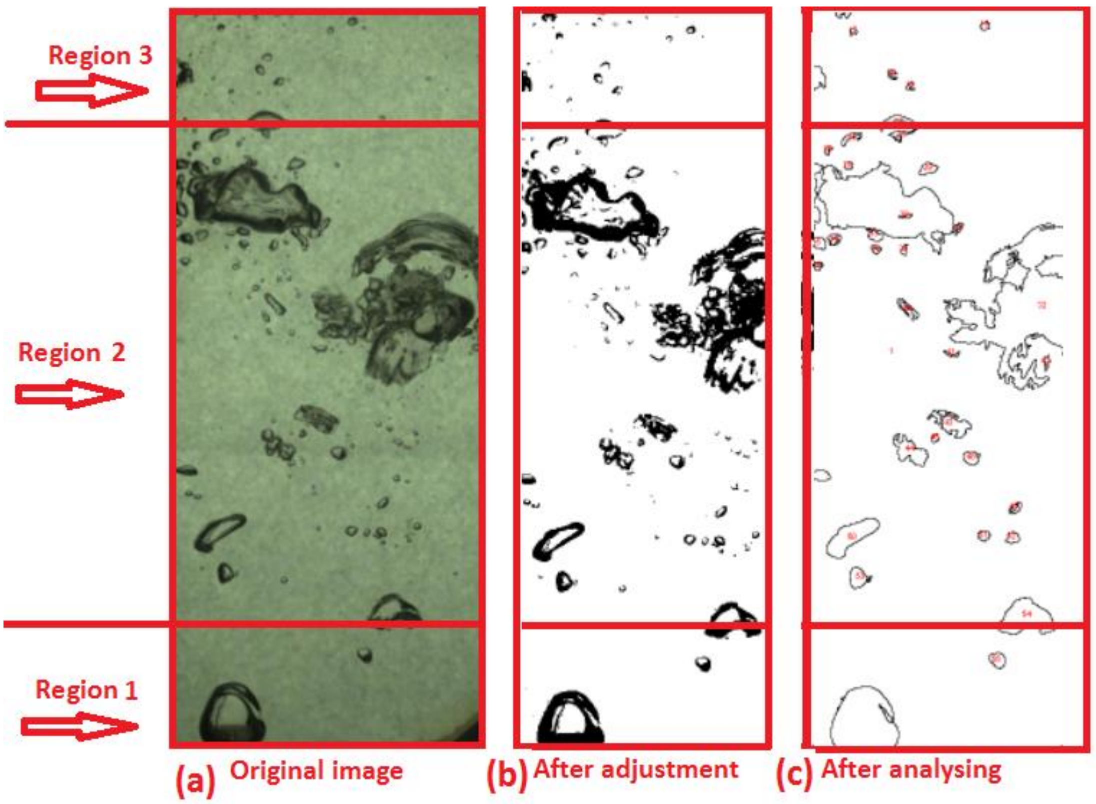

Figure (5-2). Image processing using *ImageJ* software.

Following this analysis, important parameters from *ImageJ* were provided in a separate file (Figure 5-3) which can be converted to an Excel sheet as required. These details will be used later in this chapter with the bubble heat transfer model. The numbers in the left column of Figure (5-3) refer to the given bubbles, and the label refers to the name of the image or the video at a specific time. Area, X, Y, Angle and Circ. represent the projected area, the position in the x-direction, the position in the y-direction, the angle and the circularity, respectively of the corresponding bubble at that specific time.

Results

File Edit Font Results

	Label	Area	X	Y	Angle	Circ.
1	5mm 100C_20180904	33473.695	125.505	107.634	138.483	0.051
2	5mm 100C_20180904	151.439	256.956	217.156	3.358	0.051
3	5mm 100C_20180904	3.767	232.589	220.364	5.834	0.460
4	5mm 100C_20180904	2.600	246.381	219.914	169.167	0.547
5	5mm 100C_20180904	9.233	276.376	215.292	172.313	0.260
6	5mm 100C_20180904	5.200	292.418	215.330	178.352	0.363
7	5mm 100C_20180904	10.294	232.997	213.621	158.783	0.285
8	5mm 100C_20180904	36.613	268.517	210.143	7.990	0.056
9	5mm 100C_20180904	6.845	229.634	211.150	170.052	0.191
10	5mm 100C_20180904	4.935	252.311	210.219	3.385	0.446
11	5mm 100C_20180904	3.078	159.606	208.223	8.869	0.208
12	5mm 100C_20180904	2.282	289.668	207.486	144.588	0.534
13	5mm 100C_20180904	8.490	210.936	205.913	113.473	0.635
14	5mm 100C_20180904	7.535	243.786	204.198	87.985	0.416
15	5mm 100C_20180904	2.759	171.484	201.257	10.834	0.708
16	5mm 100C_20180904	5.359	244.127	198.601	103.951	0.271
17	5mm 100C_20180904	2.016	137.636	199.722	15.092	0.686

Figure (5-3). *Image J* software optional results sheet.

5.1.3. Assumptions

Some assumptions should be considered to simplify the heat transfer investigation of the wet scrubber. Firstly, the bubble contents are homogeneous. Therefore, the temperature and the pressure within the bubble are always uniform. The gas inside the bubble is only air (there is no liquid vapour) and it is assumed to follow the ideal gas law. Further, both liquid and gas have constant properties. Although the fluid compressibility can be important in bubble collapse, it is assumed to be constant (Harris et al. 2004 and Funada et al. 2005). Most importantly, the events occur extremely rapidly for significant mass transfer of the contaminant gas to occur between the bubble and the surrounding liquid. This means no mass transfer between the bubble and the surrounding liquid.

5.2. Flow Characteristics Observation

At low inlet gas Reynolds numbers, the bubble path can be divided into three regions. The appearance, the formation and the development of these flow regions were affected strongly by the flow turbulence. At high inlet gas Reynolds numbers, the formation was extremely rapid. Therefore, only the churn-turbulent region was recognised. Although some of this was explained in Chapter 3, key points are repeated here to explain some flow observations using *ImageJ* software. Table (5-2) shows the average percentage of these three regions for the three orifice ratios compared with the total liquid height for different tests based on *ImageJ*.

Table (5-2). The three regions' average height percentage compared with the total liquid height.

Re	θ	The height of the departing region (%)	The height of the churn-turbulent region (%)	The height of the bubbly region (%)
1,200	1, 1.3, 2, 2.6, 3	23	55	22
1,800	1	20	62	18
2,400	1	17	70	13
3,300	1	0.0	100	0.0

5.2.1. Region one / departing region

The first region of the wet scrubber flow was located directly above the orifice, and it contained clear recognition bubbles. These bubbles were defined as parent or mother bubbles, and they moved upward. Their growth was smooth for the low inlet gas Reynolds number. At this case, maximum bubble size occurred after a short time directly above the orifice. This maximum bubble size also was a function of the orifice ratio: for example, the large one had produced larger bubbles than the smaller orifice ratio. Most bubbles travelled separately from the others without breaking or overlapping. This region was limited vertically from the orifice until the next region, and it was influenced by the inlet gas flow rate. For example, its height was found about one-quarter (23% based on *ImageJ* software) of the total liquid height at inlet gas Reynolds number of 1,200. The region height was much less than that for the higher inlet gas Reynolds number. This region was independent of the liquid volume ratio and the inlet gas temperature. *ImageJ* confirmed that the next region started when the bubbles cannot be recognised separately because of a high percentage of bubble overlap.

5.2.2. Region two / churn-turbulent region

The second region was located downstream and upward of the departing region directly. The bubbles were very chaotic and shaped rapidly. This region can be recognised by

ImageJ software by the area where bubbles start overlapping, breaking up and coalescencing. This region contained both large bubbles due to coalescence, and small bubbles as the result of bubble breakup. Some bubbles from the departing region may also be present. These bubbles were in continuous change of shape and size. A high percentage of bubbles was observed overlapping in this region. Most important, the turbulence of the flow directed number, shape, size and movement direction of the bubbles in this region. This is a good agreement with Clift et al. (1978) who suggested that in multiphase flow equipment, the bubbles' size distribution is led by the bubble breakup and coalescence dynamics. These bubbles moved upward towards the liquid surface or/and in a horizontal direction towards the interior scrubber sides. At a high inlet gas Reynolds number, the bubbles' travelling time from the orifice to the liquid surface was very short. Therefore, the formation of this region depended strongly on the inlet gas Reynolds number and liquid volume ratio. However, this formation was independent of the orifice ratio. The following sections explain in detail the effect of these parameters on the bubble of this region.

5.2.2.1. Bubble breakup

Bubbles broke up horizontally and/or vertically into several smaller bubbles with different sizes (Figure 5-4) due to several parameters, such as the pressure difference inside the bubble (Simmons et al. 2015). Figure (5-4) represents a bubble breaking up with equal periods of time between each image. This period of time differs for each inlet gas Reynolds number, as well as for each bubble at the same Reynolds number. In turbulent flow, bubbles break up as a result of the interaction with turbulent eddies, the high shear rates, or instability due to internal circulations (Bandara and Yapa 2011). Also, Hinze (1955) added that eddies with a length scale smaller than the bubble size can break the bubble while larger eddies just transport the bubble. In other words, at a higher Reynolds number, the inertial forces acting on the bubble break it up based on the Ohnesorge number, the Weber number, the viscosity and the shape factor (Qian et al. 2006). Further, the surface tension stabilises the interface while the viscous forces slow the growth rate of the bubble. Therefore, the bubble surface becomes unstable (Clift et al. 1978). Indeed, both the gas dissolution and the pressure changed the bubble size slightly, compared with the breakup one when the turbulence is dominant (Bandara and Yapa 2011).

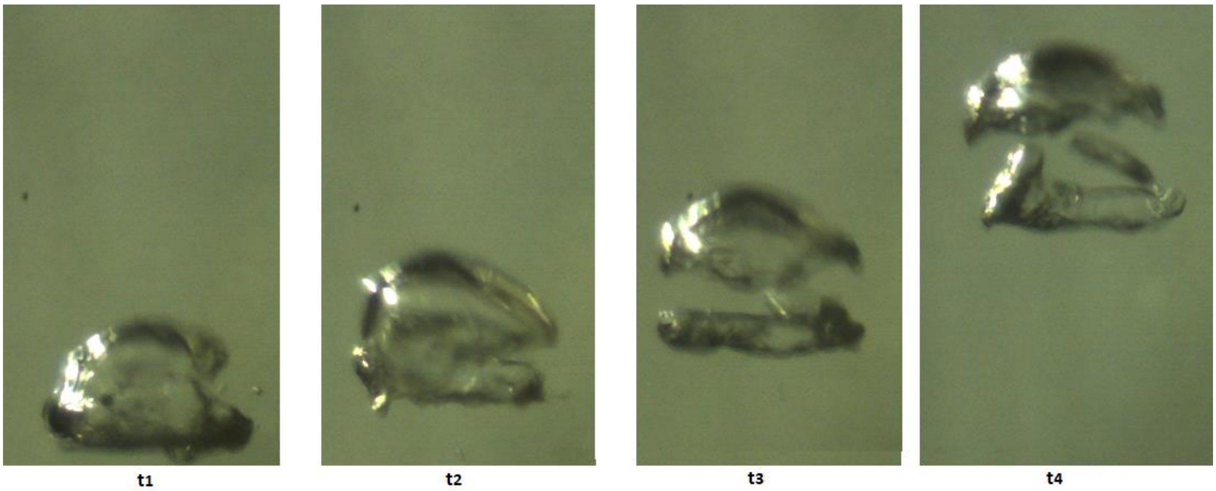

Figure (5-4). Bubble breaking up at Re 1,200 with equal time periods between each image.

5.2.2.2. Bubble coalescence

Bubble coalescence occurs when at least two bubbles collide (Figure 5-5). At this point, the thin liquid barrier between these bubbles ruptures to form larger bubbles (Studley 2010). The coalescence of two bubbles or more in turbulent flows occurs in three steps. Bubbles collide, trapping a small amount of liquid between them. Then this liquid drains until reaching the critical thickness at which time the film ruptures and merges bubbles (Bandara and Yapa 2011). In turbulent gas plumes, bubbles collide as a result of the turbulence and/or the buoyancy. Although the bubble sizes can be changed due to gas dissolution and pressure change, this change is small compared with that caused by the coalescence when the turbulence is dominant (Bandara and Yapa 2011). As mentioned in the past section, Figure (5-4) represented bubble coalescence steps with equal periods of time between each image. This period of time differed for each inlet gas Reynolds number, and for each bubble at the same inlet gas Reynolds number. Moreover, the coalescence rate was defined as the product of collision frequency and the coalescence efficiency. Several factors control the collision frequency such as the bubble sizes, the volume fraction, the dispersed phase collision speed and the system energy dissipation, while the collision efficiency is affected by the continuous and the dispersed phases properties, for example, the liquid viscosity and the interfacial tension.

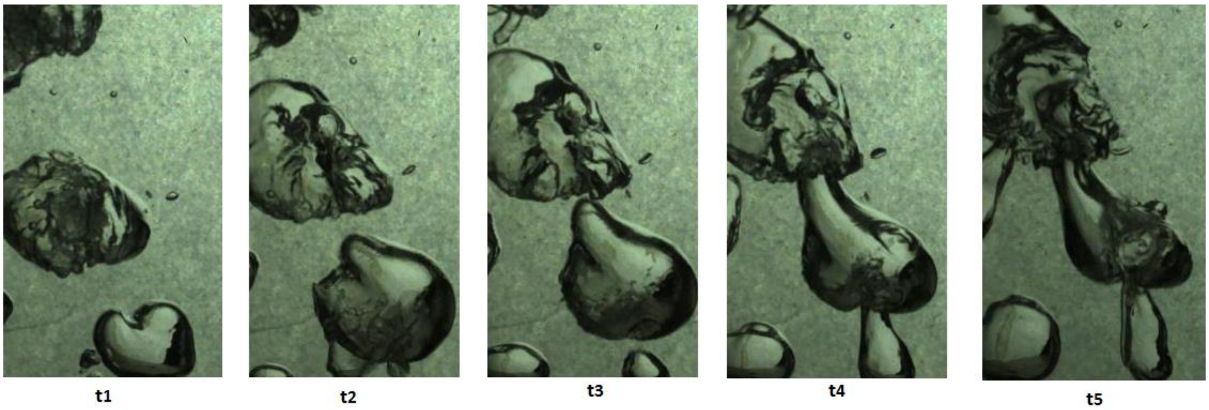

Figure (5-5). Bubble coalescence at Re 1,200 with equal time periods between each image.

5.2.2.3. Bubble overlapping

Bubble overlapping, blurriness and varying shapes make their identification more complex (Laakkonen et al. 2005). Therefore, separating touching and overlapping bubbles is essential for accurate size and shape estimation (Korath et al. 2007). However, in binarisation, many overlapping objects are detected as one large single object (Watano and Miyanami 1995). Many scientists have attempted to solve this issue. The circle pattern matching method for any degree of overlapping was used by Watano and Miyanami (1995). Their method depends on an inscribed circle fitting, which segregates the overlapping objects. However, the Watano and Miyanami (1995) method cannot measure the shape of these objects. The overlapping objects can be segregated using one or two cycles, and they can be considered as one object if they cannot be segregated after more than three cycles (Figure 5-6).

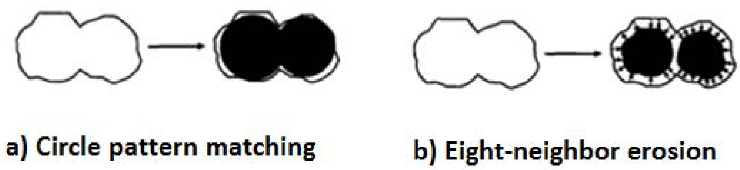

Figure (5-6). Representing more than one object by one shape (Watano and Miyanami, 1995).

Another method based on dividing the planar curve into circular arcs was used effectively by Shen et al. (2000) to recognise overlapped particles in the image. This method consists of three steps: detecting the edge of the overlapped particles, dividing this edge into circular arcs, and grouping these arcs belonging to the same circle. Moreover, Korath et al. (2007) developed an automatic algorithm to separate the touching and the overlapping particles

(Figure 5-7). It depends on the intensity variations of the regions of touching and overlapping particles and the geometric features of the boundary curves. To identify these regions, the geometric features of the boundary curves should be combined with the intensity variations. Major steps in the image processing of this method include pre-processing, segmentation and feature extraction (Korath et al. 2007).

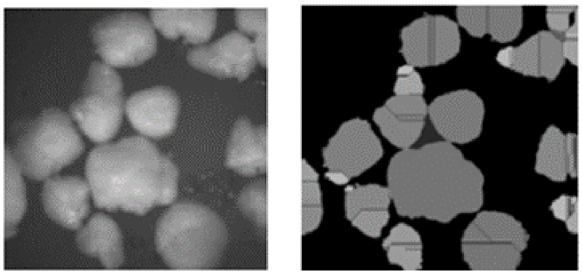

Figure (5-7). Separating the overlapping bubbles (Korath et al. 2007).

Honkanen et al. (2010) investigated the overlapping objects by outlining their slope and their curvature to find the connecting points of the overlapping objects. These connecting points possess a negative curvature peak, whereas the positive curvature refers to the other points (the curve turns towards the centre). Zhang et al. (2012) suggested that two methods could be used to investigate the bubbles overlapping in the digital image. The first one ignores the overlapping bubbles by the constraint condition. Any circular object has the shape factor at least 0.85. The second method identifies the overlapping bubbles by the object recognition approach. This method was more accurate than the first one because the large bubbles had more opportunities to overlap with the smaller size bubbles (Zhang et al. 2012).

Another method was introduced also by Zhang et al. (2012) and depended on using the overlapping elliptical bubble recognition to find the bubble size. This method consists of two steps: contour the segmentation and segment the grouping. For the contour segmentation, the concave points in the dominant point sequence were always assumed as the connecting points. The criterion segment grouping used the average distance deviation. Evaluation of this method used both simulated images and real bubble images. In the wet scrubber investigation, it is very complex to analyse the churn-turbulent region using the three-dimensional approach or any other methods because of the large scrubber wet diameter (94.5cm×47cm), especially using only one high-speed video system.

5.2.3. Region three / bubbly region

The third region of the flow in the wet scrubber was located between the churn-turbulent region and the liquid surface. The appearance of this region was led by turbulence also. This region started when *ImageJ* recognised most bubbles without overlapping upward region 2. This means that this point was the first boundary of this region and it was limited by the liquid surface. It contained small bubbles that shaped after breaking up the bubbles of region two into smaller ones. These bubbles were defined as the outlet or daughter bubbles. Most of these bubbles burst at the liquid surface with temperatures equal to the outlet gas temperature. However, some of these small bubbles were moved horizontally and/or downward towards the interior sides of the scrubber due to the flow turbulence effect. This means all bubbles burst out at the low inlet gas Reynolds number. Moreover, this region was independent of the orifice ratio, the liquid volume ratio and the inlet gas temperature ratio.

5.3. Image Analysis

Bubble motion was recorded as images and videos using a high-speed video system. Both images and videos were processed effectively using *ImageJ* software. The investigated parameters that could affect the scrubber performance can be explained as followed:

5.3.1. Bubble size/ SMD (d_{32})

Several correlations were obtained by scientists to find bubble size in terms of the gas flow rate or Reynolds number and/or the orifice size and/or the fluid properties (Table 2-1) (Abdulwahid et al. 2018). For the scrubber flow, bubble size mainly depended on the inlet gas Reynolds number and this size was increased differently for each bubble with time (Figure 5-8). In the departing region, the growth time was different for each bubble for the same inlet gas Reynolds number. This growth time decreased as the inlet gas Reynolds number increased. This growth was continued until it reached the effect of turbulence. This means that bubbles break and/or collapse in addition to overlap.

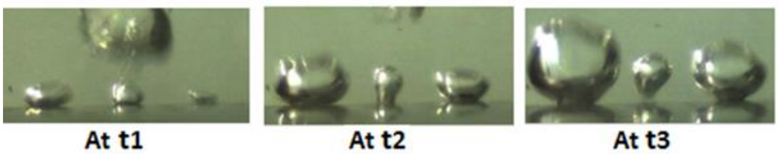

Figure (5-8). Bubble growth with time at Re 1,200 with equal time periods between each image.

Bubbles leave the orifice and travel upward with continuous increase in volume (Figure 5-9). This upward movement of nearly a steady-state volume increment continued until the bubble reached the churn-turbulent region. The shape of the bubble experienced several changes from spherical through ellipse to finally non-uniform. Then, the bubble started to slow down vertically but speed up horizontally due to the effect of turbulence. At the same time, the bubble experienced break-up into at least two bubbles in addition to collapse and/or overlap with other bubbles.

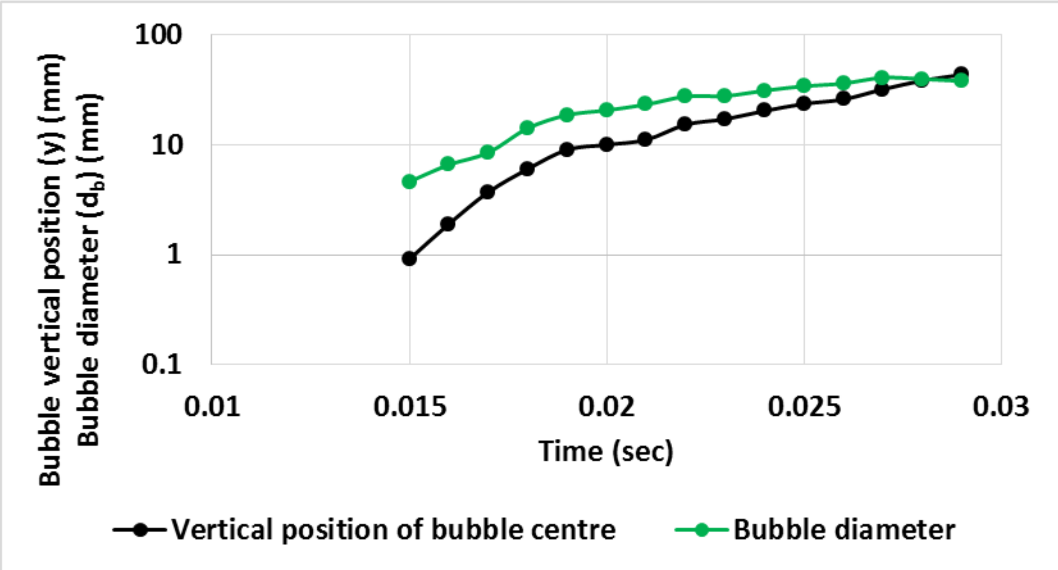

Figure (5-9). The relation of bubble vertical motion and diameter with time.

To calculate the bubble size within the departing region, *ImageJ* software provided the projected area (A_P) of any bubble (Ziegenhein 2016). The projected area is the two-dimensional measured area of the three-dimensional object. Then, the equivalent bubble diameter can be calculated based on the spherical bubble assumption from Equation (5-1) for all calculations included in this chapter (Abdulwahid et al. 2018b). This spherical assumption is the closest shape for most bubbles, in particular regions 1 and 3. However, Asar and Hormozi (2014) assumed that bubbles have an ellipsoidal shape. *ImageJ* software can provide the projected area of the bubbles based on the ellipse shape.

$$d_{ei} = \sqrt{\frac{4A_{pi}}{\pi}} \tag{5-1}$$

Occasionally, a bubble's projected area might be different from the exact area. There are two reasons for this difference. Firstly, our results were achieved based on a two-dimensional study of a three-dimensional large tank. This large volume contained a number of bubbles that cannot be ignored in addition to the effect of bubble overlapping in the accuracy of bubble area calculation. Another reason is related to *ImageJ* software (Figure 5-10). Some bubbles had a non-uniform shape, which caused differences in the gas density inside the bubble. Therefore, the pixel would be different for the same bubble (Figure 5-10) in particular bubbles (B1-1), (B1-2) and (B1-3). The same figure confirmed that *ImageJ* was effective in the area measurement as shown in bubbles (B2-1), (B2-2) and (B2-3).

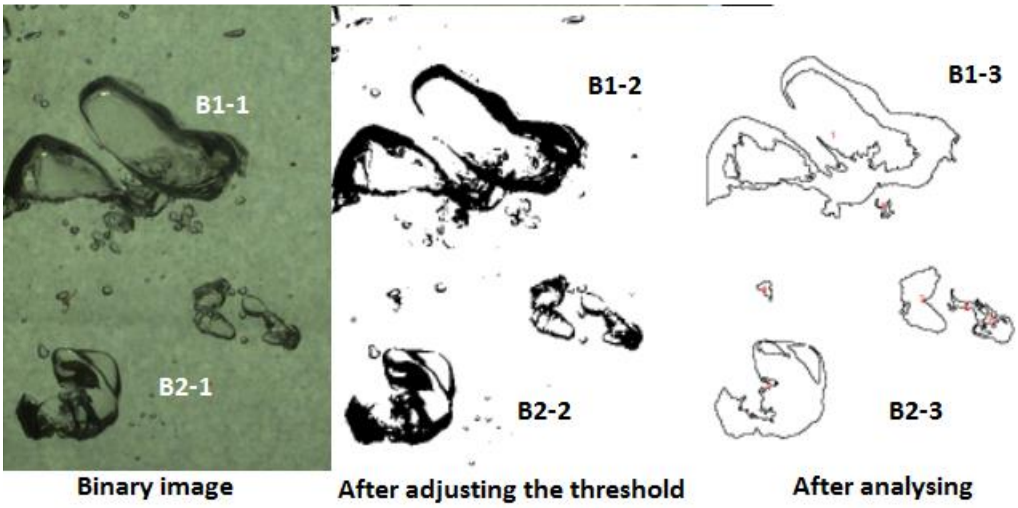

Figure (5-10). Area measurement using *ImageJ* software.

Bubbles have non-uniform shapes as explained earlier (Figure 5-8) because of their travelling in the liquid and being affected by several forces. Therefore, the Sauter Mean Diameter (SMD, d_{32} or D[3,2]) was the best option to calculate the average bubble size from Equation (5-2) (Pacek et al. 1998, Loth et al., 2004, Tang et al. 2007, Vinnett et al. 2009, Filippa et al. 2012, Asar & Hormozi 2014, Kowalczuk & Drzymala 2015, Besagni & Inzoli 2017). The equivalent diameter was processed using MATLAB software to calculate both the volume and the area of all bubbles within region 1. Then, these values were applied in Equation (5-2) to obtain d_{32}. This diameter was calculated particularly for the first region only to eliminate the effect of any bubble overlap, breakup and coalescence on the bubble size.

$$d_{32} = \frac{\sum_{i=1}^{i=N} d_{ei}^3}{\sum_{i=1}^{i=N} d_{ei}^2}, \qquad (5\text{-}2)$$

where: N is the total number of monitored bubbles and d_{ei} is the equivalent bubble diameter (m).

The bubble size in the departing region can be written in the non-dimensional form in terms of the orifice size (Equation 5-3):

$$\beta_b = \frac{d_{32}}{d_o}, \qquad (5\text{-}3)$$

where: β_b is the dimensionless bubble diameter (or the bubble orifice ratio) and d_o is the orifice diameter (m).

5.3.2. Bubble velocity/ Bubble Reynolds number

In the departing region of the scrubber flow, bubbles leave the orifice and travel upward towards the liquid surface. Bubble velocity increased with time (Figure 5-11) due to the high effect of the pressure force. Also, bubble shapes changed continuously. The bubble velocity was affected by continuous changes of its shape because bubble velocity depended strongly on bubble shape (Quinn et al. 2014). After that, the effect of liquid circulation was increased due to turbulence and interaction with other bubbles. Therefore, the bubble started moving in both x-direction and z-direction also.

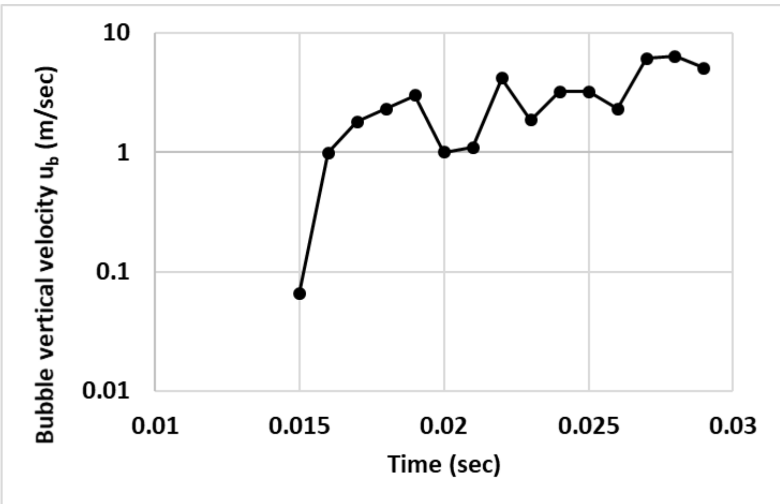

Figure (5-11). Variation of bubble vertical velocity with time.

The bubble vertical velocity (u_b) was obtained by calculating the change in y-position of the bubble centroid for a period of time. This process was applied for 70+ different bubbles at least within region 1 in different image frames using the *ImageJ* software for each test. Then, the bubble velocity was calculated from Equation (5-4) (Abdulwahid et al. 2018b):

$$u_i = \frac{Y_{i2} - Y_{i1}}{t_i}, \tag{5-4}$$

where: u_i is the bubble vertical velocity (m/s), Y_{i2}, Y_{i1} are the bubble y-positions in the image frames 2 and 1 respectively (m) and t_i is the bubble travelling time from Y_{i1} to Y_{i2} (sec.).

The average bubble velocity u_b of these bubbles was calculated using Equation (5-5). More importantly, bubble velocity was calculated only for the departing region to avoid mixing with other bubbles generated from the bubbles breaking up.

$$u_b = \frac{\sum_{i=1}^{i=N} u_i}{N} \tag{5-5}$$

This relationship can be expressed in the non-dimensional form as a bubble Reynolds number, which differs from the inlet gas Reynolds number:

$$Re_b = \frac{u_b d_{32} \rho_b}{\mu_b}, \tag{5-6}$$

where: ρ_b is the gas-phase density (kg/m^3) and μ_b is the dynamic viscosity of the gas phase (N.s/m^2).

5.3.3. Bubble heat transfer

The fundamental physical laws that govern bubble motion and their heat transfer to the surrounding fluid are the first law of thermodynamics, Newton's second law and the principle of mass conservation (Clift et al. 1978). The external fluid field deforms the bubble and deformed until the normal stress equals the shear stress at the fluid-fluid interface (Clift et al. 1978). The unsteady bubble motion causes a complex prediction of the heat transfer rate from the bubble (Harris et al. 2004). Moreover, the inlet gas faced the liquid at the pipe exit, and the temperature of the upward bubbles reduce continuously with the liquid height as a result of changing their surface area and temperature difference. This reduction in bubble temperature continues until reaching the outlet gas temperature when bubbles burst at the liquid surface (Figure 5-12).

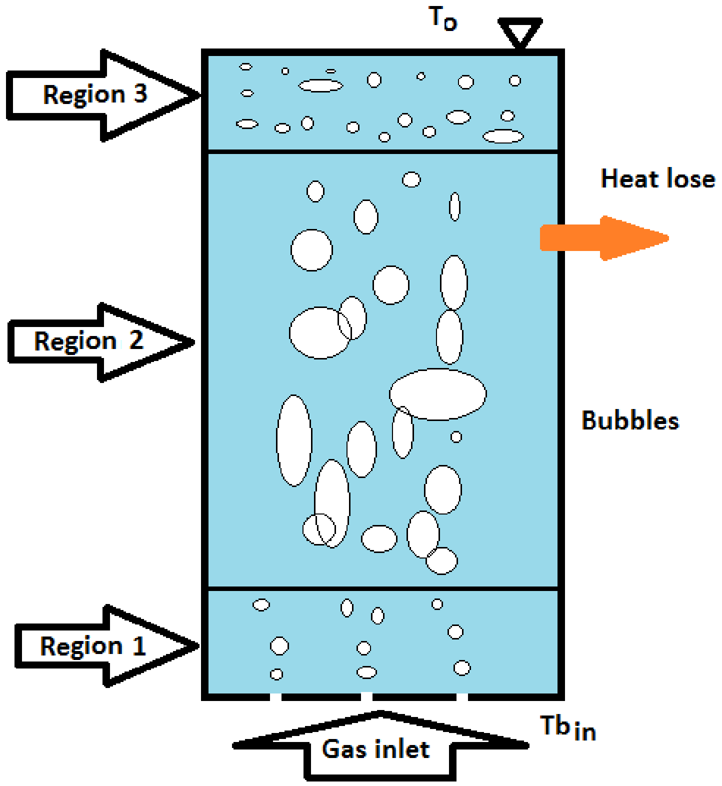

Figure (5-12). The reduction of bubble temperature.

The relationship between the bubbles and their position is very complex because the bubbles might lose some of their heat in the x-direction more than in the y-direction at a certain height. And the reverse may occur at another position after a while. To simplify the calculation, it was assumed that the bubble temperature changed linearly with its y-position only (Equation 5-7). Therefore, the bubble temperature can be calculated at the borders of the three regions of the flow using Equation (5-7).

$$T_{bin1,2,3} = T_{in2} - \frac{y_{1,2,3}}{h}(T_{in2} - T_o), \quad (5\text{-}7)$$

where: T_{bin} is bubble temperature at the inlet boundary of the region (K), T_{in2} is the inlet gas temperature at the pipe outlet (K), T_o is the leaving liquid bubble temperature (K), h is the total liquid height (m), and y is the bubble y-location (m).

The heat transferred from the gas-phase to the liquid phase can be calculated from Equation (5-8) (Abdulwahid et al. 2018b). This equation was used to calculate the heat transfer for each region separately.

$$Q_{1,2,3} = \dot{m_g} c_{pg} \Delta T_{1,2,3}, \tag{5-8}$$

where: $Q_{1,2,3}$ is the heat transfer from the gas to the liquid for any region 1, 2, or 3 respectively (W), $\dot{m_g}$ is the gas mass flow rate (kg/sec.), c_{pg} is the gas thermal capacity (kJ/kg.K) and $\Delta T_{1,2,3}$ is the temperature difference at the boundary of that region 1, 2, or 3 respectively (K).

Hart (1976) explained that the heat transfer coefficient was independent of several parameters such as the liquid height, the column diameter and the bubble location within the liquid. Therefore, in this investigation we will assume it is independent of the liquid height, diameter and location within the region because we have a different flow for each region. In this case, we have three values for the heat transfer coefficient representing three flow regions. The heat loss from the gas phase was totally transferred to the liquid phase (Abdulwahid et al. 2018). Due to the assumption that there is no phase change, the heat transfer rate can be expressed as shown in Equation (5-9). This equation was used to calculate the heat transfer coefficient in regions 1 and 2 only because there were no bubbles overlapping.

$$Q_{1,2,3} = h_{1,2,3}\, A_{b1,2,3}\left(T_{b1,2,3} - T_L\right), \tag{5-9}$$

where: $h_{1,2,3}$ is the heat transfer coefficient between the bubbles and their surrounding liquid (W/m^2.K), $A_{b1,2,3}$ is the total surface area of all bubbles with the flow region 1,2,3 (m^2), $T_{b1,2,3}$ is the average bubble temperature of the flow region (K) and T_L is the liquid temperature (K).

The heat transfer coefficient between bubbles and their surrounding liquid for region 2 was calculated based on the assumption of the linear change with vertical liquid height. By combining Equations (5-8) and (5-9) for region 2, we can estimate the total surface area of the bubbles. This surface area was compared with corresponding areas from *ImageJ* software to find the bubbles overlapping percentage in region 2. After that, the average heat transfer coefficient between the bubbles and their surrounding liquid can be obtained using Equation (5-10) for all of the flow regions. This average heat transfer coefficient is essential for Nusselt number (Nu) calculation. This calculation depends on the bubble characteristic length. The Sauter mean diameter of the bubbles at the departing region was considered as the characteristic length to eliminate the turbulence effect.

$$h_{ave} = \frac{\mathrm{h}_1 + \mathrm{h}_2 + \mathrm{h}_3}{3} \tag{5-10}$$

The Nusselt number represents the heat transfer from the bubbles to their surrounding in the non-dimensional form. This Nusselt number was calculated from Equation (5-11):

$$\mathrm{Nu} = \frac{h_{ave} d_{32}}{k}, \tag{5-11}$$

where: k is the bubble (gas) thermal conductivity (W/m.K).

5.3.4. Mother to daughter bubbles ratio

Bubbles left the orifices at the departing region and travelled upward with a curtain total number of bubbles based on the inlet gas Reynolds number. The number of these bubbles changed after passing the churn-turbulent region due to coalescing, breaking and overlapping. The bubbly region included these bubbles in addition to the smaller number of bubbles due to flow circulation (Figure 5-13).

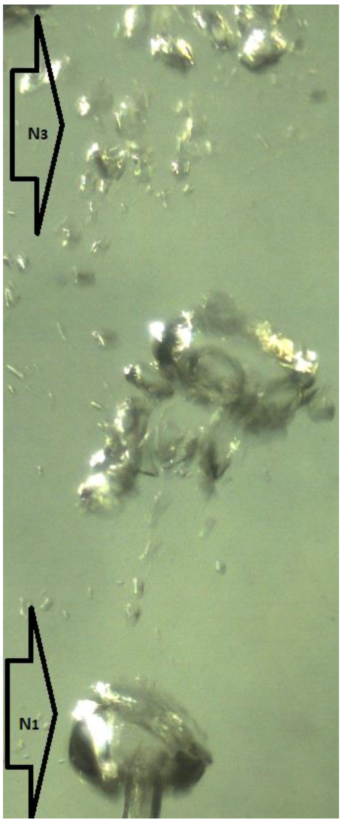

Figure (5-13). The relation between the bubbles number at Re 1,200.

The mother-to-daughter bubbles ratio (λ) may indicate the energy transfers between the bubbles and the liquid. A large number of bubbles generally have a larger total surface area than a limited number of bubbles. The number of bubbles was obtained directly from *ImageJ* software by analysing the *avi* video file. This ratio will be used instead of the breakage frequency (Maab & Kraume 2011, Solsvik et al. 2017, Hasan 2017) of the mother bubbles to the daughter bubbles or the breakage probability or efficiency (Luo & Svendsen 1996). It is very complex to recognise the break-up time of these bubbles in a high-turbulence flow of the scrubber.

$$\lambda = \frac{\sum N_1}{\sum N_3} \tag{5-12}$$

5.3.5. Bubble circularity

Bubble circularity measures how much the bubble shape approaches a perfect sphere. This parameter was obtained directly by analysing the *avi*. file using the *ImageJ* software. Bubbles were assumed earlier in this chapter to have spherical shapes in the three-dimensional analysis or to be circular in the two-dimensional case. Therefore, this may cause some errors in our calculations if it is far from this assumption. However, it is very complex to avoid this error because the bubble shape changes continuously with time and position. Further investigations are discussed later in this chapter.

5.4. Results and Discussion

Different operating conditions and/ or design parameters may influence the heat transfer rate and the flow of the scrubber. The departing region (region 1) will be the focus of most investigations of the scrubber in this chapter to eliminate the turbulence effect.

5.4.1. The effect of orifice ratio (β)

The orifice plate played an important and positive role in the scrubber performance. It reduced both the flow turbulence and the liquid carried by the outlet gas. Each orifice was affected by three or four adjacent orifices in the same row due to inertia and pressure forces (Shuyi 2003). These forces affected the investigated parameters such as bubble size, shape and velocity (Figure 5-14). This section investigates the individual effect of the orifice ratio on several parameters. Three orifice ratios were studied: 0.1, 0.15 and 0.2. Also, the liquid temperature, the inlet gas Reynolds number and the temperature ratio were maintained constant at $20^{\circ}C$, 1,200 and 1, respectively during these experiments to eliminate their effect. The following correlations in this section are suitable for the operating conditions mentioned earlier. However, they may be applicable for other ranges of operating conditions.

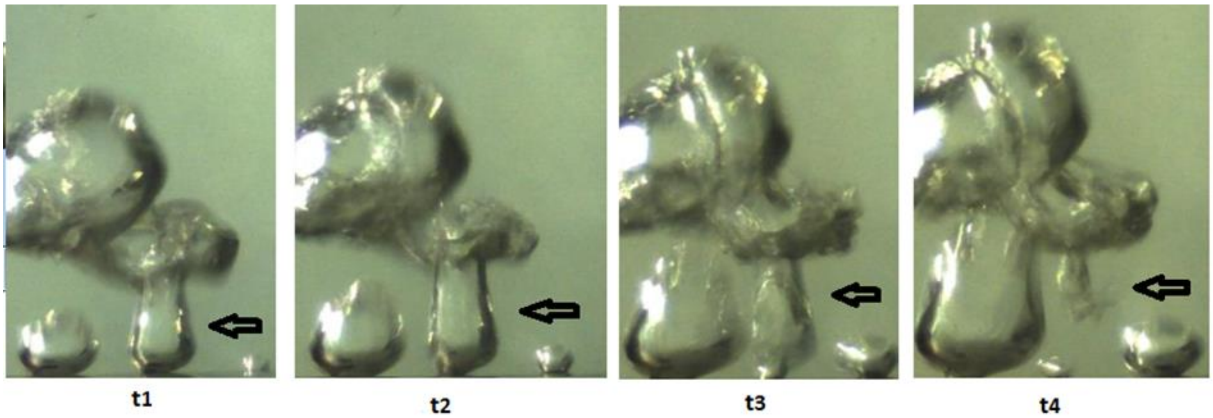

Figure (5-14). The influence of orifices by each other at Re 1,200 with equal time periods between each image.

5.4.1.1. Bubble size

Bubble size at the departing region was strongly affected by the orifice ratio. In this section, the orifice size effect was investigated without involving heat transfer to eliminate any additional parameter possibility on the flow characteristics. In other words, the gas was supplied at the same temperature as the liquid. The bubble size was calculated using Equation (5-2). Moreover, the Sauter mean diameters (d_{32}) for the bubbles in the departing region were found to be 19.4, 18.9 and 19 mm for β 0.2, 0.15 and 0.1, respectively. This means that bubbles were affected by turbulence forces only despite the differences in their departing diameters at the orifice. This agrees with Davidson and Schüler (1997) who suggested that bubble size was not a function of the orifice size only.

5.4.1.2. Bubble motion

The vertical velocity of the bubble at region 1 was dependent on the orifice size (Figure 5-15). The vertical bubble velocity decreased with increasing the orifice size. This can be explained easily using the continuity equation. To maintain the same mass flow rate of the inlet gas, the increment in the orifice cross-sectional area must be correspond to a reduction in the bubble velocity. When the volume of the bubble increases, the buoyancy effect becomes more important (Simmons et al. 2015). *ImageJ* provided the changes in bubble position in the y-direction in the departing region and the time of image frames. The vertical velocity of these babbles was calculated using Equation (5-4). After, that the average vertical velocity of the bubbles in the departing region was obtained by dividing the sum of their velocity on their number at this region. A new correlation between the orifice diameter and the bubble velocity can be confirmed from Figure (5-15) as follows:

$$u_b = 1.75 - 81.5\, d_o \tag{5-13}$$

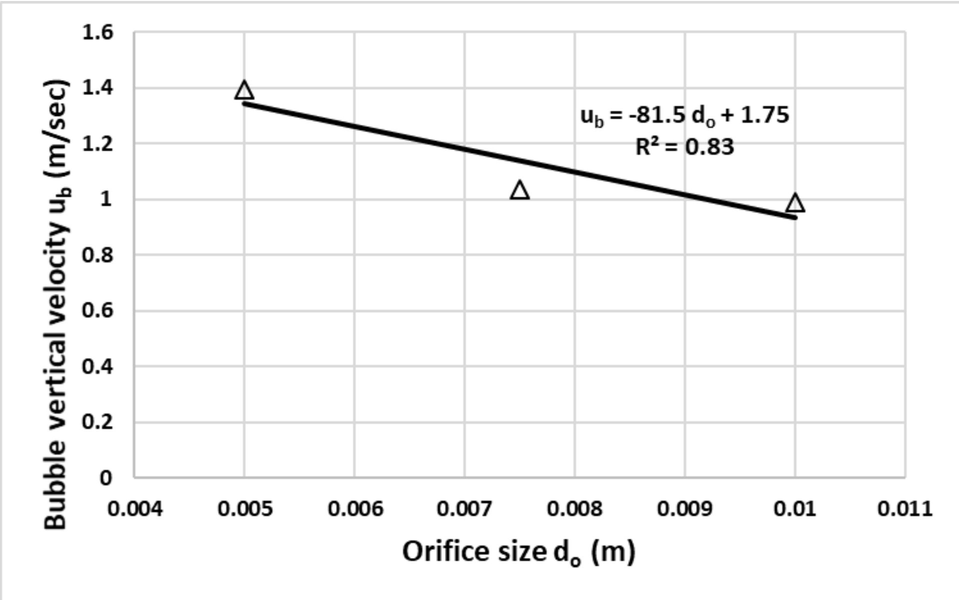

Figure (5-15). Dependency of bubble velocity of the departing region on the orifice size.

To convert the previous vertical velocity correlation with the orifice diameter into the non-dimensional form, both Re_b and β were used instead of u_b and d_o respectively (Figure 5-16 and Equation 5-14). The orifice ratio and the bubble Reynolds number were calculated using Equations (4-2) and (5-6) respectively. These correlations are suitable for the departing region at inlet gas Reynolds number 1,200.

$$Re_b = 2{,}296 - 5{,}165\, \beta \tag{5-14}$$

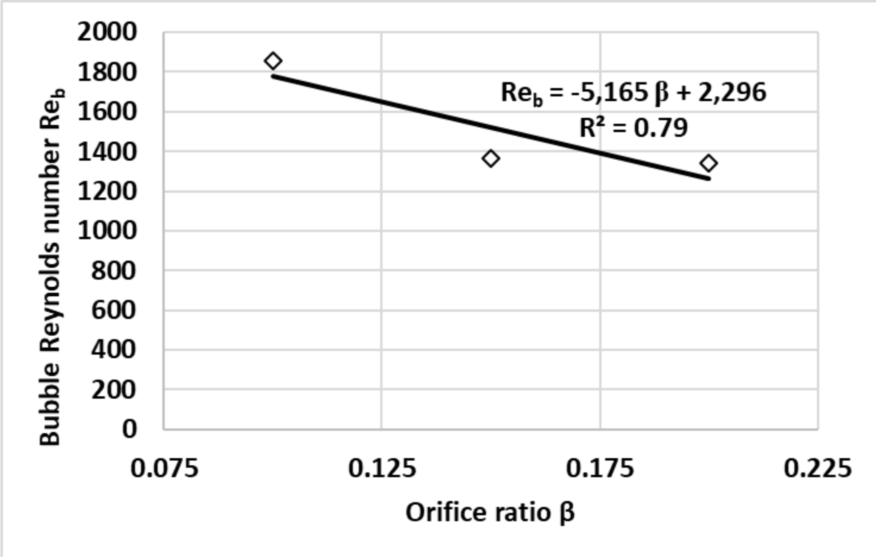

Figure (5-16). The relation between the bubble Reynolds number and the orifice ratio at the departing region.

In the departing region, the non-dimensional bubble diameter ratio (β_b) increased with increasing the bubble Reynolds number (Figure 5-17 and Equation 5-15). The bubble Reynolds number was affected by the orifice ratio as mentioned earlier. This increased the bubble ratio because the bubble Sauter mean diameter was nearly constant during these tests.

$$\beta_b = 5.04 \ln Re_b - 34.1 \qquad (5\text{-}15)$$

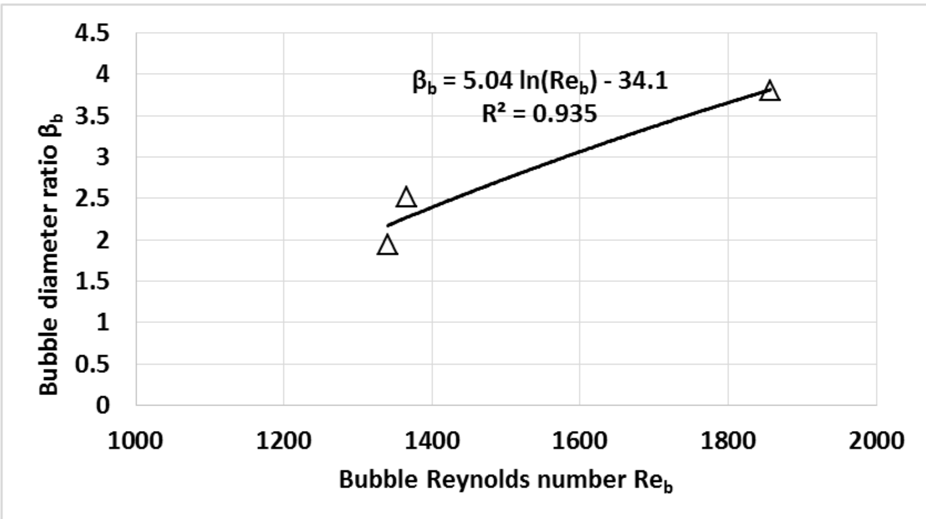

Figure (5-17). The relation between Reynolds number and the bubble diameter ratio at the departing region.

5.4.1.3. Breaking ratio

The number of bubbles in both departing and bubbly regions increased as a result of reducing the orifice ratio (Table 5-3). The number of bubbles was increased due to reducing the orifice size to maintain the same inlet gas mass flow rate. This bubble breaking ratio was obtained using Equation (5-12) by dividing the number of parent bubbles by the number of daughter bubbles. Both of these numbers were provided by *ImageJ* software after analysing the related videos.

Table (5-3). Bubble braking ratio for different orifice ratios

Orifice ratio (β)	0.15	0.1	0.2
The bubble rate of departing region (bubble/sec)	57	43	38
The bubble rate of bubbly region (bubble/sec)	152	126	114

The bubble breaking ratio decreased linearly with the orifice ratio increment (Equation 5-16 and Figure 5-18). This agrees with Islam et al. (2015) who confirmed that bigger and faster coalescence of bubbles can be achieved using larger orifice diameter. This fast coalescence rate reduces the number of bubbles at the bubbly region for a given inlet gas flow rate. Applying Equation (5-12) confirmed that this breaking ratio decreased with increasing the orifice size.

$$\lambda = 0.4 - 0.44\,\beta \qquad (5\text{-}16)$$

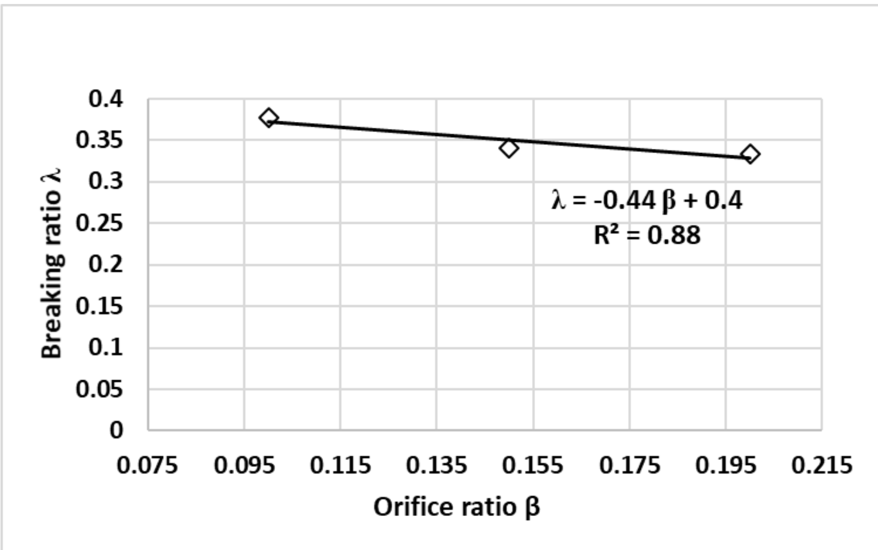

Figure (5-18). The relation between the bubbles breaking ratio and the orifice ratio.

5.4.1.4. Bubble circularity

The average bubble circularity in the departing region was obtained directly from the *ImageJ* software. At the inlet gas Reynolds number 1,200 and the temperature ratio 1, they were 0.85, 0.26 and 0.32 for β equal to 0.2, 0.15 and 0.1, respectively. This means that bubble circularity was independent of the orifice ratio in contrast to the bubbles at the detachment place. Indeed, the average circularity of all bubbles at the departing region was led by other parameters such as flow turbulence.

5.4.2. The effect of inlet gas Reynolds number (Re)

The inlet gas Reynolds number has a major effect on the flow dynamics and the heat transfer as mentioned previously in the literature. This section investigates the effect of the inlet gas Reynolds number individually on the bubble hydro-dynamically. Four inlet gas Reynolds numbers of 1,200, 1,800, 2,400 and 3,300 were studied. The 3,300 Reynolds number was highly complex in image analysis due to overlapping bubbles. Therefore, this section ignores this test. In addition, the inlet gas temperature ratio, the liquid temperature and the orifice ratio were maintained constant at 1, 20°C and 0.1, respectively during these experiments to eliminate their effect on this investigation. The following correlations in this section are suitable for the operating condition mentioned earlier. However, they might be applicable for other ranges of operating conditions. The effect of inlet gas Reynolds number was investigated and discussed.

5.4.2.1. Bubble size

Increasing the inlet gas Reynolds number caused more turbulence, and the departing bubbles were affected strongly by this turbulence. This can be confirmed clearly from Figure (5-19). This figure shows that the bubble Sauter mean diameter (d_{32}) has different values based on the inlet gas volumetric flow rate. This diameter decreased with increasing the inlet gas flow rate because the bubble growth was limited due to increasing bubble overlapping and/or coalescing. The higher inlet gas Reynolds number represents the most complex images and videos analysis (Figure 3-19). The case of Re 3,300 cannot be analysed due to high bubble overlapping. To find the relationship between the Sauter mean diameter and the inlet gas volumetric flow rate more tests must be conducted.

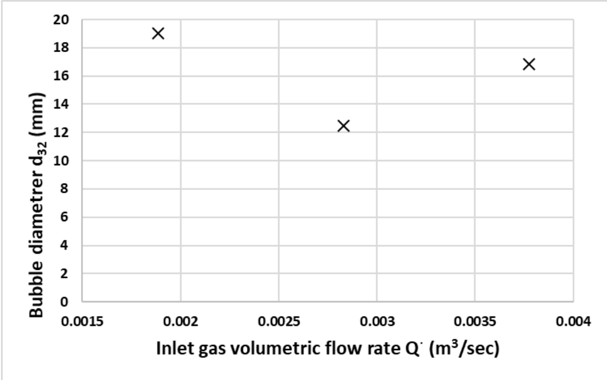

Figure (5-19). The relationship between the bubble diameter and the inlet gas volumetric flow rate.

The previous equation can be represented in terms of the inlet gas Reynolds number instead of the inlet gas volumetric flow rate (Figure 5-20). This relationship is polynomial for two reasons. Firstly, the departing bubbles were affected continuously by each other (Islam et al. 2015). Secondly, some error occurred with video analysis using the *ImageJ* software after removing the noise and setting the threshold because this threshold did not cover all the bubble projected area due to the bubbles overlapping. The relationship between the bubble diameter ratio at the departing region and the inlet gas Reynolds number is shown in Equation (5-17). The figure shows that bubble diameter ratio first decreases and then increase with the increase of the Reynolds number. The perfect R-squared number (R^2=1) for the fitting function is due the limitation of the data points (same with the subsequent graphs). In future research more test conditions should be performed.

$$\beta_b = 3(10)^{-6}\, Re^2 - 0.011\, Re + 13 \tag{5-17}$$

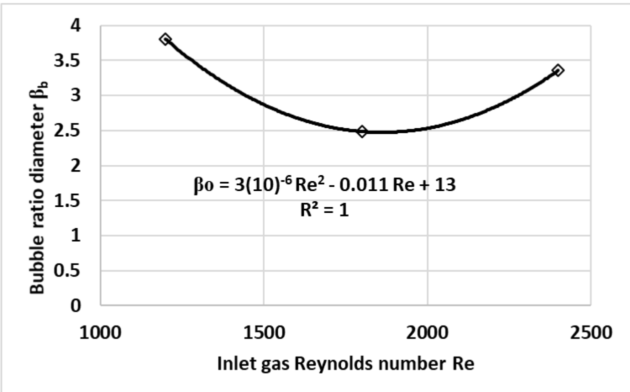

Figure (5-20). The relationship between the bubble diameter and the inlet gas Reynolds number.

5.4.2.2. Bubble motion

Bubble average vertical velocity in the departing region increased with an increasing inlet gas Reynolds number as expected until 1,800 (Figure 5-21). However, it decreased when the inlet gas Reynolds number exceed 1,800 as a result of decreasing the bubble size as explained earlier. Indeed, increasing the inlet gas Reynolds number increased the churn-turbulent region. In other words, fewer were analysed using *ImageJ* due to difficulty monitoring the bubbles. Moreover, the overall relationship between bubble velocity and the inlet gas Reynolds number can be expressed as:

$$u_b = -4(10)^{-7}\, Re^2 + 0.0011\, Re + 0.55 \tag{5-18}$$

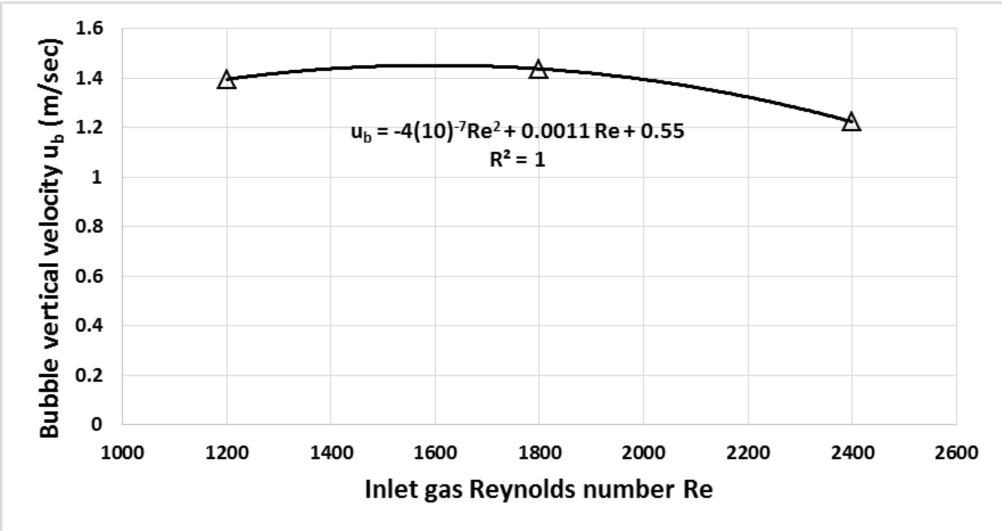

Figure (5-21). The relationship between the bubble velocity and the inlet gas Reynolds number.

This relationship can be expressed in a non-dimensional form (Equation 5-19 and Figure 5-22). Figure (5-22) shows that with the increase of inlet gas Reynolds number, the bubble Reynolds number first decreases and then increases.

$$Re_b = 0.0011\, Re^2 - 4\, Re + 5{,}460 \tag{5-19}$$

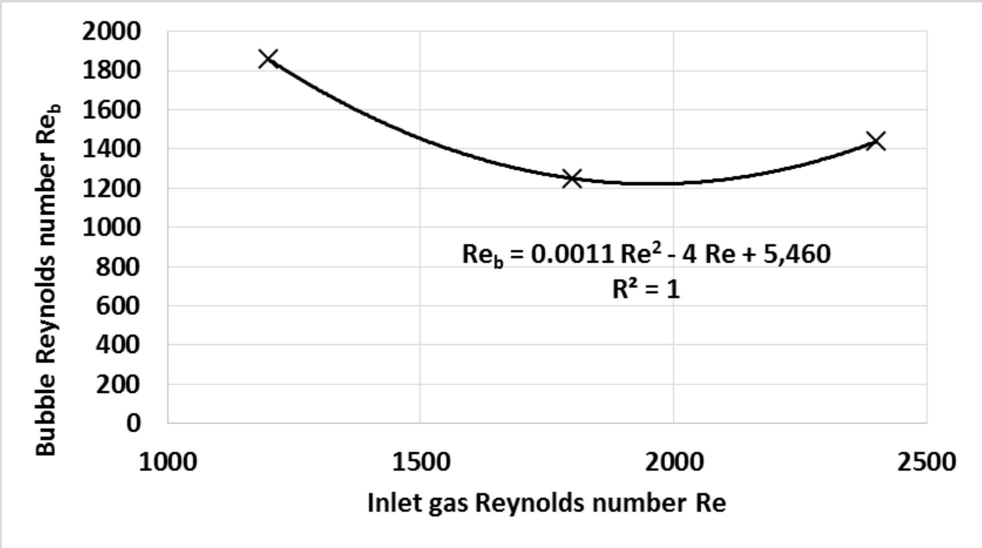

Figure (5-22). The relationship between the Reynolds numbers of the bubble and the inlet gas.

5.4.2.3. Breaking ratio

Breaking ratio depended strongly on the inlet gas Reynolds number (Figure 5-23 and Equation 5-20). It increased with increasing the inlet gas Reynolds number. Higher turbulence was observed clearly at the higher Reynolds number of the inlet gas. The number of bubbles at the bubbly region was fewer than at the departing region (Table 5-4). This is due to increasing the bubble coalescing in the bubbly region (Figure 5-24). In addition to the difficulties in both of images and videos analysis of the higher Reynolds number, this increases the error in these results.

$$\lambda = -5\,(10)^{-6} Re^2 + 0.0215\, Re - 17.5 \qquad (5\text{-}20)$$

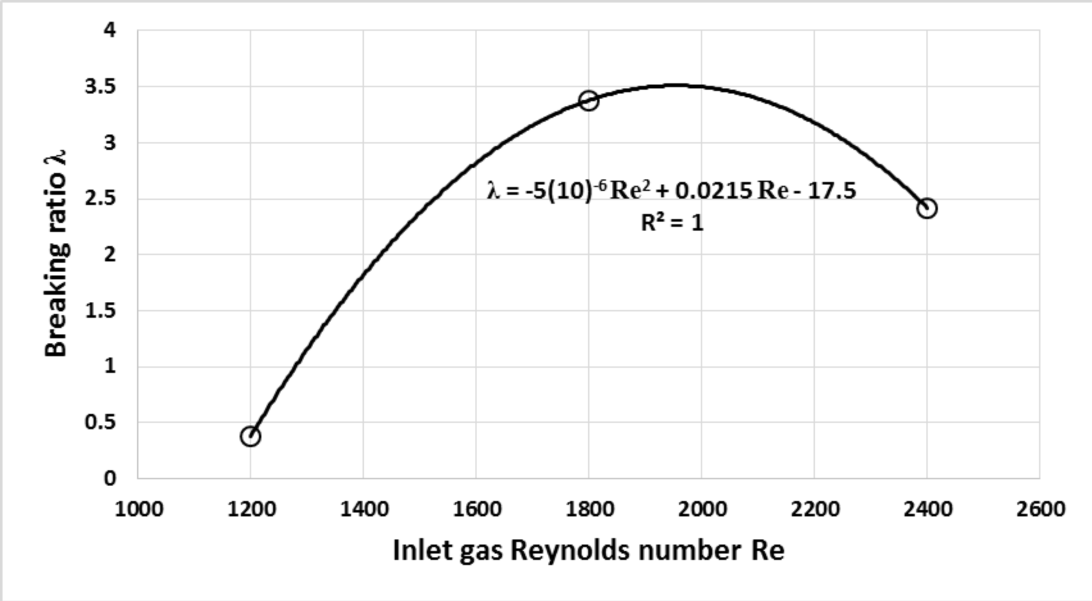

Figure (5-23). Dependency of bubble breaking ration on Reynolds number of the inlet gas.

Increasing the inlet gas Reynolds number increased the number of bubbles in region 1. This was a result of increasing the gas volume flow rate into the same orifice size. However, the number of bubbles at the bubbly region was strongly affected by the flow turbulence, in particular, the bubbles coalescing and/or overlapping.

Table (5-4). Bubble numbers for different inlet gas Reynolds numbers.

Inlet gas Reynolds number	**1,200**	**1,800**	**2,400**
The bubble rate of departing region (bubble/sec)	57	115	117
The bubble rate of bubbly region (bubble/sec)	152	34	48

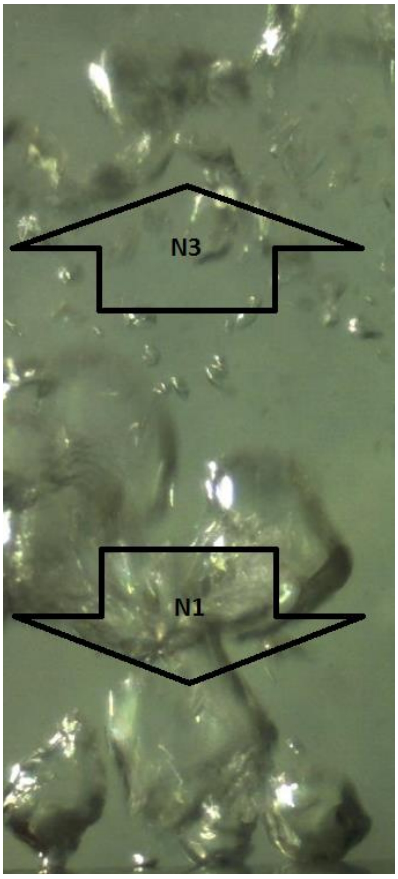

Figure (5-24). Bubble coalescing percentage at the bubbly region.

5.4.2.4. Bubble circularity

The average bubble circularity in the departing region decreased moderately and linearly with increasing bubble Reynolds numbers (Figure 5-25). Bubbles were initially generated with a non-uniform shape at higher rates of the continuous change of their shapes due to more interaction between bubbles at a higher bubble Reynolds number. The bubble circularity in terms of bubble Reynolds number is described in Equation (5-21).

$$C_b = 0.5 - 9(10)^{-5} Re_b \tag{5-21}$$

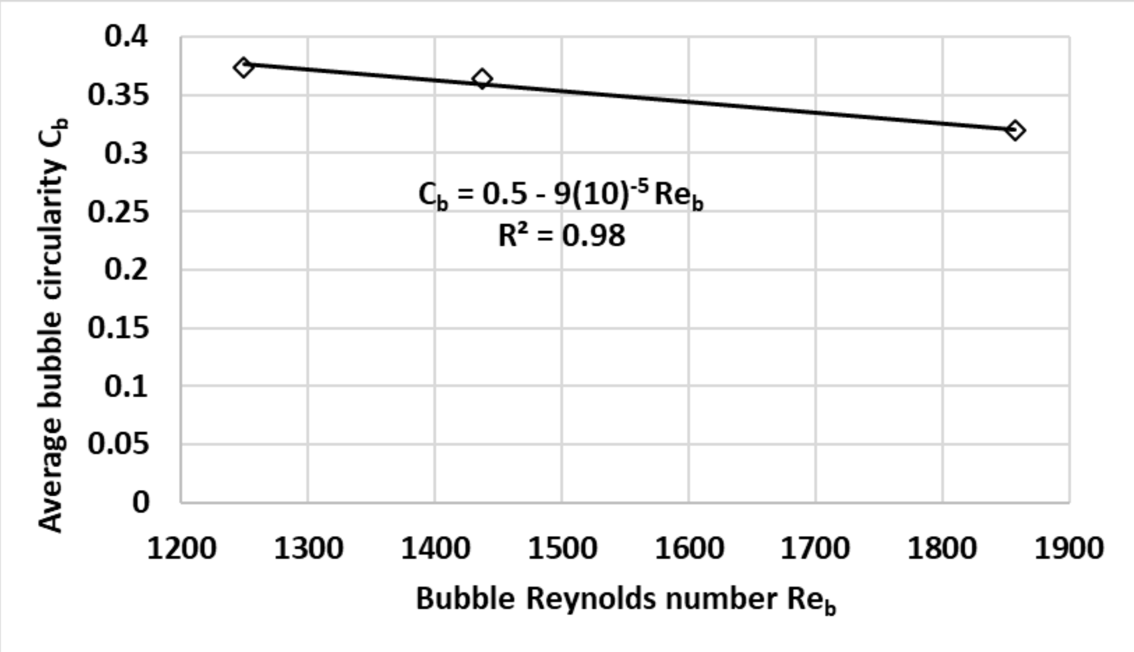

Figure (5-25). Dependency of bubble circularity on the bubble Reynolds number.

5.4.3. The effect of inlet gas temperature ratio (θ)

The effect of increasing the inlet gas temperature ratio on scrubber performance was investigated at a constant liquid temperature of 20°C. Both the inlet gas Reynolds number and the orifice ratio were maintained constant at 1,200 and 0.1 respectively during these experiments to eliminate their effect on this investigation. Four operating conditions were started directly after each other to avoid any possible effect of changing the liquid temperature because of the heat gain from the inlet gas. This section investigates the four inlet gas temperature ratios of 1.3, 2, 2.6 and 3 on the bubble characteristics hydro-dynamically and thermally. The following correlations in this section are suitable for the operating condition mentioned earlier. However, they might be applicable for other ranges of operating conditions.

5.4.3.1. Bubble size

The average bubble size in region 1 was independent of changing the inlet gas temperature. Although bubble density was changed due to the gas temperature effect, the influence of turbulence was stronger than increasing the bubble temperature. The Sauter mean diameters were calculated at 15mm, 18mm, 20mm and 17mm corresponding to the inlet gas temperature ratios of 1.3, 2, 2.6 and 3, respectively. These results were achieved at a constant orifice ratio of 0.1 and constant inlet gas Reynolds number of 1,200.

5.4.3.2. Bubble motion

The average vertical bubble velocity in the departing region increased with increasing the inlet gas temperature (Figure 5-26 and Equation 5-22). This agrees with Tian et al. (2019) and Zhang et al. (2003). Increasing the temperature inside the bubble reduces the bubble density. This decreases the gravity force and pushes the bubble upward. Tian et al. (2019) suggest the bubble rising velocity is affected also by the liquid viscosity in addition to bubble surface properties.

$$u_b = 2(10)^{-7}T_{in}^2 - 1(10)^{-5}T_{in} + 0.103 \qquad (5\text{-}22)$$

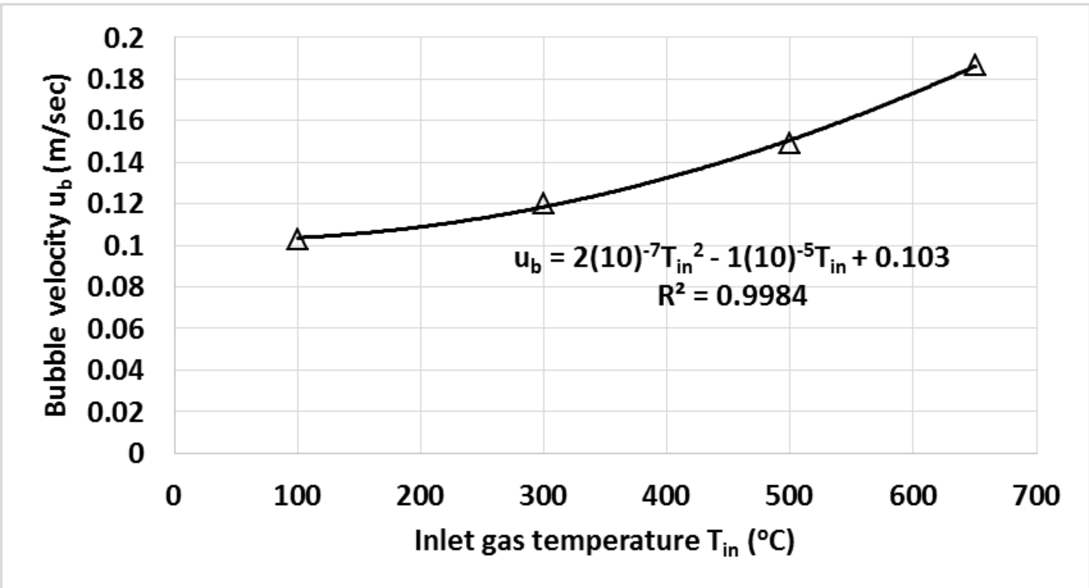

Figure (5-26). The relationship between the average bubble vertical velocity and the inlet gas temperature.

Equation (5-23) can be written in non-dimensional form as bubble Reynolds number and inlet gas temperature ratio instead of bubble vertical velocity and inlet gas temperature (Equation 5-23 and Figure 5-27). The bubble Reynolds number depends on both bubble diameter and velocity. This causes a difference in the correlation slope between Figures (5-26) and (5-27).

$$Re_b = -17\theta^2 + 75\theta - 31 \qquad (5\text{-}23)$$

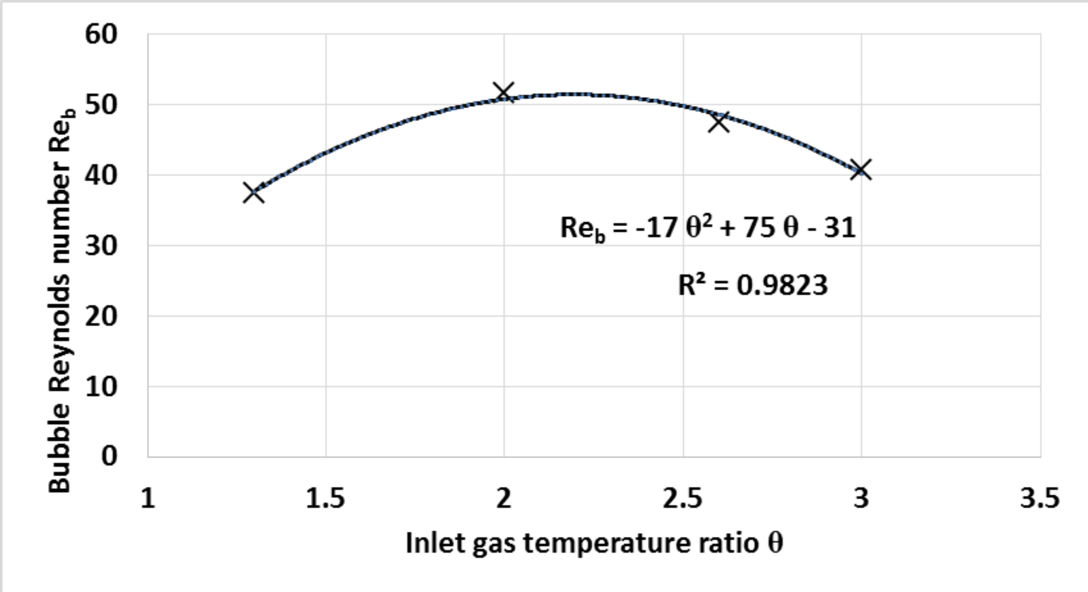

Figure (5-27). The relationship between the bubble Reynolds number and the inlet gas temperature ratio.

5.4.3.3. Breaking ratio

The bubble breaking ratio was independent of increasing the inlet gas temperature as shown in Table (5-5). The breaking ratio was influenced by the flow turbulence rather than the bubble temperature.

Table (5-5). The bubble breaking ratio at different inlet gas temperature ratios.

Inlet gas temperature ratio (θ)	**1.3**	**2**	**2.6**	**3**
Breaking ratio (λ)	0.24	0.3	0.24	0.38

5.4.3.4. Bubble circularity

Bubble circularity was independent of the inlet gas temperature ratio (Table 5-6). This was due to the same reason explained earlier (Table 5-5).

Table (5-6). Bubble circularity at different inlet gas temperature ratio.

Inlet gas temperature ratio (θ)	**1.3**	**2**	**2.6**	**3**
Bubble circularity (C_b)	0.26	0.29	0.29	0.3

5.4.3.5. Bubble heat transfer

The heat transfer to the liquid increased by increasing the inlet gas temperature based on Equation (5-8). This was due to increasing the temperature difference between the bubbles and their surrounds. Most of the inlet gas energy was transferred to the liquid. The minority of the inlet energy leaves the scrubber with the outlet gas. There was no evaporation due to the process being quick. The heat transfer for each flow region was calculated based on Equation (5-7) in addition to Equation (5-8) as shown in Table (5-7). This table confirmed that the heat transfer increased for all flow regions. The churn-turbulent region had the most heat transfer because it had the larger volume, temperature difference and flow turbulence.

Table (5-7). The heat transfer between the gas and the liquid at different inlet gas temperature ratios.

Inlet gas temperature ratio (θ)	**1.3**	**2**	**2.6**	**3**
Heat transfer at the departing region (Q_1) (W)	44	68	93	112
Heat transfer at the churn-turbulent region (Q_2) (W)	89	319	565	757
Heat transfer at the bubbly region (Q_3) (W)	45	159	282	378
Total heat transfer (Q) (W)	178	546	940	1248

The heat transfer coefficient between the bubbles and their surrounding liquid was obtained using Equation (5-9) for both departing and bubbly regions. The heat transfer coefficient of the churn-turbulent region was calculated by assuming a linear relationship of the heat transfer coefficient for all the flow region (Table 5-8). After that, the average heat transfer for the flow inside the scrubber was obtained using Equation (5-10).

Table (5-8). The heat transfer coefficient between the gas bubble and the surrounding liquid at different inlet gas temperature ratios.

Inlet gas temperature ratio (θ)	**1.3**	**2**	**2.6**	**3**
Heat transfer coefficient at the departing region (h_1) ($W/m^2.K$)	37	22	12	16
Heat transfer coefficient at the churn-turbulent region (h_2) ($W/m^2.K$)	276	152	100	150
Heat transfer coefficient at the bubbly region (h_3) ($W/m^2.K$)	513	282	187	283
Average heat transfer coefficient for the flow regions (h_{ave}) ($W/m^2.K$)	276	152	100	150

The relationship between the average heat transfer coefficients and the inlet gas temperatures is shown in Figure (5-28) and Equation (5-24). This figure shows that the heat transfer coefficient increased with increasing the inlet gas temperature. Increasing both the inlet gas energy and the temperature difference caused this increment due to the effect on the gas thermal properties.

$$h_{ave} = 9(10)^{-4}\, T_{in}{}^{2} - 0.33\, T_{in} + 128.5 \tag{5-24}$$

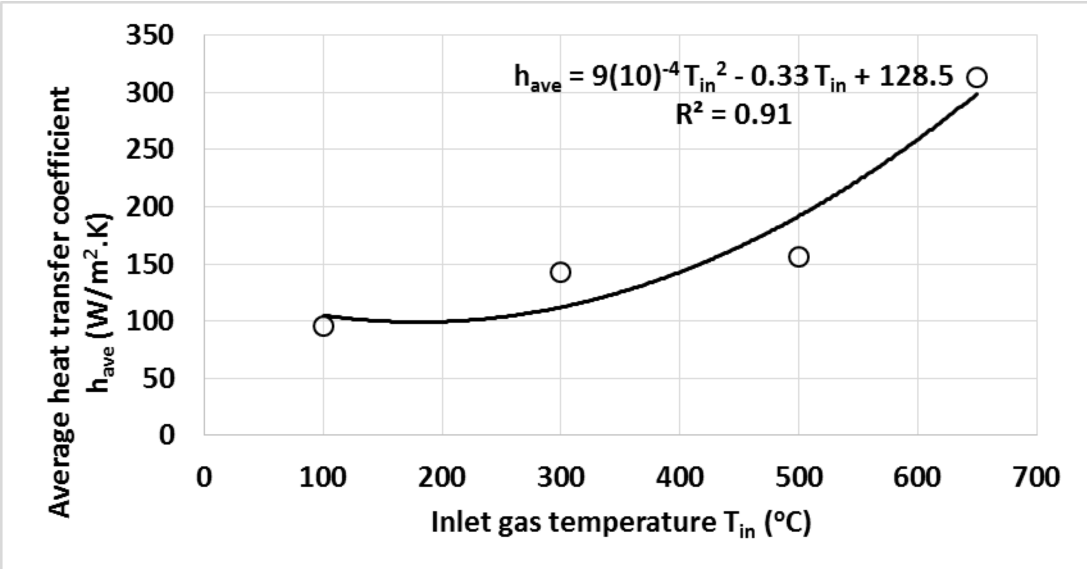

Figure (5-28). The relationship between average bubble heat transfer coefficient and inlet gas temperature.

The heat transfer coefficient between the bubbles and their surrounding depends on the bubble vertical velocity (Figure 5-29 and Equation 5-25). This agrees with Fair et al. (1962) and Harris et al. (2004). The high turbulence flow produces the high rates of energy as a result of the strong local interaction between the bubbles and their surrounding liquid (Abdulmouti 2014).

$$h_{ave} = 26{,}392\, u_b^2 - 5{,}229 u_b + 366 \tag{5-25}$$

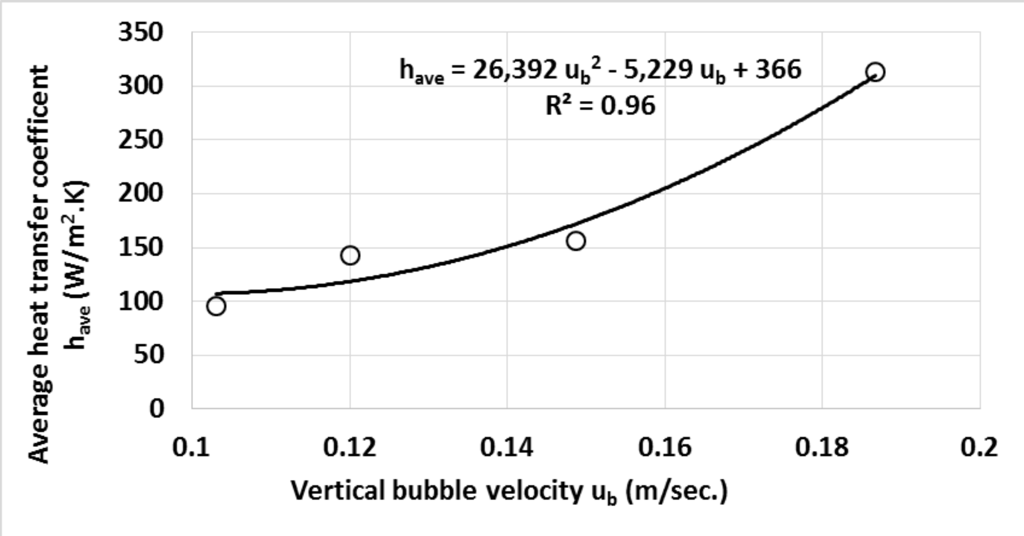

Figure (5-29). Heat transfer coefficient as a function of bubble vertical velocity.

The non-dimensional form of the relationship between the average heat transfer coefficient and the inlet gas temperature can be expressed in terms of the Nusselt number and the inlet gas temperature ratio. The calculated Nusselt number increased due to increasing the inlet gas temperature ratio (Figure 5-27 and Equation 5-26). This can be a result of the changes in the heat transfer coefficient and bubble velocity with temperature.

$$\mathrm{Nu}_b = 17\,\theta^2 - 49\,\theta + 82 \tag{5-26}$$

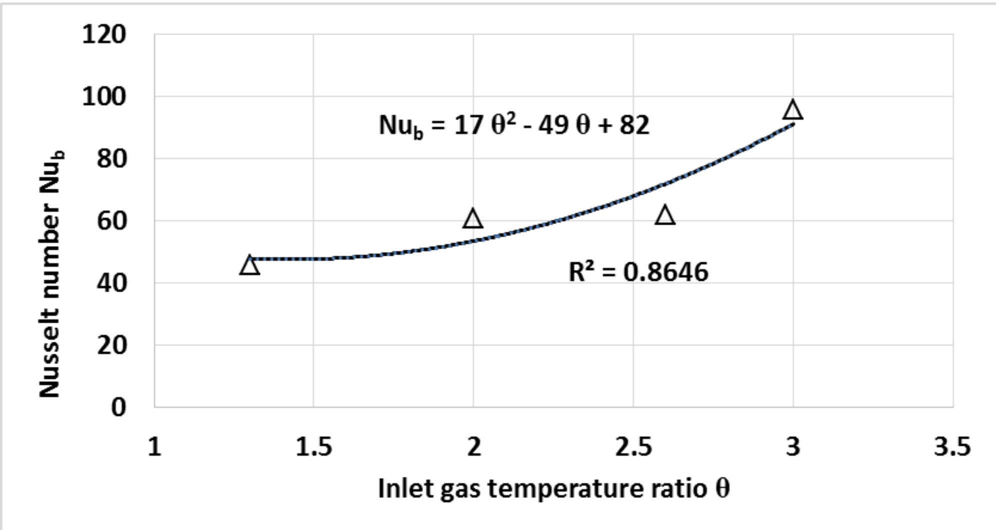

Figure (5-30). Bubble Nusselt number as a function of inlet gas temperature ratio.

5.4.3.6. Churn-turbulent overlapping

The churn-turbulent region had a high percentage of bubble overlap compared with the other two regions. To obtain this percentage, the total surface area of all bubbles within this region was calculated using Equation (5-9). Then, this area was compared with the total area from *ImageJ* software to find the bubble overlap percentage (Table 5-9). This overlapping percentage was independent of the inlet gas temperature ratio, which might cause some error in the heat transfer calculation. To avoid this error in the future, it is recommended to use at least two high-speed video systems to visualise the flow from different sides of the scrubber, and to build a new scrubber with all sides made from transparent high-temperature resistant polycarbonate metal. A careful consideration should be made to avoid another error because the heat transfer rate from the scrubber to the ambient will differ from the industrial one because of changing metal.

Table (5-9). Bubble overlap for different inlet gas temperature ratio.

Inlet gas temperature ratio (θ)	**1.3**	**2**	**2.6**	**3**
Bubbles overlapping of the churn-turbulent region (%)	39	56	52	100

5.5. Conclusion

This chapter has investigated the heat transfer model of the scrubber for different operating conditions in both dimensional and the non-dimensional forms, in particular, the inlet gas Reynolds number range 1,200~3,300 and temperature ratio 1~3 and the orifice ratio range 0.15-0.2. The raw data from Chapter 3 was used in this study. These investigations were achieved mainly depending on images and videos analysis using the *ImageJ* software. The importance of this analysis is to investigate the heat transfer within the scrubber. High heat transfer rates causes higher humidity and temperature of the outlet gas.

Three flow regions were observed in the scrubber: the departing, the churn-turbulent and the bubbly. The development of these regions depended on the inlet gas Reynolds number. Increasing the inlet gas Reynolds number reduced both the departing and the bubbly regions and increased the churn-turbulent one. The churn-turbulent region was the most complex because it contained a high percentage of bubble breaking, coalescing and overlap. This study confirmed that the bubble overlap percentage in this region can reach 100%.

Bubbles departed the orifice row at the departing region with different shapes, sizes and velocities. This was due to the effect of the adjacent orifices and the flow turbulence. Bubble size, vertical velocity and y-position increased with time until reaching the next flow region. At the departing region, it was confirmed that the bubble diameter was a function of the inlet gas volumetric flow rate or the Reynolds number. Both the inlet gas Reynolds numbers and temperatures in addition to the orifice sizes affected bubble vertical velocity or bubble Reynolds number at the departing region. Both the bubble diameter ratio and the bubble circularity were dependant on the bubble Reynolds number.

The bubble breaking ratio was a function of both the inlet gas Reynolds number and orifice ratio. The heat transfer between the gas bubbles and their surrounding liquid depended on the inlet gas temperature ratio. Finally, increasing the inlet gas Reynolds number and temperature ratio in addition to decreasing the orifice ratio would increase scrubber performance. This is because it would maximise the heat transfer rate by increasing the temperature difference, the interaction between bubbles and liquid, and the bubble surface area via the breaking ratio.

Chapter 6 – Conclusions and Recommendations for Future Work

6.1. Conclusions (Summary of Findings)

This thesis began by reviewing the particulate matter capturing mechanism, heat transfer mechanism and flow mechanism of a wet scrubber. The wet scrubber was analysed using three methods: experiments, thermodynamic analysis and heat transfer analysis. This included a wide range of operating conditions such as inlet gas flow rate, inlet gas temperature and liquid volume ratio and design parameters such as orifice size.

This thesis confirmed that increasing the inlet gas Reynolds number and temperature ratio in addition to decreasing the orifice ratio improved scrubber performance. This increment maximised the heat transfer rate by increasing the temperature difference, the interaction between bubbles and liquid, and the bubble surface area via the breaking ratio. Further summary of thesis findings are explained as followed based on chapters to simplify determining the related data, calculations,…etc.

6.1.1. Summary of experiments findings

The experiments confirmed that the wet scrubber effectively reduced the inlet gas temperature up to 590ºC. However, the outlet gas relative humidity increased up to the saturation condition for most tests due to the high evaporation rate of the scrubbing liquid. Adding the orifice plate reduced the flow turbulence and the liquid leaving the scrubber from the scrubber outlet. Also, bubbles left the orifices in a non-uniform stream. Bubbles departed the orifices from the inner rows more than the outer ones.

6.1.2. Summary of thermodynamic analysis findings

The scrubber was analysed thermodynamically based on the steady-state heating assumption, the first law of thermodynamics and the continuity equation. The heat loss from the scrubber was calculated based on the transient convection heat transfer. In this method, the liquid temperature had a major effect on the heat loss from the scrubber. Further, the results of this analysis confirmed that increasing the liquid volume ratio reduced the outlet gas temperature. Increasing the inlet gas Reynolds number and/or temperature ratio affected the scrubber performance. Also, there was fairly good agreement between the calculated and the measured relative humidity of the outlet gas.

6.1.3. Summary of thermodynamic analysis findings

The heat transfer analysis of the scrubber confirmed three flow regions at the low Reynolds numbers of the inlet gas. These regions were: departing, churn-turbulent and bubbly. The departing region had nearly the same height as the bubbly one. This height nearly equaled one-quarter of the total liquid height. About half of the liquid height was observed for the churn-turbulent region. The churn-turbulent region was the most complex one because it contained all bubble overlap, breaking and/or coalescing. The bubble overlap percentage in this region could reach 100%. However, at high Reynolds numbers of the inlet gas, only the churn-turbulent region was observed at high inlet gas flow rate from the orifice to the liquid surface.

Bubbles departed the orifice row at the departing region with different shapes, sizes and velocities. This was due to the effect of the adjacent orifices and the flow turbulence. Furthermore, the bubble diameter was a function of the inlet gas volumetric flow rate or the Reynolds number. The inlet gas Reynolds number, inlet gas temperature ratio and the orifice ratio affected the bubble vertical velocity or bubble Reynolds number at the departing region. Also, the bubble diameter ratio and the bubble circularity were dependent on the bubble Reynolds number. The bubble breaking ratio was a function of the inlet gas Reynolds number and the orifice ratio. The heat transfer between the bubbles and their surrounding liquid depended on the inlet gas temperature ratio.

6.2. Recommendations for Future Work

The results of the three methods could be improved by applying several modifications for the apparatus. First, the inlet gas condition should be measured for each test by installing the humidity probe and the thermocouple at the stream of the inlet gas. This would improve the estimation of the heat loss from the scrubber. As a second modification, at least two high-speed camera systems should be used in two different directions to reduce error in image analysis such as the bubble overlap.

Additional operating conditions could be tested following the same thesis procedure. For example, diesel exhaust gas could be used instead of the air tested in this thesis. Also, testing different scrubbing liquids could be fruitful in the case of testing the diesel exhaust gas.

6.3. Contribution to New Knowledge

Reducing the relative humidity and temperature of the outlet gas and the liquid drops carried out by the outlet gas indicate improving the scrubber performance. This can be achieved by suggesting a new scrubber design. The new scrubber design has two orifice plates to increase the heat transfer between the bubbles and the liquid (Figure 6-1). Adding these two orifices would prevent the leaving gas from carrying some liquid to the scrubber outside. This solves one problem of blocking the dry filter after the scrubber.

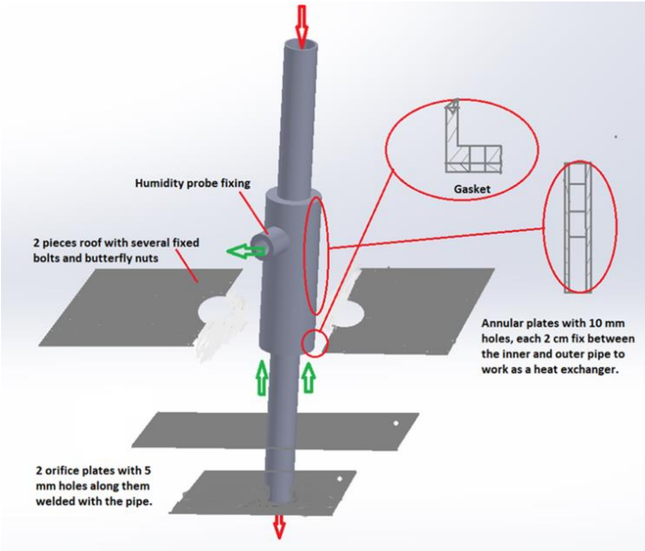

Figure (6-1). New scrubber design.

The new scrubber design solves the existing problem of the high relative humidity of the outlet gas. This solution combined the inlet and the outlet gas pipes together in the annular base (Figures 6-1 and 6-2). This transfers the heat from the inlet gas to the outlet gas through the pipe wall. As a result, the inlet gas temperature would decrease causing less liquid evaporation rate. The heat gained by the outlet gas would reduce the outlet gas relative humidity by heating the outlet gas. The inner annular plates fitted between the inlet and outlet pipes would condense some liquid vapor and prevent some liquid from leaving the scrubber.

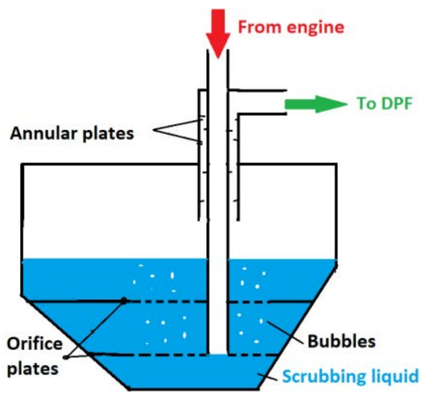

Figure (6-2). The schematic diagram of the new design.

References (Bibliography)

Abdulmouti (**2014**) Bubbly two-phase flow: part II- characteristics and parameters, American J. Fluid Dynamics, 4(4), p. 115-180, doi: 10.5923/j.ajfd.20140404.01.

Abdulwahid, A. A., Situ, R., Brown, R. J. Underground diesel exhaust wet scrubbers: Current status and future prospects. *Energies* **2018**, 11, 1-20. doi:10.3390/en11113006.

Abdulwahid, A. A., Situ, R., Brown, R. J., Heat and mass transfer process in exhaust wet scrubber, 21st Australasian Fluid Mech. Conf. 10th-13th Dec. **2018**, Australia, doi: https://www.conftool.com/21afmc/index.php?page=browseSessions&form_session=59.

Akhtar, A. CFD Simulations for continuous flow of bubbles through gas-liquid columns: Application of VOF Method. *Chem. Product Process Model.* **2007**, *2*, 1–19.

Ali, M. K. A.; CFD Simulation of bubbly flow through a bubble column. *Int. J. Sci. Eng. Res.* **2014**, *5*, 904–910.

Al-Shemmeri, T. T., Oberweis, S. Correlation of the NOx emission and exhaust gas temperature for biodiesel. *Applied Thermal Eng.* **2011**, *31*, 1682-1688. doi: 10.1016/j.applthermaleng.2011.02.010.

Anagbo, P.E. Formation of ellipsoidal bubbles at free-standing nozzle. *Chem. Eng. Sci.* **1991**, *46*, 781–788.

Andras, H.; Christian, J.; Michael, L.; Christia, K.; Aleksander, M.; Michael, H. CFD Simulation of bubble columns using the VOF model: comparison of commercial and open source solvers with an experiment. *Chem. Eng. Trans.* **2009**, *18*, doi:10.3303/CET0918098.

Asar, M., Hormozi, F., Experimental Determination of Bubble Size in Solution of Surfactants of the Bubble Column. J. Adv. Chem. Eng., **2014**, 4, pp. 1-5.

Azzopardi, B.; Zhao, D.; Yan, Y.; Morvan, H.; Mudde, R.F.; Lo, S. *Hydrodynamics of Gas-Liquid Reactors*; Wiley: Hobbken, NJ, USA, **2011**.

Bai, W. Experimental and Numerical Investigation of Bubble Column Reactors. Ph.D. Thesis, Eindhoven University of Technology, Eindhoven, The Netherlands, **2010**.

Bandara, U. C., Yapa, P. D., **2011**, Bubble sizes, breakup, and coalescence in deep water gas/oil plumes, J. Hydraul. Eng., v 137, issue 7, pp. 729-738, doi: 10.1061/.

Bandyopadhyay, A.; Biswas, M.N. Fly-ash scrubbing in a tapered bubble column scrubber. *Process Saf. Environ. Prot.* **2006**, *84*, 54–62, doi:10.1205/psep.05040.

Barbour, W.; Oommen, R.; Shareef, G.S.; Corporation, R.; Vatavuk, W.M. EPA Air Pollution Control Cost Manual (Sixth Edition)-SO_2 and Acid Gas Controls, **2002**. Available online: https://www3.epa.gov/ttn/ecas/docs/cs5-2ch1.pdf (accessed on 22.12.2017).

Besagni, G.; Inzoli, F.; Ziegenhein, T. Two-phase bubble columns: A comprehensive review. *Chem. Eng.* **2016**, *2*, 1–79, doi:10.3390/chemengineering2020013.

Besagni, G., Inzoli, F., The effect of liquid phase properties on bubble column fluid dynamics: Gas holdup, flow regime transition, bubble size distributions and shapes, interfacial areas and foaming phenomena. Chem. Eng. Sci., **2017**, 160, pp. 270-296.

Bhadra, V.; Singh, H.K.; Kahndelwal, G.; Kumar, A. Effect of flue gases with wet scrubber in 4-stroke C.I engine. *Int. J. Sci. Eng. Technol*. **2014**, *2*, 1422–1430.

Burtscher, H. Physical characterization of particulate emissions from diesel engines: A review. *J. Aerosol Sci.* **2005**, *36*, 896–932, doi:10.1016/j.jaerosci.2004.12.001.

Cardenas, M.D.; Armas, O.; Mata, C.; Soto, F. Performance and pollutant emissions from transient operation of a common rail diesel engine fueled with different biodiesel fuels. *Fuel* **2016**, *185*, 743–762, doi:10.1016/j.fuel.2016.08.002.

Chen, Y.M.; Mayinger, F. Measurement of heat transfer at the phase interface of condensing bubbles. *Int. J. Multiph. Flow* **1992**, *18*, 877–890.

Cho, Y.J.; Woo, K.J.; Kang, Y.; Kim, S.D. Dynamic characteristics of heat transfer coefficient in pressurized bubble columns with viscous liquid medium. *Chem. Eng. Process.* **2002**, *41*, 699–706.

Chen, P. Modeling the Fluid Dynamics of Bubble Column Flows. Ph.D. Thesis, Washington University, Washington, DC, USA, 2004.

Clift, R., Grace, J. R., Weber, M. E., Bubbles, drops and particles, *Academic press, A subsidiary of Harcourt Brace Jovanovich, Publishers*. **1978**, 1-380.

D'Addio, L.; Natale, F.D.; Carotenuto, C.; Scoppa, G.; Dessy, V.; Lancia, A. Removal of fine and ultrafine combustion derived particles in a wet electrostatic scrubber, **2013**. Available online: http://www.combustion-institute.it/proceedings/XXXVI-ASICI/papers/36proci2013.VI4.pdf (accessed on 12.07.2017).

Davidson, J. F.; Schüler, B. O. G., Bubble formation at an orifice in a viscous liquid. *Trans. Ins. Chem. Engrs*. **1960**, *38*, p 335–342.

Davidson, J. F., Schüler, B. O. G., **1997**, Bubble formation at an orifice in a viscous liquid, Ins. Chem. Eng., 75, pp. 105-115.

Davies, R. M.; Taylor, G. The mechanics of large bubbles rising through liquids in tubes. *Proc. Roy. Soc*. **1950**, p 375–390, doi:10.1098/rspa.1950.0023.

Deju, L., **2014**, Population balance modelling of gas-liquid bubbly flow: capturing coalescence and breakup processes, PhD thesis, RMIT University, Australia. Pp.1-144.

Deckwer, W.D.; Loulsl, Y.; Zaldl, A.; Ralek, M. Hydrodynamic properties of the Fischer-Tropsch slurry process. *Ind. Eng. Chem. Process Des. Dev.* **1980**, *19*, 699–708.

Delnoij, E.; Lammers, F.A.; Kuipers, J.A.M.; Swaaij, W.P.M. v. Dynamic simulation of dispersed gas-liquid two-phase flow using a discrete bubble model. *Chem. Eng. Sci*. **1997**, *52*, 1429–1458.

DeGuzman, N.M.; Chato, J.C. Evaporative Heat Transfer Characteristics in a Vertical Channel With Obstructions, **1997**. Available online: https://core.ac.uk/download/pdf/4820839.pdf (accessed on 18.09.2018).

Ebrahiem, E.E.; Al-Maghrabi, M.N.; Mobarki, A.R. Removal of organic pollutants from industrial wastewater by applying photo-Fenton oxidation technology. *Arab. J. Chem*. **2017**, *10*, S1674–S1679.

Ekambara, K.; Dhotre, M.T. CFD Simulation of bubble column. *Nuclear Eng. Des.* **2010**, *240(5),* 963–969, doi:10.1016/j.nucengdes.2010.01.016.

Fair, J.R.; Lambright, A.J.; Andersen, J.W. Heat transfer and gas holdup in a sparged contactor. *I EC Process Des. Dev.* **1962**, *1*, 33–36.

Filippa, L., et al., Sauter mean diameter determination for the fine fraction of suspended sediments using a LISST-25X diffractometer. Measurement, **2012**, 45, pp. 364-368.

Funada, T., Joseph, D. D., Maehara, T., Yamashita, S., **2005**, Ellipsoidal model of the rise of a Taylor bubble in a round tube, International Journal of Multiphase Flow, 31 (4), pp. 473-491, doi: 10.1016/j.ijmultiphaseflow.2004.11.010.

Gabriel, D.; Cox, H.H.J.; Deshusses, M.A. Conversion of full-scale wet scrubbers to biotrickling filters for H2S control at publicly owned treatment works. *J. Environ. Eng.* **2004**, *130*, 1110–1117, doi:10.1061/(ASCE)0733-9372(2004)130:10(1110.

Gaffney, J.S.; Marley, N.A. The impacts of combustion emissions on air quality and climate – From coal to biofuels and beyond. *Atmos. Environ.* **2009**, *43*, 23–36, doi:10.1016/j.atmosenv.2008.09.016.

Gandhi, A.B.; Joshi, J.B. Estimation of heat transfer coefficient in bubble column reactors using support vector regression. *Chem. Eng. J.* **2010**, *160*, 302–310, doi:10.1016/j.cej.2010.03.026.

Giakoumis, E.G.; Dimaratos, A.M.; Rakopoulos, C.D.; Rakopoulos, D.C. Combustion instability during starting of turbocharged diesel engine including biofuel effects. *J. Energy Eng*. **2017**, *143*, 1–15, doi:10.1061/(asce)ey.1943-7897.0000402.

Giechaskiel, B.; Suarez-Bertoa, R.; Lahde, T.; Clairotte, M.; Carrier, M.; Bonnel, P.; Maggiore, M. Evaluation of NOx emissions of a retrofitted euro 5 passenger car for the horizon prize "Engine retrofit". *Environ. Res.* **2018**, *166*, 298–309, doi:10.1016/j.envres.2018.06.006.

Giechaskiel, B.; Schwelberger, M.; Delacroix, C.; Marchetti, M.; Feijen, M.; Prieger, K.; Andersson, S.; Karlsson, H. Experimental assessment of solid particle number Portable

Emissions Measurement Systems (PEMS) for heavy-duty vehicles applications. *J. Aerosol Sci.* **2018**, *123*, 161–170, doi:10.1016/j.jaerosci.2018.06.014.

Giechaskiel, B. Solid particle number emission factors of euro VI heavy-duty vehicles on the road and in the laboratory. *Int. J. Environ. Res. Public Health* **2018**, *15*, 1–24, doi:10.3390/ijerph15020304.

Giechaskiel, B.; Clairotte, M.; Valverde-Morales, V.; Bonnel, P.; Kregar, Z.; Franco, V.; Dilara, P. Framework for the assessment of PEMS (Portable Emissions Measurement Systems) uncertainty. *Environ. Res.* **2018**, *166*, 251–260, doi:10.1016/j.envres.2018.06.012.

Groothoff, B., Norris, J., Oldfield, G., Reed, S., Langley, C., Clar, S., Bond, R.; Diesel Particulate Matter & Occupational Health Issues, **2013**. Available online: http://www.gastech.com.au/files/dpm/Diesel-Particulate-Matter-and-Occupational-Health-Issues.pdf (accessed on 26.01.2017).

Guo, R.; Gao, X. Simultaneous removal of SO_2 and NO_2 by wet scrubbing using aqueous limestone slurry. In Proceedings of the 11th International Conference on Electrostatic Precipitation, Hangzhou, China, 20-24th October **2008**; pp. 602–605.

Harris, P.J.; Al-Awadi, H.; Soh, W.K. An investigation into the effects of heat transfer on the motion of a spherical bubble. *ANZIAM J.* **2004**, *45*, 361–371.

Hart, W.F., Heat transfer in bubble-agitated system. A general correlation. *Ind. Eng. Chem., Process Des.* **1976**, *15*, 109–114.

Hasan, B. O., **2017**, Breakage of drops and bubbles in a stirred tank: A review of experimental studies.

Higuera, F.J.; Medina, A. Injection and coalescence of bubbles in a quiescent inviscid liquid. *Eur. J. Mech. - B/Fluids* **2006**, *25*, 164–171, doi:10.1016/j.euromechflu.2005.06.001.

Hikita, H.; Asal, S.; Klkukawa, H.; Zalke, T.; Ohue, M. Heat transfer coefficient in bubble columns. *American Chem. Society* **1981**, *20*, 540–545.

Honkanen, M., Eloranta, H., Saarenrinne, P., **2010**, Digital imaging measurement of dense multiphase flows in industrial processes, Flow Measurement and Instrumentation, 21 (1), pp. 25-32, doi: 10.1016/j.flowmeasinst.2009.11.001.

Hoque, N., Situ, R., Hagan, W., Almedia, J., Lin, W., Brown, R.J., A thermo-fluid study of a diesel engine wet scrubber. *In Proceedings of the 19^th^ Australasian Fluid Mechanics Conference*, Melbourne, Australia, 8–11 December **2014**.

Huang, W. Homogeneous and heterogeneous Fenton and photo-Fenton processes: impact of iron complexing agent ethylenediamine-N,N'-disuccinic acid (EDDS), **2013**. Available online: https://tel.archives-ouvertes.fr/tel-00788822/document (accessed on 18.09.2018).

Incropera, F. P., DeWitt, D. P. Fundamentals of heat and mass transfer. J. Wiley **2002**, New York.

Ishii, M.; Hibiki, T. *Thermo-Fluid Dynamics of Two-Phase Flow*; Springer: New York, USA, **2006**.

Islam, M. T., Ganesan, P. B., Sahu, J. N., Sandaran, S. C. Effect of orifice size and bond number on bubble formation characteristics: A CFD study. *The Canadian J. Chem. Eng*. **2015**, *93 (10),* p 1869-1879, doi: 10.1002/cjce.22282.

Jhawar, A.K.; Prakash, A. Analysis of local heat transfer and hydrodynamics in a bubble column using fast response probes. *Chem. Eng. J.* **2007**, *62*, 7274–7281, doi:10.1016/j.ces.2007.08.026.

Kantarci, N.; Borak, F.; Ulgen, K.O. Bubble column reactors. *Process Biochem.* **2005**, *40*, 2263–2283, doi:10.1016/j.procbio.2004.10.004.

Khan, K.I. Fluid dynamic modelling of bubble column reactor. PhD thesis, Politecnico di Torino, Italia, 2014.

Korath, J. M., Abbas, A., Romagnoli, J. A., **2007**, Separating touching and overlapping objects in particle images – A combined approach, Chem. Eng. Trans., 11, pp. 167-172.

Kowalczuk, P., Drzymala, J., Physical meaning of the Sauter mean diameter of spherical particulate matter. Particulate Sci. Tech., **2015**, 34, pp. 645-647.

Krishna, R.; Swart, J.W.A. D.; Hennephof, D.E.; Ellenberger, J.; Hoefsloot, H.C.J. Influence of increased gas density on hydrodynamics of bubble column reactors. *AIChE J.* **1994**, *40*, 112–121.

Kurella, S.; Balla, M.; Bhukya, P.K. Scrubbing of HCl gas from synthesis gas in a multistage dual-flow sieve plate wet scrubber by alkaline solution. *J. Chem. Eng. Process Technol.* **2015**, *6*, 1–7, doi:10.4172/2157-7048.1000250.

Laakkonen, M., Moilanen, P., Miettinen, T., Saari, K., Honkanen, M., Saarenrinne, P., Aittamaa, J., **2005**, Local Bubble Size Distributions in Agitated Vessel, Chemical Engineering Research and Design, 83 (1), pp.50-58, doi: 10.1205/cherd.04122.

Lapin, A.; Lübbert, A. Numerical simulations of the dynamics of two-phase gas-liquid flows in bubble columns. *Chem. Eng. Sci.* **1994**, *49*, 3661–3674.

Leibson, I.; Holcomb, E.G.; Cacoso, A.G.; Jacmic, J.J. Formation from single orifices. *AIChE J.* **1956**, *2*, p 296–306.

Lee, H.C.; Oh, B.D.; Bae, S.W.; Kim, M.H.; Lee, J.Y.; Song, I.S. Partial nucleate boiling on the microscale heater maintaining constant wall temperature. *J. Nucl. Sci. Technol*. **2003**, *40*, 768–774.

Leong, K.C.; Ho, J.Y.; Wong, K.K. A critical review of pool and flow boiling heat transfer of dielectric fluids on enhanced surfaces. *Appl. Therm. Eng.* **2017**, *112*, 999–1019, doi:10.1016/j.applthermaleng.2016.10.138.

Lehr, F.; Mewes, D. A transport equation for the interfacial area density applied to bubble columns. *Chem. Eng. Sci*. **2001**, *56*, 1159–1166.

Levich, V.G. *Physiochemical Hydrodynamics*; Prentice-Hall: Englewood Cliffs, NJ, USA., 1962.

Lin, T.; Fan, L. Heat transfer and bubble characteristics from a nozzle in high-pressure bubble columns. *Chem. Eng. Sci*. **1999**, *54*, 4853–4859.

Lienhard IV, J.H.; Lienhard V, J.H. *A Heat Transfer Text Book*, 4th Ed.; Phlogiston Press: Cambridge, MA, USA, **2011**.

Loth, E., et al., Effective diameter for group motion of polydisperse particle mixtures. Powder Tech., **2004**, 142, pp. 209-218.

Luo, H., Svendsen, H. F., **1996**, Theoretical model for drop and bubble breakup in turbulent dispersions.

Maab, S., Kraume, M., 2011, Determination of breakage rates using single drop experiments.

Machulek, A.; Quina, F.H.; Gozzi, F.; Silva, V.O.; Friedrich, L.C.; Moraes, J.E.F. Fundamental mechanistic studies of the photo-Fenton reaction for the degradation of organic pollutants, **2012**. Available online: https://www.intechopen.com/books/organic-pollutants-ten-years-after-the-stockholm-convention-environmental-and-analytical-update/fundamental-mechanistic-studies-of-the-photo-fenton-reaction-for-the-degradation-of-organic-pollutan(accessed on 13.09.2018).

Martínez-Bazán, C.; Montañéz, J.L.; Lasheras, J.C. On the breakup of an air bubble injected into a fully developed turbulent flow: I: Breakup frequency. *J. Fluid Mech*. **1999**, *401*, 157.

Masood, R.M.A.; Rauh, C.; Delgado, A. CFD Simulation of bubble column flows: An explicit algebraic Reynolds stress model approach. *Int. J. Multiph. Flow* **2014**, *66*, 11–25, doi:10.1016/j.ijmultiphaseflow.2014.06.008.

Mata, C.; Gómez, A.; Armas, O. The influence of ethanol-diesel blend on pollutant emissions from different bus fleets under acceleration transitions. *Fuel* **2017**, *209*, 322–328, doi:10.1016/j.fuel.2017.08.018.

Meikap, B.C.; Kundu, G.; Biswas, M.N. Modeling of a novel multi-stage bubble column scrubber for flue gas desulfurization. *Chem. Eng. J.* **2002**, *86*, 331–342.

Mikic, B.B.; Rohsenow, M.W. A new correlation of pool-boiling data including the effect of heating surface characteristics. *J. Heat Trans*. **1969**, *9*, 245–250.

Miljevic, B. The Application of a Profluorescent Nitroxide Probe to Detect Reactive Oxygen Spices Derived from Combustion-Generated Particulate Matter. Ph.D. Thesis, Queensland University of Technology, Queensland, Australia, 2010.

Moalem, D.; Sideman, S. Bubble condensation with non-homogeneous distribution of non-condensables. *Int. J. Heat Mass Trans.* **1971**, *14*, 2152–2156.

Moalem, D.; Sideman, S. The effect of motion on bubble collapse. *Int. J. Heat Mass Trans*. **1973**, *16*, 2321–2329.

Monahan, S.M. Computational Fluid Dynamics Analysis of Air-Water Bubble Columns. Ph.D. Thesis, Iowa State University, Ames, IA, USA, 2007.

Munkejord, S.T.; Jakobsen, J.P.; Austegard, A.; Molnvik, M.J. Thermo- and fluid-dynamical modelling of two-phase multi-component carbon dioxide mixtures. In Proceedings of the 9th International Conference on Greenhouse Gas Control Technologies, Washington, DC, USA, **2008**.

Mussatti, D.; Hemmer, P.; EPA Air Pollution Control Cost Manual (Sixth Edition)-Wet Scrubbers for Particulate Matter, **2002**. Available online: https://www3.epa.gov/ttncatc1/dir1/cs6ch2.pdf (accessed on 22.12.2017).

O'Sullivan, C. T. Newton's law of cooling- A critical assessment. *Am. J. Phys.* 1990, *58 (10),* 956-960. doi: 10.1119/1.16309.

Ozisik, M.N.; Kress, T.S. Effects of internal circulation velocity and noncondensable gas on vapor condensation from a rising bubble. *Nuclear Sci.Eng*. **1978**, *66*, 397–405.

Pacek, A., et al. On the Sauter mean diameter and size distributions in turbulent liquid/liquid dispersions in a stirred vessel. Chem. Eng. Sci., **1998**, 53, pp. 2005-2011.

Papagiannakis, R.G.; Hountalas, D.T.; S. R. Krishnan, S.R.; Srinivasan, K.K.; Rakopoulos, C.D.; Rakopoulos, D.C. Numerical evaluation of the effects of compression ratio and diesel fuel Injection timing on the performance and emissions of a fumigated natural gas–diesel dual-fuel engine. *J. Energy Eng*. **2016**, *142*, 1–16, doi:10.1061/(asce)ey.1943-7897.0000326.

Parkinson, L.; Sedev, R.; Fornasiero, D.; Ralston, J. The terminal rise velocity of 10-100 µm diameter bubbles in water. *J. Colloid Interface Sci.* **2008**, *322*, 168–172, doi:10.1016/j.jcis.2008.02.072.

Pratt, S.; Grainger, A.; Jones, L.; Todd, J.; Brennan, R. Diesel Vehicle Research at BHP Collieries, **1998**. Available online: https://ro.uow.edu.au/cgi/viewcontent.cgi?referer=https://www.google.com.tw/&httpsredir=1&article=1274&context=coal (accessed on 23.05.2018).

Qian, D., McLaughlin, J. B., Sankaranarayanan, K., Sundaresan, S., Kontomaris, K., **2006**, Simulation of Bubble Breakup Dynamics in Homogeneous Turbulence, Chem. Eng. Comm., 193 (80), pp. 1038-1063, doi: 10.1080/00986440500354275.

Quinn, J. J.; Maldonado, M.; Gomez, C. O.; Finch, J. A. Experimental study on the shape–velocity relationship of an ellipsoidal bubble in inorganic salt solutions. *Minerals Eng.* **2014,** 55, p 5-10, doi:org/10.1016/j.mineng.2013.09.003.

Rakopoulos, D.C.; Rakopoulos, C.D.; Giakoumis, E.G. Impact of properties of vegetable oil, bio-diesel, ethanol and n-butanol on the combustion and emissions of turbocharged HDDI diesel engine operating under steady and transient conditions. *Fuel* **2015**, *156*, 1–19, doi:10.1016/j.fuel.2015.04.021.

Rakopoulos, D.C.; Rakopoulos, C.D.; Giakoumis, E.G.; Komninos, N.P.; Kosmadakis, G.M.; Papagiannakis, R.G. Comparative evaluation of ethanol, n-butanol and diethyl ether effects as biofuel supplements on combustion characteristics, cyclic variations and emissions balance in light-duty diesel engine. *J. Energy Eng.* **2017**, *143*, 1–8, doi:10.1061/(asce)ey.1943-7897.0000399.

Rao, V.; Dayawansa, D.; Honnery, D.; Sharman, S.; Garnier, G.; Curcio, P. Extending the Life of Disposable Exhaust Filters in Vehicles Operating in Underground Coal Mines; ACARP Report C21017, Monash University, Melbourne, Australia, **2013**.

Rao, V.; Dayawansa, D.; Honnery, D. Reducing Diesel Particulate Matter in Underground Mines by Optimising Design and Operation of Diesel Exhaust Systems, **2015**. Available online: https://www.acarp.com.au/abstracts.aspx?repId=C23013 (accessed on 2018.09.19).

Raymond, F.; Rosant, J.M. A numerical and experimental study of the terminal velocity and shape of bubbles in viscous liquids. *Chem. Eng. Sci*. **2000**, *55*, 943–955.

Rens, G.L.M. A. v.; Wilde, H.P.J. d. Pre- and After-Treatment Techniques for Diesel Engines in Inland Navigation, **2005**. Available online: https://www.ecn.nl/publicaties/PdfFetch.aspx?nr=ECN-RX--05-175 (accessed on 26.01.2017).

Ristovski, Z.D.; Miljevic, B.; Surawski, N.C.; Morawska, L.; Fong, K.M.; Goh, F.; Yang, I.A. Respiratory health effects of diesel particulate matter. *Respirology* **2012**, *17*, 201–212, doi:10.1111/j.1440-1843.2011.02109.x.

Saxena, S.C. Heat transfer from a cylindrical probe immersed in a bubble column. *Chem. Eng. J*. **1989**, *41*, 25–39.

Setten, B.A.A. L. v.; Makkee, M.; Moulijn, J.A. Science and technology of catalytic diesel particulate filters. *Catal. Rev*. **2001**, *43*, 489–564, doi:10.1081/cr-120001810.

Shaikh, A.; Al-Dahhan, M.H. A review on flow regime transition in bubble columns. *Int. J. Chem. React. Eng.* **2007**, *5*, 1–68.

Simmons, J. A., Sprittles, J. E., Shikhmurzaev, Y. D., **2015**, The formation of a bubble from a submerged orifice, European J. Mech. - B/Fluids, pp. 1-29.

Situ, R., Brown, R. J., Wang, H., Surawski, N., Ristovski, Z. D. Exit humidity of wet scrubbers for underground coal mines. *18th Australasian Fluid Mech. Conf.* 3rd-7th Dec. **2012**, Australia.

Shen, L., Song, X., Iguchi, M., Yamamoto, F., **2000**, A method for recognizing particles in overlapped particle images, Pattern Recognition Letters, 21, pp. 21-30.

Shuyi, X. Bubble formation at multiple orifices. *MSc. Thesis* **2003**, National University of Singapore.

Solsvik, J., Skjervold, V. T., Jakobsen, H. A., **2017**. A breakage model for finite Reynolds number flow.

Stainless steel grade datasheets, *Atlas Steels Tech. Dep.* **2013.**

Studley, F., **2010**, Numerical modeling of air-water flows in bubble columns and airlift reactors, MSc. thesis, Faculty of the Virginia Polytechnic Institute and State University, Virginia, USA., pp. 1-57.

Suarez-Bertoa, R.; Kousoulidou, M.; Clairotte, M.; Giechaskiel, B.; Nuottimäki, J.; Sarjovaara, T.; Lonza, L. Impact of HVO blends on modern diesel passenger cars emissions during real world operation. *Fuel* **2019**, *235*, 1427–1435, doi:10.1016/j.fuel.2018.08.031.

Talaia, M.A.R. Terminal velocity of a bubble rise in a liquid column. *World Acad. Sci. Eng. Technol*. **2007**, *28*, 264–268.

Tang, H., et al., Calculation method for particle mean diameter and particle size distribution function under dependent model algorithm. Chinese optics letters, **2007**, 5, pp. 31-33.

Thakre, S.S.; Joshi, J.B. CFD simulation of bubble column reactors: importance of drag force formulation. *Chem. Eng. Sci.* **1999**, *54*, 5055–5060.
Thermal properties of plastic materials, *Professional Plastics* **2019**.

Theofanous, T.G.; Fauske, H.K. The effect of noncondensables on the rate of sodium vapor condensation from a single-rising HCDA bubble. *Nucl. Tech.* **1973**, *19*, 132–139.

Tomiyama, A.; Kataoka, I.; Zun, I.; Sakaguchi, T. Drag coefficients of single bubbles under normal and micro gravity conditions. *JSME Int. J. Ser. B* **1998**, *41*, 472–479.

Tomiyama, A.; Celata, G.P.; Hosokawa, S.; Yoshida, S. Terminal velocity of single bubbles in surface tension force dominant regime. *Int. J. Multiph. Flow* **2002**, *28*, 1497–1519.

Tokumura, M.; Mizukoshi, A.; Noguchi, M.; Wada, Y.; Usami, Y.; Yamaki, T.; Yanagisawa, Y. Removal of acetaldehyde gas using wet scrubber coupled with photo-Fenton reaction. *AIMS Environ. Sci*. **2016**, *3*, 159–167, doi:10.3934/environsci.2016.1.159.

Vinnett, L., et al., Bubble Size Analysis and Boundary Conditions for Automatic Control of Industrial Flotation Cells. IFAC Proceedings, **2009**, 42, pp. 161-166.

Volkwein, J.C.; Mischler, S.E.; Davies, B.; Ellis, C. Field measurement of diesel particulate matter emissions. *Ann. Occup. Hyg.* **2008**, *52*, 99–105, doi:10.1093/annhyg/mem069.

Wang, T.; Wang, J.; Jin, Y. Theoretical prediction of flow regime transition in bubble columns by the population balance model. *Chem. Eng. Sci.* **2005**, *60*, 6199–6209, doi:10.1016/j.ces.2005.04.027.

Wang, H.Y.; Dong, F. A method for bubble volume calculating in vertical two-phase flow. *J. Phys. Conf. Ser.* **2009**, *147*, 1–12, doi:10.1088/1742-6596/147/1/012018.

Walsh, M.A. Overview of Basic Types and Configuration of Wet Scrubber Technologies, **2007**. Available online: http://wpca.info/pdf/presentations/Eskom2007/2)Overview%20of%20Basic%20Types%20&%20Config%20of%20WFGD%20by%20Mike%20Walsh-Marsulex.pdf (accessed on 17.09.2018).

Wallis, G.B. *One-Dimensional Two-Phase Flow*; McGraw-Hill: New York, NY, USA, 1969.

Watano, S., Miyanami, K., **1995**, Image processing for on-line monitoring of granule size distribution and shape in fluidized bed granulation, Powder Tech., 83, pp. 55-60.

Xu, Y. Direct Contact Condensation with and Without Noncondensable Gas in a Water Pool. Ph.D. Thesis, Purdue University, West Lafayette, IN, USA, **2004**.

Yang, G.Q.; Luo, X.; Lau, R.; Fan, L.S. Heat-transfer characteristics in slurry bubble columns at elevated pressures and temperatures. *Ind. Eng. Chem*. **2000**, *39*, 2568–2577.

Youssef, A.A. Fluid Dynamics and Scale-Up of Bubble Columns with Internals. Ph.D. Thesis, Washington University in St. Louis, Washington, DC, USA, **2010**.

Zizka, M., Sulc, R., Ditl, P. Heat transfer between gas and liquid in a bubble column. *Chem. Eng. Trans.* **2017**, *57*, 1261-1266. doi: 10.3303/CET1757211.

Zhang, Y., Sam, A., Finch, J. A. Temperature effect on single bubble profile in water and surfactant solution. *Colloids & surfaces A: physicochemical and Eng. Aspects* **2003**, *223 (1-3),* p 45-54, doi: org/10.1016/S0927-7757(03)00189-4.

Zhang, L.; Yang, C.; Mao, Z. Unsteady motion of a single bubble in highly viscous liquid and empirical correlation of drag coefficient. *Chem. Eng. Sci*. **2008**, *63*, 2099–2106, doi:10.1016/j.ces.2008.01.010.

Zhang, W., Jiang, X., Liu, Y., **2012**, A method for recognizing overlapping elliptical bubbles in bubble image, Pattern Recognition Letters, 33 (12), pp. 1543-1548, doi: 10.1016/j.patrec.2012.03.027.

Zhen, T.; Cheng, Y.; Li, X.; Wang, L. Bubble shape and rising velocity in viscous liquids at high temperature and pressure. *Experim. Thermal & Fluid Sci.* **2019**, *102*, p 528-538, doi.org/10.1016/j.expthermflusci.2018.12.018.

Ziegenhein, T., Fluid dynamics of bubbly flows. Technischen Universität, Berlin, Germany, **2016**.

Appendices

Appendix A

Table (A) Steady-state Heating Experiments Operating Conditions.

Test No.	Test symbol	Inlet gas flow rate (SLPM)	Inlet gas temperature ($T_{in\ 1}$) (ºC)	Liquid volume ratio (%)	Orifice size (mm)	Liquid temperature (T_l) (ºC)	Outlet gas temperature (T_o) (ºC)	RH_o (%)
1	◇	100	150	20	N/A	45.4	41.2	92.5
		100	250	20	N/A	45.5	41.3	96.5
		100	350	20	N/A	44.5	40.5	96.5
		100	450	20	N/A	45.7	41.8	95
		100	550	20	N/A	46.4	41.9	96.5
		100	650	20	N/A	47.2	43.3	96.5
2	□	160	150	20	N/A	43.9	41	82

		160	250	20	N/A	44.6	42.2	96.5
		160	350	20	N/A	45.1	42.7	96.5
		160	450	20	N/A	46.1	43.6	96.5
		160	550	20	N/A	48.4	44.8	96.5
		160	650	20	N/A	49.7	46.4	96.5
3	○	210	150	19	N/A	54	51.9	96.5
		210	250	19	N/A	55.3	52.4	96.5
		210	350	19	N/A	55.8	51.5	96.5
		210	450	19	N/A	56	53.4	96.5
		210	550	19	N/A	56.5	52.6	96.5
		210	650	19	N/A	57.1	53.6	96.5
4	△	260	150	16	N/A	45	43.3	97

		260	250	16	N/A	46.8	45.2	97
		260	350	16	N/A	52	49.2	97
		260	450	16	N/A	55.4	55.1	97
		260	550	16	N/A	57.5	57.5	97
5	□	100	150	48	N/A	40.6	36.1	97
		100	250	48	N/A	42.5	36.9	97
		100	350	48	N/A	44.5	39.4	97
		100	450	48	N/A	46	40.8	97
		100	550	48	N/A	48.7	43.5	97
		100	650	48	N/A	50.1	46	97
6	◇	160	150	42	N/A	42.8	38.1	96
		160	250	42	N/A	43.8	39	96

		160	350	42	N/A	44.8	39.8	96
		160	450	42	N/A	45.8	40.8	96
		160	550	42	N/A	46.9	42.8	96
		160	650	42	N/A	50.9	45.9	95.5
7	○	210	150	46	N/A	41.6	38.8	96
		210	250	46	N/A	42.1	39.7	96
		210	350	46	N/A	43.3	40.8	96
		210	450	46	N/A	44.3	41.7	96
		210	550	46	N/A	46.4	43	96
		210	650	46	N/A	49.9	45.8	96
8	△	260	150	45	N/A	51.7	48.5	96
		260	250	45	N/A	52.5	49.3	96

		260	350	45	N/A	53.5	49.8	96
		260	450	45	N/A	54.5	50.9	96
		260	550	45	N/A	55.1	52.2	96
9	□	100	150	38	5	32.6	33.4	96
		100	250	38	5	32.6	31.7	96
		100	350	38	5	33	31.8	96
		100	450	38	5	33.4	32.3	96
		100	550	38	5	35.9	33.1	96
		100	650	38	5	37.6	33.8	96
10	◇	160	150	37	5	36.9	38.5	97.5
		160	250	37	5	42.4	41.6	97
		160	350	37	5	45.6	44.9	96

		160	450	37	5	47.9	47.2	95
		160	550	37	5	48	47.9	96
		160	650	37	5	48.5	47.9	96
11	○	210	150	36	5	32.4	31.8	98
		210	250	36	5	33.9	33.6	97
		210	350	36	5	42.4	41.9	96
		210	450	36	5	46.8	46.3	96
		210	550	36	5	50.2	49.7	96
		210	650	36	5	57.3	56.8	96
12	△	260	150	36	5	32.4	31.8	97
		260	250	36	5	33.9	33.6	98
		260	350	36	5	40.2	37.6	98

		260	450	36	5	52.8	47.3	96
		260	550	36	5	56.2	52.9	96
13	□	100	150	38	7.5	43.1	41.3	85
		100	250	38	7.5	44.8	43	96
		100	350	38	7.5	46.3	44.5	96
		100	450	38	7.5	47.7	46.1	96
		100	550	38	7.5	49	47.9	96
		100	650	38	7.5	49.7	49.1	96
14	◇	160	150	38	7.5	41.8	40.7	96
		160	250	38	7.5	41.8	40.7	93
		160	350	38	7.5	42	41	96
		160	450	38	7.5	42.8	41.3	96

		160	550	38	7.5	43.2	42.2	96
		160	650	38	7.5	44.8	43.9	96
15	○	210	150	38	7.5	44.5	44.13707763	96
		210	250	38	7.5	47.9	47.3	96
		210	350	38	7.5	50.2	49.6	96
		210	450	38	7.5	52.6	51.9	96
		210	550	38	7.5	52.7	52.4	96
		210	650	38	7.5	53.1	52.5	96
16	△	260	150	38	7.5	41.7	41.46645669	96
		260	250	38	7.5	47.7	47.3	96
		260	350	38	7.5	52.9	52.6	96
		260	450	38	7.5	57.5	57.4	96

		260	550	38	7.5	58.2	58	96
17	□	100	150	42	10	44.5	41.9	79
		100	250	42	10	45.7	43.2	92
		100	350	42	10	46.4	44.1	96
		100	450	42	10	47.3	45	96
		100	550	42	10	48.4	46.2	96
		100	650	42	10	49.2	46.3	96
18	◇	160	150	42	10	42.2	41.19458167	74
		160	250	42	10	42.3	41.3336255	96
		160	350	42	10	42.4	41.4	94
		160	450	42	10	42.8	41.8	96
		160	550	42	10	43.3	42.2	96

		160	650	42	10	44.4	43.3	96
19	○	210	150	42	10	47.6	46.8	96
		210	250	42	10	49.5	49	96
		210	350	42	10	50.3	49.6	96
		210	450	42	10	50.4	49.7	96
		210	550	42	10	50.8	50	96
		210	650	42	10	50.9	49.7	96
20	△	260	150	42	10	45	44.6	96
		260	250	42	10	45.4	44.7	96
		260	350	42	10	45.9	45.4	96
		260	450	42	10	50.3	49.8	96
		260	550	42	10	54.61	53.6	96

Appendix B – The results of Thermodynamic Analysis

Table (B-1). The constant *C* of the heat loss estimation Equation (4-22) for steady-state heating tests.

Test conditions	C-value
Re 1,200, LVR 20% and β N/A	0.35
Re 1,800, LVR 20% and β N/A	0.53
Re 2,400, LVR 19% and β N/A	0.14
Re 3,300, LVR 16% and β N/A	1.59
Re 1,200, LVR 48% and β N/A	0.05
Re 1,800, LVR 42% and β N/A	0.37
Re 2,400, LVR 46% and β N/A	0.52
Re 3,300, LVR 45% and β N/A	1.39
Re 1,800, LVR 36% and β 0.1	0.41
Re 2,400, LVR 36% and β 0.1	0.11
Re 3,300, LVR 36% and β 0.1	0.48
Re 1,200, LVR 38% and β 0.15	0.24
Re 1,800, LVR 38% and β 0.15	0.32
Re 2,400, LVR 38% and β 0.15	0.98
Re 3,300, LVR 38% and β 0.15	1.65
Re 1,200, LVR 42% and β 0.2	0.24
Re 1,800, LVR 42% and β 0.2	0.35
Re 2,400, LVR 42% and β 0.2	0.97
Re 3,300, LVR 42% and β 0.2	1.6

Table (B-2). The outlet/inlet energies dependant on both Re and θ of the inlet gas and independent on LVR or β.

Test conditions	θ					
	1.4	**1.7**	**2**	**2.4**	**2.7**	**3**
Re 1,200, LVR 20% and β N/A	0.94	0.74	0.62	0.55	0.54	0.46
Re 1,800, LVR 20% and β N/A	1.04	1	0.94	0.8	0.74	0.69

Re 2,400, LVR 19% and β N/A	1.16	1.06	1.02	1.01	0.91	0.82
Re 3,300, LVR 16% and β N/A	1.15	1.03	0.96	1.08	0.94	
Re 1,200, LVR 48% and β N/A	1.16	1	0.85	0.8	0.73	0.86
Re 1,800, LVR 42% and β N/A	1.19	1.07	1	0.87	0.77	0.7
Re 2,400, LVR 46% and β N/A	1.09	1.03	0.91	0.82	0.75	0.7
Re 3,300, LVR 45% and β N/A	1.11	1.07	1.1	0.96	0.85	
Re 1,200, LVR 36% and β 0.1	1.1	0.91	0.8	0.66	0.64	0.53
Re 1,800, LVR 36% and β 0.1	1.24	1.1	0.99	0.9	0.78	0.7
Re 2,400, LVR 36% and β 0.1	1.1	0.9	0.9	0.87	0.81	0.83
Re 3,300, LVR 36% and β 0.1	0.99	0.98	0.91	0.87	0.83	
Re 1,200, LVR 38% and β 0.15	1.07	1.05	0.99	0.87	0.79	0.72
Re 1,800, LVR 38% and β 0.15	1.07	1	0.93	0.81	0.72	0.66
Re 2,400, LVR 38% and β 0.15	1.08	1.02	1.09	0.98	0.87	0.79
Re 3,300, LVR 38% and β 0.15	1.11	1.06	1	1	0.96	
Re 1,200, LVR 42% and β 0.2	1	0.91	0.78	0.68	0.64	0.59
Re 1,800, LVR 42% and β 0.2	1	0.99	0.98	0.9	0.8	0.73
Re 2,400, LVR 42% and β 0.2	1	0.95	0.94	0.88	0.82	0.83
Re 3,300, LVR 42% and β 0.2	0.98	0.99	1	0.87	0.85	

Table (B-3). All results of the liquid mass evaporation ($\dot{m_{ev}} \times 10^4$) (kg/sec).

Test conditions	**θ**					
	1.4	**1.7**	**2**	**2.4**	**2.7**	**3**
Re 1,200, LVR 20% and β N/A	0.86	0.93	0.94	0.99	1.32	1.16
Re 1,800, LVR 20% and β N/A	3.72	3.88	3.88	4	4.07	4.37
Re 2,400, LVR 19% and β N/A	3.6	4.56	6.87	6.94	6.95	7.9
Re 3,300, LVR 16% and β N/A	6.32	6.49	6.88	9.3	10	
Re 1,200, LVR 48% and β N/A	2	2.1	2.37	2.5	2.88	2.74
Re 1,800, LVR 42% and β N/A	3.2	3.54	3.46	3.95	4.1	4.2
Re 2,400, LVR 46% and β N/A	4.47	4.59	4.84	4.94	5.2	5.45
Re 3,300, LVR 45% and β N/A	8	8.1	8.25	8.3	8.7	
Re 1,200, LVR 36% and β 0.1	1.6	1.63	1.84	1.66	2	1.7
Re 1,800, LVR 36% and β 0.1	3.6	3.8	4.25	4.63	4.58	4.66
Re 2,400, LVR 36% and β 0.1	3.26	3.53	5	5.83	6.55	8
Re 3,300, LVR 36% and β 0.1	2.9	4.98	6.1	7.3	8.46	
Re 1,200, LVR 38% and β 0.15	1.8	2.7	2.8	2.95	3.15	3.18
Re 1,800, LVR 38% and β 0.15	3.4	3.5	3.66	3.69	3.85	4.1
Re 2,400, LVR 38% and β 0.15	5.5	6.1	6.47	6.88	7.1	7.2
Re 3,300, LVR 38% and β 0.15	6.36	7.77	9	10.4	10.5	
Re 1,200, LVR 42% and β 0.2	2.4	2.7	2.8	2.83	2.94	2.97

Re 1,800, LVR 42% and β 0.2	3	3.74	3.61	3.81	3.87	3.98
Re 2,400, LVR 42% and β 0.2	6	6.4	6.5	6.6	6.6	6.7
Re 3,300, LVR 42% and β 0.2	6.7	7	7.26	8.2	9	